Investigation of semiconductor nanostructures using optical two-dimensional Fourier-transform spectroscopy

Dissertation
zur
Erlangung des Doktorgrades
der Naturwissenschaften
(Dr. rer. nat.)

dem

Fachbereich Physik
der Philipps-Universität Marburg
vorgelegt von

Irina Kuznetsova

aus

st. Staroizobilnaja
(Russland)

Marburg/Lahn, 2007

Vom Fachbereich Physik der Philipps-Universität als Dissertation

angenommen am 10.10.07

Erstgutachter: Prof. Dr. P. Thomas

Zweitgutachter: Prof. Dr. W. Rühle

Tag der mündlichen Prüfung: 24.10.07

To Valentina and Michael

Contents

Abbreviation

h : heavy hole;

l : light hole;

hh : heavy-hole biexciton;

ll : light-hole biexciton;

lh : mixed heavy-light hole biexciton;

FWM : four-wave-mixing;

FWHM : full-width-at-half-maximum;

2D-FT : two-dimensional Fourier-transformed;

2D-FTS : two-dimensional Fourier-transform spectroscopy;

QW : quantum well;

TR : time-resolved;

TI : time-integrated;

CES : coherent excitation spectroscopy;

NMR : nuclear magnetic resonance.

Chapter 1

Introduction

The aim of this work is the exploration of the recently developed two-dimensional Fourier-transform spectroscopy (2D-FTS) method and its application in the field of semiconductor physics. This multi-dimensional spectroscopy method originates from nuclear magnetic resonance (NMR) [1]. By virtue of its successful application in the field of structural biology, NMR analogs have been further developed in chemistry and later in optics [2]. Admittedly, the interpretations of two-dimensional spectra in the regimes of radio, infrared and optical frequencies are different due to different underlying processes and specialities of those methods. It is, however, clear that those methods yield physical, biological and chemical insights into the structure and/or the dynamics of a variety of complex systems. Recently such two-dimensional spectroscopy method has been developed for the application to semiconductor nanostructures [3].

In semiconductor nanostructures the investigation of electronic states and transitions between them is the central issue. While linear optical measurements provide typically quite unspecific information on, e.g., the total line width, nonlinear experiments have been applied successfully to obtain much more detailed information about the nature of excited states, the coupling among them, and many-body effects [4, 5].

If more than just a single optical resonance is excited, the nonlinear transients in the time domain show quantum beats or polarization interferences [4, 6]. This may complicate the identification of the inhomogeneous contribution to the line width of the individual resonances, in particular, in situations where the nature of the coupling among the relevant electronic states is unknown. The specific feature of 2D-FTS is that it contains the possibility to treat the coupled resonances separately, including the investigation of homogeneous and inhomogeneous broadening (Chapter 11.2, 11.3). We will show that optical 2D-FTS is the appropriate method for the exploration of couplings, including many-body induced coupling between electron-hole pairs (excitons), exciton-exciton (biexciton), and exciton-continuum (Chapter 7). Since 2D-FTS is a variant of the Four-Wave-Mixing (FWM) approach the theoretical modeling requires to treat the many-body interaction up to third order in the electrical field ($\chi^{(3)}$-limit) by applying the Semiconductor Bloch Equations including the correlations. Thus we confine ourselves to the regime of weak excitation.

The first theoretical description of optical 2D-FTS has been based on modified Optical Bloch Equations, where excitation-induced dephasing and the excitation-induced shift have been included [7]. Our simulations are based on an extended one-dimensional tight-binding model (Chapter 3.1) and apply the Semiconductor Bloch Equations including correlations within the $\chi^{(3)}$-limit (Chapter 3.1). The first comparison between experiment and theory for different polarization scenarios of the excitation field is based on this one-dimensional tight-binding model [8]. It is surprising that such a simple model, which in principle allows only a qualitative description, was able to yield almost quantitative agreement between experiment and theory.

The same approach has also been used by the Mukamel-group quite recently, based on our model and our set of equations. Some 2D-FT spectra have been calculated and the relation to Feynman diagrams has been illustrated [9].

It has to be mentioned that this is the first theoretical work which in a consistent theoretical frame treats the signatures of 2D-FTS and their dependencies on various material and experimental parameters in great detail (Chapter 8 to 10). It thus illustrates the versatility and power of this method, which is partly proven by the successful theory-experiment agreement. In addition to this comparison, parameter studies suggest further experiments applied to a variety of nanostructured semiconductor material systems in order to clarify their behavior under light-matter excitation.

To achieve a detailed description of 2D-FTS, we initially treat non-interacting particles (Chapter 4) as a tutorial illustration. For the same purpose we apply this method to artificial model-nanostructures in order to investigate the dependencies of 2D-FTS on different material (Chapter 4, 10.2) and model parameters (Chapter 10). In this sense this work can be considered to be a key study for this method if applied to semiconductor nanostructures.

Since this method is based on the well-known Four-Wave-Mixing (FWM) experiment, it is important to illustrate the differences and similarities with respect to other methods based on FWM. An example of such a method is the Coherent-Excitation-Spectroscopy (CES) method [10]. Similar to 2D-FTS, this method images the coupled excitonic resonances and the couplings within the system in a two-dimensional plot. It is interesting to compare these two methods (Chapter 12). Furthermore, it might be questioned whether 2D-FTS has advantages over the time-resolved and time-integrated FWM-experiments. It is well known that these traces yield information about homogeneous and inhomogeneous broadenings [4] and couplings as well. We focus on this point in Chapter 11 and show the advantage of 2D-FTS over the mentioned methods.

It should be mentioned that both experimental and theoretical work on 2D-FTS in the optical regime is still quite scarce. We believe that this thesis might serve as a starting point of the interpretation of forthcoming experimental work applying 2D-FTS to semiconductor nanostructures in the optical regime.

Part I

Preliminaries

Chapter 2

Experiment and imaging of 2D-FT spectra

Optical two-dimensional Fourier transform spectroscopy (2D-FTS) originates from nuclear magnetic resonance [1] and has later been applied to the infrared regime [11]. In this work we study the application of this method to semiconductor nanostructures theoretically and compare our results with experiment. The main idea of 2D-FTS is to disentangle the experimentally collected information about the excited system and about the couplings between its various resonances.

2D-FTS is based on the Four-Wave-Mixing (FWM) experiment, where the excitation of the sample is performed by a sequence of three pulses a, b, c and the signal is measured in direction $-k_a + k_b + k_c$. Such kind of nonlinear experiment provides, e.g., the well known photon echo [12]. Some textbook explanations of the photon echo are based on time-reversal. However, a more thorough interpretation of the photon echo is based in the concept of phase conjugation of the polarization due to the first pulse in FWM experiments [13].

It is instructive to describe the photon echo experiment as an example of the FWM technique. The first pulse a excites the sample at time $t = -\tau$ with $\tau \geq 0$ (Fig. 2.1, left). Hence the linear-response polarization is generated and in real systems it is damped due to dephasing processes. They include radiation damping, electron-electron and electron-phonon scattering. These processes are characterized

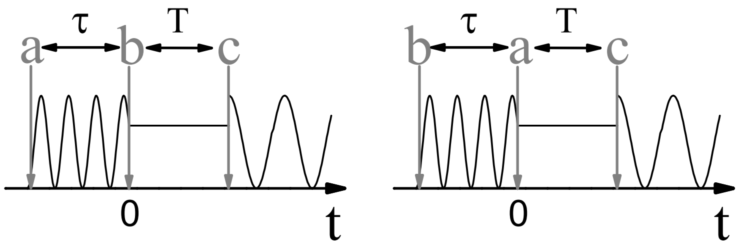

Figure 2.1: Scheme of the 2D-FTS experiment for rephasing (left) and non-rephasing mode (right).

by a dephasing time T_2, if the decay of the polarization is exponential. This yields the so-called homogeneously broadened Lorentzian line. The phase conjugation of the response of the system occurs during the application of the second pulse at time $t = 0$, thus τ is the time separation between the first two pulses. By applying the third pulse at time $t = T$ with $T \geq 0$, we obtain the third-order polarization. This polarization yields the rephasing process, thus the photon echo appears at $t = T + \tau$. Figure 2.1 (left) illustrates such a photon echo experiment, which we will call the rephasing mode of 2D-FTS in the following.

The photon echo is based on disorder (called inhomogeneous line) and on phase conjugation. First of all, in order to measure the photon echo, the analyzed system has to be represented by an ensemble of transitions with slightly different frequencies, which can be described as disorder. The second requirement for a photon echo experiment or the rephasing mode of 2D-FTS is that the polarization due to the first pulse has to be conjugated. The excitation pulses are then given by (leaving the spatial phase factors aside)

$$\begin{aligned} E_a(t) &= \frac{1}{\sqrt{\pi\delta^2}}\eta_0 e^{-i\omega_L(t+\tau)} e^{i\vec{k_a}\cdot\vec{r}} e^{-(t+\tau)^2/\delta^2}, \\ E_b(t) &= \frac{1}{\sqrt{\pi\delta^2}}\eta_0 e^{-i\omega_L t} e^{i\vec{k_b}\cdot\vec{r}} e^{-t^2/\delta^2}, \\ E_c(t) &= \frac{1}{\sqrt{\pi\delta^2}}\eta_0 e^{-i\omega_L(t-T)} e^{i\vec{k_c}\cdot\vec{r}} e^{-(t-T)^2/\delta^2}, \end{aligned} \tag{2.1}$$

where $\tau \geq 0, T \geq 0$ are delay times between the two first and the two last pulses, respectively, and δ is the width of the Gaussian pulse. The factor η_0 quantifies the amplitude of the excitation field, ω_L is the central frequency of the excitation pulses and $\vec{k_n}$ is the wave vector, which denotes the direction of the excitation pulses: $n = a, b, c$. The values of the delay times are restricted by the dephasing time for τ and by the density dynamics for T. If all these above mentioned criteria for the system and for the excitation condition are satisfied, we can perform the photon echo experiment.

Now, we consider the case were the first two pulses are interchanged (Fig. 2.1, right). In this situation the rephasing processes are not active, because now the second pulse a is phase conjugated[1]. This is then called the non-rephasing mode of 2D-FTS. Here we have the following excitation pulses:

$$\begin{aligned}
E_b(t) &= \frac{1}{\sqrt{\pi\delta^2}}\eta_0 e^{-i\omega_L(t-\tau)} e^{i\vec{k_b}\cdot\vec{r}} e^{-(t-\tau)^2/\delta^2}, \\
E_a(t) &= \frac{1}{\sqrt{\pi\delta^2}}\eta_0 e^{-i\omega_L t} e^{i\vec{k_a}\cdot\vec{r}} e^{-t^2/\delta^2}, \\
E_c(t) &= \frac{1}{\sqrt{\pi\delta^2}}\eta_0 e^{-i\omega_L(t-T)} e^{i\vec{k_c}\cdot\vec{r}} e^{-(t-T)^2/\delta^2}, \qquad (2.2)
\end{aligned}$$

where now $\tau \leq 0$ and $T \geq 0$.

We now describe the method of how the two-dimensional 2D-FTS spectra are obtained. In the theoretical description we obtain in the $\chi^{(3)}$-limit the third-order polarization, which depends on both real time t and time delay τ. The last delay time T is a parameter. We apply the Fourier transformation with respect to real time t and the time delay τ. The first Fourier transformation (here it is given for the rephasing mode, where contributions to the integral exist only for $\tau \geq 0$):

$$\begin{aligned}
P(\omega_t, \tau, T) &= \int_{-\infty}^{\infty} P(t, \tau, T) e^{i\omega_t(t-T)} dt, \\
P(\omega_t, -\omega_\tau, T) &= \int_{-\infty}^{\infty} P(\omega_t, \tau, T) e^{-i\omega_\tau \tau} d\tau \qquad (2.3)
\end{aligned}$$

(where $\omega_\tau > 0$) and for the non-rephasing mode the second Fourier transformation

---

[1] FWM-signal direction $-k_a + k_b + k_c$ remains valid.

is:

$$P(\omega_t, \omega_\tau, T) = \int_{-\infty}^{\infty} P(\omega_t, \tau, T) e^{-i\omega_\tau \tau} d\tau, \tag{2.4}$$

where now there are contributions to the integral only for $\tau \leq 0$. Here we also define $\omega_\tau > 0$.

The resulting two-dimensional spectrum $P(\omega_t, \pm\omega_\tau, T)$ contains information about all excited resonances present in the system. It also displays separately all the information about couplings within the system. In the following chapters we will present two-dimensional spectra, where the x-axis displays the emission energy (corresponding to the signal frequency ω_t) and the y-axis displays the absorption energy (corresponding to the frequency ω_τ related to the delay time between first and second pulses).

The nonlinear polarization is the source of electromagnetic radiation from the system that is measured as the optical signal. Its electric field is given by $E(\omega_t, \pm\omega_\tau, T) \propto iP(\omega_t, \pm\omega_\tau, T)$. In this work we present the 2D-FTS amplitude $|E(\omega_t, \pm\omega_\tau, T)|$, the real part $\Re[E(\omega_t, \pm\omega_\tau, T)]$ and the imaginary part spectra $\Im[E(\omega_t, \pm\omega_\tau, T)]$ with respect to the electrical field (as it is performed in the experiment). It is to be noted, that the rephasing 2D-FTS is traditionally[2] displayed on the negative $-\omega_\tau$ axis, as is obvious from the above equations defining the Fourier transforms.

A proper 2D-FTS experiment and its successful interpretation requires a number of important details:

i) In order to see the freely evolving system response extremely short excitation pulses are needed[3]. Otherwise the response is tightly coupled to the excitation field.

ii) In our numerical calculations we replace the Fourier integrals in Eq. (2.3), (2.4) by sums. Thus an insufficient resolution in the τ- and t-domain results in additional signatures in the two dimensional spectra. The resolution in the time domain is also

---

[2] It traces back to nuclear magnetic resonance.

[3] They must be much narrower than the dephasing time, usually in fs-range.

important because it has a bearing on the frequency window due to discrete Fourier transformation. That means in the numerical simulation a periodicity for large $\Delta\tau$ occurs in the spectrum, because the integral is substituted by the following sum:

$$\int_{-\infty}^{\infty} f(\tau) e^{-i\omega\tau} d\tau \Longrightarrow \sum_{n=0}^{N} f(\tau_n) e^{-i(\omega+\omega_m)\tau_n} \Delta\tau, \tag{2.5}$$

and

$$\begin{aligned} \tau_n &= \Delta\tau * n \\ \omega_m &= 2\pi * \frac{m}{\Delta\tau}, \end{aligned} \tag{2.6}$$

where $n = 0, ...N$ and m is any integer. Thus it is important to take into account the restriction for fine resolution in the time domain with the corresponding frequency window.

iii) We have to obey the Nyquist-Shannon sampling theorem, i.e. the sampling frequency $1/\Delta\tau$ $(1/\Delta t)$ has to be at least twice the maximum frequency of the signal.

iv) Finally, for performing the Fourier transformation the oscillating function has to be truncated somewhere. In order to avoid termination errors we need to take the whole range of time delay τ, where the signal $P(\omega_t, \tau, T)$ has significant values.

Chapter 3

Semiconductor model

3.1 One-dimensional tight-binding model

In this chapter we present the one-dimensional tight-binding model, shown in Fig. 3.1. This model provides the band structure and thus forms the basis of the evaluation of the polarization and higher-order correlations in the medium. In Part II it will be shown how we apply this model for the treatment of interacting particles. Here we start by discussing the single-particle properties, i.e., we neglect the many-body interaction. As a first step we assume that the particles are spatially localized at certain sites. The energetic levels of the electrons ϵ_i^e and (heavy h and light l) holes $\epsilon_i^{h,l}$ are given on a one dimensional chain of sites. Other than in a simple atomic level model, our energetic levels couple to the nearest neighbor sites with a strength given by J. The energy E_0 determines, together with the band widths due to this coupling, the energy gap E_g at the Γ-point for the given material system. In order to model semiconductor nanostructures such as quantum wells we here introduce light-hole levels which are higher[1] in energy than that of the heavy holes. The corresponding offset is given by the design of the particular quantum well.

By means of this model we can prepare a matrix, which includes N electron states, N heavy- and N light-hole states. Applying periodic boundary conditions

---

[1] Here, this means the absolute value of the energy.

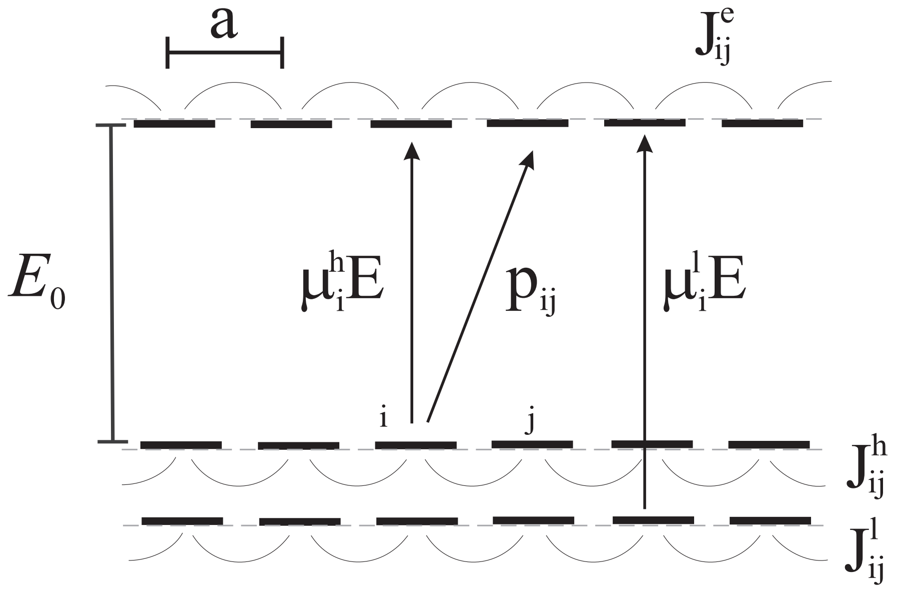

Figure 3.1: One-dimensional tight-binding model for the semiconductor. Upper levels represent distribution of the energetic levels of the electrons in space, middle and lower energetic levels of heavy and light holes, respectively. Here a is the spatial separation between neighbor sites. J^e_{ij} describes coupling between localized electron neighbor sites i and j, $J^{h(l)}_{ij}$ that for heavy and light holes, respectively. Inter-band coherence between sites i and j is given by p_{ij}, with E_0 the band gap energy can be adjusted. $\mu^{h(l)}_i$E depicts the strength of the optical heavy- (light-) hole transition to electron states, induced by electric field E.

we diagonalize this hermitian $3N \times 3N$ matrix

$$\begin{pmatrix}
\epsilon^e_1 & 0 & 0 & J^e & 0 & 0 & \ldots & J^e & 0 & 0 \\
0 & \epsilon^h_1 & 0 & 0 & J^h & 0 & \ldots & 0 & J^h & 0 \\
0 & 0 & \epsilon^l_1 & 0 & 0 & J^l & \ldots & 0 & 0 & J^l \\
\vdots & & & & & & & & & \vdots \\
J^e & 0 & 0 & 0 & 0 & 0 & \ldots & \epsilon^e_N & 0 & 0 \\
0 & J^h & 0 & 0 & 0 & 0 & \ldots & 0 & \epsilon^h_N & 0 \\
0 & 0 & J^l & 0 & 0 & 0 & \ldots & 0 & 0 & \epsilon^l_N
\end{pmatrix}$$

numerically in order to find the eigenvalues and eigenvectors of the ring, which has the radius $Na/2\pi$. N is the number of sites and a is the site separation (lattice constant of our model). The eigenvectors satisfy the Bloch theorem and have the following form:

$$\psi_{\alpha}^{e(h,l)}(k_n, R_j) \;=\; \frac{1}{\sqrt{N}} e^{ik_nR_j} u_{\alpha}(k_n, R_j), \tag{3.1}$$

where u_α is a lattice-periodic Bloch function, i.e., $u_\alpha(k_n, R_j) = u_\alpha(k_n)$, n and $j = 1, ...N$, $R_j = ja$ is the position of site j, and α numbers the eigenvalues. The "vector" k_n is confined to the first Brillouin zone, viz:

$$-\pi/a < k_n \leq \pi/a, \tag{3.2}$$

and has discrete values with $k_n - k_{n-1} = 2\pi/N$.

For this simple situation one can of course also find the eigenvalues and eigenstates analytically. The result for the eigenvalues is [4]

$$E^{e(h,l)}(k) \;=\; const. + 2J^{e(h,l)} cos(ka), \tag{3.3}$$

where J^e is chosen negative, $J^{h(l)}$ are positive in order to have a direct gap at $k = 0$.

The eigenstates are then

$$\psi_{\alpha}^{e(h,l)}(k_n, R_j) \;=\; \frac{1}{\sqrt{N}} e^{ik_nR_j} \tag{3.4}$$

where Eq. (3.3) defines the relation between the eigenvalue and the k-value.

In more complicated cases, which we will encounter later, we can only apply numerical diagonalization and obtain a list of eigenvalues ordered in some way (e.g., according to their magnitude), and a list of eigenvectors $\phi_\alpha(R_j)$, which is ordered in the same way. Knowing that the eigenvectors can be classified by k-values according to Eq. (3.1), we have to find the k-values for a given eigenvalue E_α which then defines the band structure with its dispersion, effective masses etc.

The complication in searching the k-values characterizing the eigenvectors arises due to degeneracy (at least of order 2, namely for k and $-k$ we have $E(k) = E(-k)$) of the eigenstates[2]. In particular, the numerical routine may give us for a given

---

[2] Within this work we do not consider magnetic field effects.

degenerate eigenvalue E_α a linear combination $\phi_\alpha(R_j)$ of eigenvectors $\psi_\alpha^{e,h,l}(k_n^{e,h,l}, R_j)$ having specific but different $k_n^{e,h,l}$ each, and we have to find all these k_n-values. This linear combination can be written, with coefficients $\beta_{e,h,l}$, as

$$\phi_\alpha(R_j) = \beta_e \psi_\alpha^e(k_n^e, R_j) + \beta_h \psi_\alpha^h(k_n^h, R_j) + \beta_l \psi_\alpha^l(k_n^l, R_j). \tag{3.5}$$

To sort out these k-values we take advantage of the periodicity of the complex exponential function $e^{i\kappa_m}$. This function is defined for $[-\pi : \pi]$ and has the same graduation κ_m as $k_n a$. We build sums of the product of eigenvectors[3] and the complex exponential function $e^{i\kappa_m j}$:

$$\sum_j^N [\beta_e \psi_\alpha^e(k_n^e, R_j) + \beta_h \psi_\alpha^h(k_n^h, R_j) + \beta_l \psi_\alpha^l(k_n^l, R_j)] e^{i\kappa_m j} \left\{ \begin{array}{lcl} \neq 0 & : & k_n^{e,h,l} a = \kappa_m \\ = 0 & : & k_n^{e,h,l} a \neq \kappa_m \end{array} \right. \tag{3.6}$$

Here we use that the Bloch function $u_\alpha(k_n)$ is periodic, i.e., independent of position of the sites. Along this way we find out allowed energy states of the electrons and holes and their associated wave vectors. In general cases this dispersion is no more cosine-like.

The effective masses of the electrons and holes result from expanding the cosine functions at k=0 in second order. This leads to (note that $J^e < 0$ and $J^{h(l)} > 0$):

$$m_e = -\frac{\hbar^2}{2J^e a^2} \tag{3.7}$$

$$m_{h(l)} = \frac{\hbar^2}{2J^{h(l)} a^2} \tag{3.8}$$

It is to be noted that all the parameters of this model, including the distance between the sites a are not material parameters. Relevant physical quantities of this model are the effective masses and the size of the ring $2\pi R$. In order to investigate the spectra of the continuum properly, R must go towards infinity.

We do not expect that on the basis of such a model we can describe a real semiconductor structure quantitatively. However, we are able to explain qualitatively

---

[3] or their linear combination

different kinds of couplings including coupling due to various aspects of the many-body interaction. Another benefit of this model is the possible treatment of disorder by a random spatial arrangement of the site energies [14].

3.2 Selection rules

In this work we consider typical III-V semiconductors, in particular quantum wells. Unlike in bulk material in the quantum well the degeneracy of the heavy- and light-hole valence band is lifted at the center of the Brillouin zone due to reduction of translational symmetry in growth direction. In the previous chapter we introduced the one-dimensional tight-binding semiconductor model, which has been extended to describe also the additional energy level for the light hole. In this way we include the effect of the spatial confinement in growth direction z, which splits the heavy- and light-hole bands and leads to the band structure for the heavy and light hole in xy-direction (Eq. (3.3)). Our model represents a kind of extended quantum wire system (replacing the two-dimensional quantum well).

In Chapter 10 we discuss the influence of band mixing effects on 2D-FTS. The splitting of the bands can be identified due to heavy- and light-hole excitonic resonances. However, even without splitting, there would be separate excitonic heavy- and light-hole resonances due to the different masses of the heavy and light holes. Band splitting just adds to this shift, thus the resonances are further apart. With band mixing included it is no longer possible to assign a given resonance a pure heavy- or light-hole character.

Since we consider weak excitation close to the fundamental gap at low temperature, the optical transitions take place close to the Γ-point. By accounting for spin-orbit coupling we form the energy scheme at the Γ-point as shown in Fig. 3.2, i.e we define the selection rules. Due to spin degeneracy we have two kinds of three-energy level systems, each is characterized by one electron and two hole states with corresponding angular momentum j_z-quantum numbers. For the Γ-point this leads

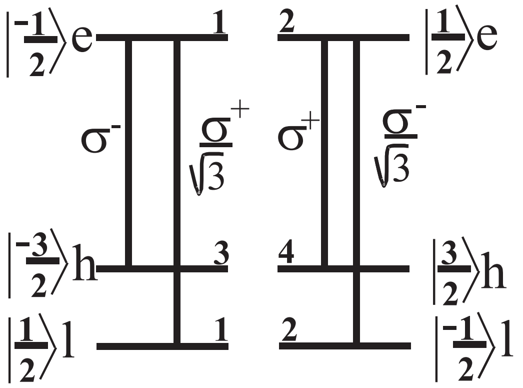

Figure 3.2: Dipole transitions describing optical excitations of heavy- and light-hole excitons in the bulk.

to the following dipole-matrix elements, where we here give their absolute values for the bulk situation:

$$\begin{aligned}
\vec{\boldsymbol{\mu}}_{ij}^{31} &= \delta_{ij}\mu_0\vec{\boldsymbol{\sigma}}^{-} = \delta_{ij}\frac{\mu_0}{\sqrt{2}}\begin{pmatrix} 1 \\ -i \end{pmatrix} \\
\vec{\boldsymbol{\mu}}_{ij}^{32} &= \vec{\boldsymbol{\mu}}_{ij}^{41} = 0 \\
\vec{\boldsymbol{\mu}}_{ij}^{42} &= \delta_{ij}\mu_0\vec{\boldsymbol{\sigma}}^{+} = \delta_{ij}\frac{\mu_0}{\sqrt{2}}\begin{pmatrix} 1 \\ i \end{pmatrix} \\
\vec{\boldsymbol{\mu}}_{ij}^{11} &= \delta_{ij}\frac{\mu_0}{\sqrt{3}}\vec{\boldsymbol{\sigma}}^{+} = \delta_{ij}\frac{\mu_0}{\sqrt{6}}\begin{pmatrix} 1 \\ i \end{pmatrix} \\
\vec{\boldsymbol{\mu}}_{ij}^{21} &= \vec{\boldsymbol{\mu}}_{ij}^{12} = 0 \\
\vec{\boldsymbol{\mu}}_{ij}^{22} &= \delta_{ij}\frac{\mu_0}{\sqrt{3}}\vec{\boldsymbol{\sigma}}^{-} = \delta_{ij}\frac{\mu_0}{\sqrt{6}}\begin{pmatrix} 1 \\ -i \end{pmatrix} .
\end{aligned} \tag{3.9}$$

Here μ_0 is the modulus of the matrix element for the heavy-hole transition. We assume the propagation of the light field to be in the z-direction.

These selection rules play an important role in the investigation of the polarization effects in the sample if different polarized excitation pulses are applied. In this work, we will consider co-circular, co-linear and cross-linear polarization directions. The selection rules show that such excitation situations can be viewed as two independent two level system (co-circular excitation) and two coupled three level systems (linear excitation) for non-interaction particles (see Chapter 4).

Chapter 4

Non-interacting particles

Before we present results of the numerical calculations for the semiconductor model, in this chapter we begin with an analysis of the 2D-FTS amplitude $|E(\omega_t, \pm\omega_\tau, T)|$ and real part $\Re[E(\omega_t, \pm\omega_\tau, T)]$ spectra for a model system, where the many-body interaction is neglected. The calculation on the basis of our extended interacting one-dimensional tight-binding model, which is discussed in Chapter 3.1 yields, two coupled resonances corresponding to "heavy-hole", i.e lower-[1] energy "excitonic" transitions and "light-hole", i.e. higher-energy "excitonic" transition. This can be roughly modeled by a level-system with non-interacting particles with the correct selection rules. The advantage of studying a non-interacting system is that on hand of this model system, containing the selection rules, we can investigate the dependence of 2D-FTS spectra on polarization direction of the excitation pulses and compare with analytical results, thus gaining a first insight into the origin of the spectral signatures. In particular we consider co-circular, co-linear and cross-linear excitations.

4.1 Co-circular excitation

We begin with co-circular excitation $\sigma^+\sigma^+\sigma^+$ and denote the corresponding excitation pulses as E_{σ^+}. The excitation pulses are defined in the basis of linear excitation

---

[1] Here, this means the absolute value of the energy.

pulses as following:

$$\begin{gathered}
\boldsymbol{E}_{\sigma^{\pm}} = E_x \pm i * E_y \propto \begin{pmatrix} 1 \\ \pm i \end{pmatrix} , \\
\text{where} \quad \boldsymbol{E}_x \quad \text{and} \quad \boldsymbol{E}_y \quad \text{are} \\
\boldsymbol{E}_x \propto \begin{pmatrix} 1 \\ 0 \end{pmatrix} \qquad \text{and} \quad \boldsymbol{E}_y \propto \begin{pmatrix} 0 \\ 1 \end{pmatrix} .
\end{gathered} \tag{4.1}$$

The polarizations and dipole-matrix elements are defined in the same way. In the following we confine ourselves to the P_{σ^+} polarization case.

We study the polarization dependence of the non-rephasing and rephasing mode of 2D-FTS both analytically for δ-pulse excitation and numerically for Gaussian pulses. For both modes we solve the Optical Bloch Equations for the level system (see Appendix A) and explicitly consider the vector character of the light field (Eq. (4.1)), the polarizations and the dipole-matrix elements.

As a result for δ-pulse excitation we obtain for the non-rephasing mode the macroscopic polarization $P_{\sigma^+}(t,\tau,T)$ (Here and in the following we are omitting the irrelevant amplitude of the electric excitation field, which simply appears as a factor in third order η_0^3.)

$$\begin{aligned}
P_{\sigma^+}(t,\tau,T) \;\; = \;\; & -\frac{2i}{\sqrt{2}\hbar^3} e^{i(k_c+k_b-k_a)} \Theta(t-T)\Theta(T)\Theta(-\tau) \\
& \left[\begin{pmatrix} 1 \\ i \end{pmatrix} \mu_1^4 e^{-i(\omega_1 - i\hbar^{-1}\gamma_1)(t-\tau-T)} + \begin{pmatrix} 1 \\ i \end{pmatrix} \mu_2^4 e^{-i(\omega_2 - i\hbar^{-1}\gamma_2)(t-\tau-T)} \right] ,
\end{aligned} \tag{4.2}$$

where $\tau \leq 0$, $T \geq 0$ and $\mu_{1(2)}$ are the moduli of the corresponding dipole-matrix elements. The dephasing time for the resonance with lower frequency ω_1 (higher frequency ω_2) is represented by the rates $T_1^{-1} = \hbar^{-1}\gamma_1$ ($T_2^{-1} = \hbar^{-1}\gamma_2$). Thus the analytical results for δ-pulse excitation leads after two Fourier transformations to 2D-FTS, which will show two peaks at the diagonal.

Figure 4.1 (upper row) shows the numerical results for the non-rephasing mode for Gaussian excitation pulses: amplitude and real-part 2D-FTS. For simplification we take T to be zero and to minimize the influence of the excitation conditions we center the pulses between the resonances. The dipole-matrix elements and dephasing times are taken to be the same for both resonances.

As we expect from the selection rules (see Fig. 3.2), 2D-FTS for the co-circular excitation shows two independent resonances. This means that this situation can be modeled by two independent two level systems. The real-part spectrum for such a system shows mostly absorptive character and minor discrepancies are due to the sensitivity of the non-rephasing mode to the temporal overlap with the excitation pulse. By taking extremely short pulses these discrepancies are vanishing (see Chapter 4.3). Here we do not show the imaginary part 2D-FTS, which has a dispersive character according to the Kramers-Kronig relations.

The analytical results obtained for δ-excitation pulses for the rephasing mode are

$$\begin{aligned} P_{\sigma^+}(t,\tau,T) &= -\frac{2i}{\sqrt{2}\hbar^3} e^{i(k_c+k_b-k_a)} \Theta(t-T)\Theta(T)\Theta(\tau) \\ & \Bigg[\begin{pmatrix} 1 \\ i \end{pmatrix} \mu_2^4 e^{-i(\omega_2 - i\hbar^{-1}\gamma_2)(t-T)} e^{i(\omega_2 + i\hbar^{-1}\gamma_2)\tau} \\ & + \begin{pmatrix} 1 \\ i \end{pmatrix} \mu_1^4 e^{-i(\omega_1 - i\hbar^{-1}\gamma_1)(t-T)} e^{i(\omega_1 + i\hbar^{-1}\gamma_1)\tau} \Bigg], \end{aligned} \tag{4.3}$$

where now $\tau \geq 0$ and $T \geq 0$. This expression clearly explains the notion rephasing mode. Since for $t - T = \tau > 0$ the phase factors are unity independent of the excitation frequencies ω_1, ω_2. This is not the case for the non-rephasing mode, since $\tau < 0$.

The numerical results for the rephasing-mode amplitude and real-part 2D-FTS are shown in Fig. 4.1 (lower row). As it is expected from the analytical results, the rephasing mode 2D-FTS yields two peaks at the diagonal. The oscillator strength of those peaks for the rephasing and non-rephasing mode is of the same order (Fig. 4.1 left column). The real-part spectrum displays a purely absorptive character for the rephasing mode (Fig. 4.1 lower right corner), and slightly dispersive character for

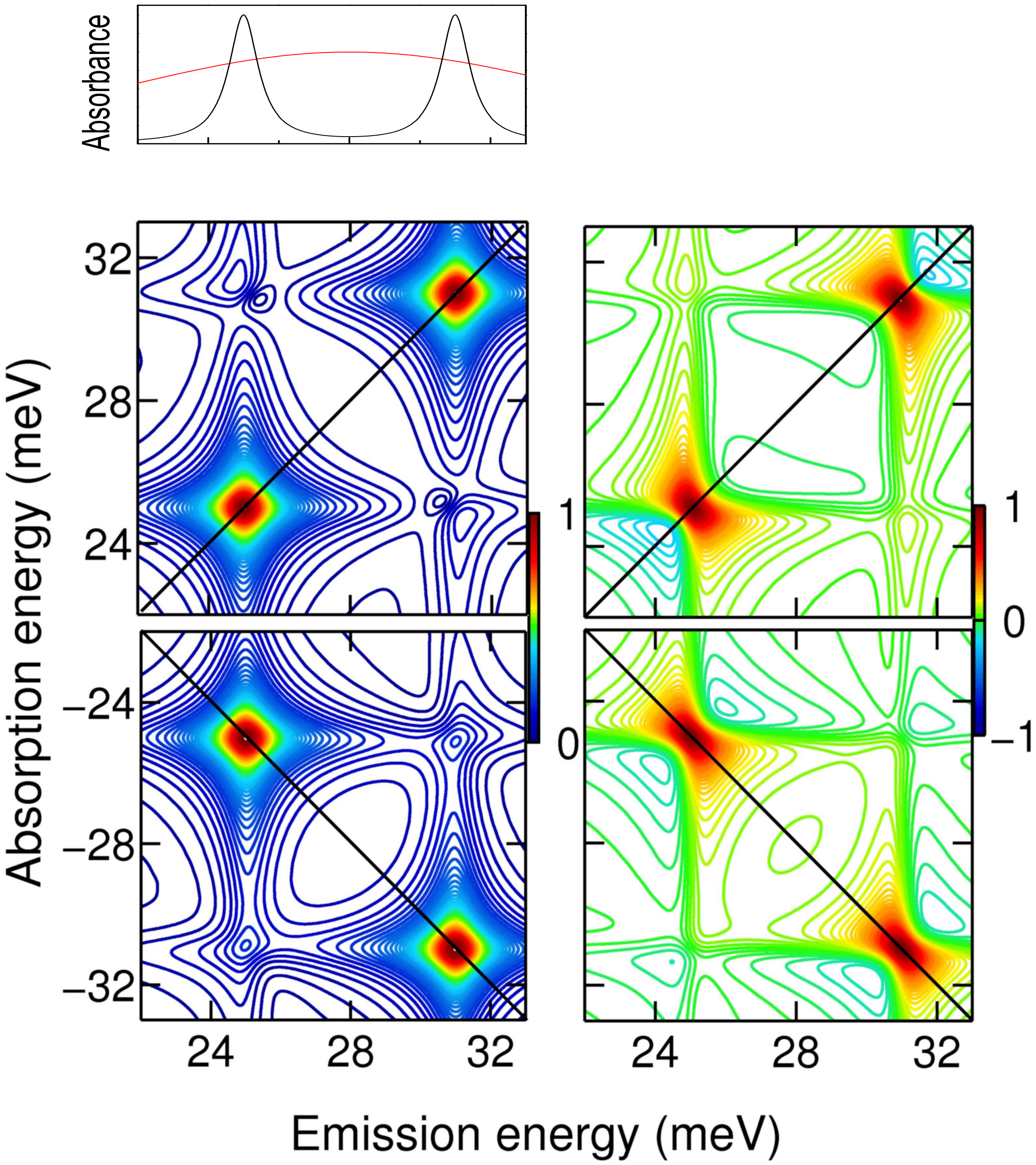

Figure 4.1: Normalized amplitude (left column) and real-part (right column) 2D-FTS for the co-circular polarization case. The upper row depicts the non-rephasing mode and the lower the row rephasing mode. The upper single figure shows the normalized linear spectrum (black line) and the excitation power spectrum (red line) of the Gaussian pulse with corresponding width of 100 fs. Here parameter set I has been used.

the non-rephasing mode (Fig. 4.1 upper right corner).

Finally, we have seen that in the case of the co-circular excitation pulses the amplitude spectra for rephasing and non-rephasing modes are identical (Fig. 4.1 left column). The oscillator strengths of the peaks are given by the dipole-matrix elements in fourth order and by the overlap with the spectrum of the excitation pulses. Generally, the real-part spectra are more sensitive to this overlap. The real spectrum of the non-rephasing mode for extremely short pulses shows a spectrum that is identical to that of the rephasing mode.

It is also remarkable, and has to be expected, that the well known beating seen in the temporal signals of a FWM-experiment with linearly polarized excitation pulses is not appearing for our level system considered here for the co-circular excitation.

4.2 Linearly polarized excitations

In this chapter we consider the co- and cross-linear excitation (the excitation fields are given in Eq. (4.1)) for the non-rephasing mode and compare them with that of the rephasing mode 2D-FTS. The essential difference with respect to the co-circular excitation relies on the selection rules. It is obvious that in the linear excitation situation the system can no longer be considered as being a simple pair of two independent two-level systems. Since in the linear excitation situation we excite all spin-dependent transitions simultaneously, instead of the previously uncoupled resonances in the co-circular case they are now coupled due to a common state. We are investigating such kind of coupling for a simple level system in this chapter, again analytically for δ-excitation pulses and numerically for Gaussian pulses. A second question arises here: How does the beating of the temporal FWM-signal show up in 2D-FTS?

We start with co-linear XXX polarization for the non-rephasing mode. The analytical result for $\delta-$excitation pulses is (see Appendix A):

$$\begin{aligned} P_x(t,\tau,T) &= -\frac{i}{2\hbar^3} e^{i(k_c+k_b-k_a)} \Theta(t-T)\Theta(T)\Theta(-\tau) \begin{pmatrix} 1 \\ 0 \end{pmatrix} \\ & \Big[\mu_2^2 e^{-i(\omega_2 - i\hbar^{-1}\gamma_2)(t-T)} \big(e^{i(\omega_2 - i\hbar^{-1}\gamma_2)\tau} [2\mu_2^2 + \mu_1^2 e^{-i\Delta\omega T}] + \mu_1^2 e^{i(\omega_1 - i\hbar^{-1}\gamma_1)\tau} \big) \\ &+ \mu_1^2 e^{-i(\omega_1 - i\hbar^{-1}\gamma_1)(t-T)} \big(e^{i(\omega_1 - i\hbar^{-1}\gamma_1)\tau} [2\mu_1^2 + \mu_2^2 e^{i\Delta\omega T}] + \mu_2^2 e^{i(\omega_2 - i\hbar^{-1}\gamma_2)\tau} \big) \Big] , \end{aligned} \tag{4.4}$$

where $\tau \leq 0$, $T \geq 0$ and $\hbar\Delta\omega = \hbar(\omega_2 - \omega_1)$ is the energy offset between the two resonances.

We perform the Fourier transformations with respect to t and τ. In contrast to the co-circular situation the diagonal terms are now getting mixed character, the oscillator strength for the lower (higher) peak is given by $2\mu_1^4 + \mu_1^2\mu_2^2 e^{i\Delta\omega T}$ $(2\mu_2^4 + \mu_1^2\mu_2^2 e^{-i\Delta\omega T})$. The important issue is that the diagonal terms oscillate with the frequency corresponding the energy separation of the two resonances. Thus the beating of the diagonal peaks with the period $2\pi/\Delta\omega$ appears in the frequency domain for the non-rephasing mode. As a new feature the non-diagonal terms emerge with the oscillator strength given by the product of the dipole-matrix element of both resonances $\mu_1^2\mu_2^2$.

On this stage we omit the T-dependence by taken T=0 for simplicity and compare the oscillator strengths with those of our numerical results (Fig. 4.2, upper row). In our numerical simulations the dipole-matrix elements are taken to be equal[2]. Thus in the amplitude 2D-FTS we obtain diagonal peaks with the oscillator strength of $3 * \mu^4$ and the non-diagonal ones are given by μ^4. The real part spectrum shows almost pure absorptive character, which agrees with the co-circular excitation case.

We now consider the amplitude 2D-FTS for the rephasing mode displayed in Fig. 4.2 (lower row). The peak distribution and the oscillator strengths differ from that of the non-rephasing mode. The reason for this discrepancy lies in the different

---

[2] $\mu_1 = \mu_2 = \mu$

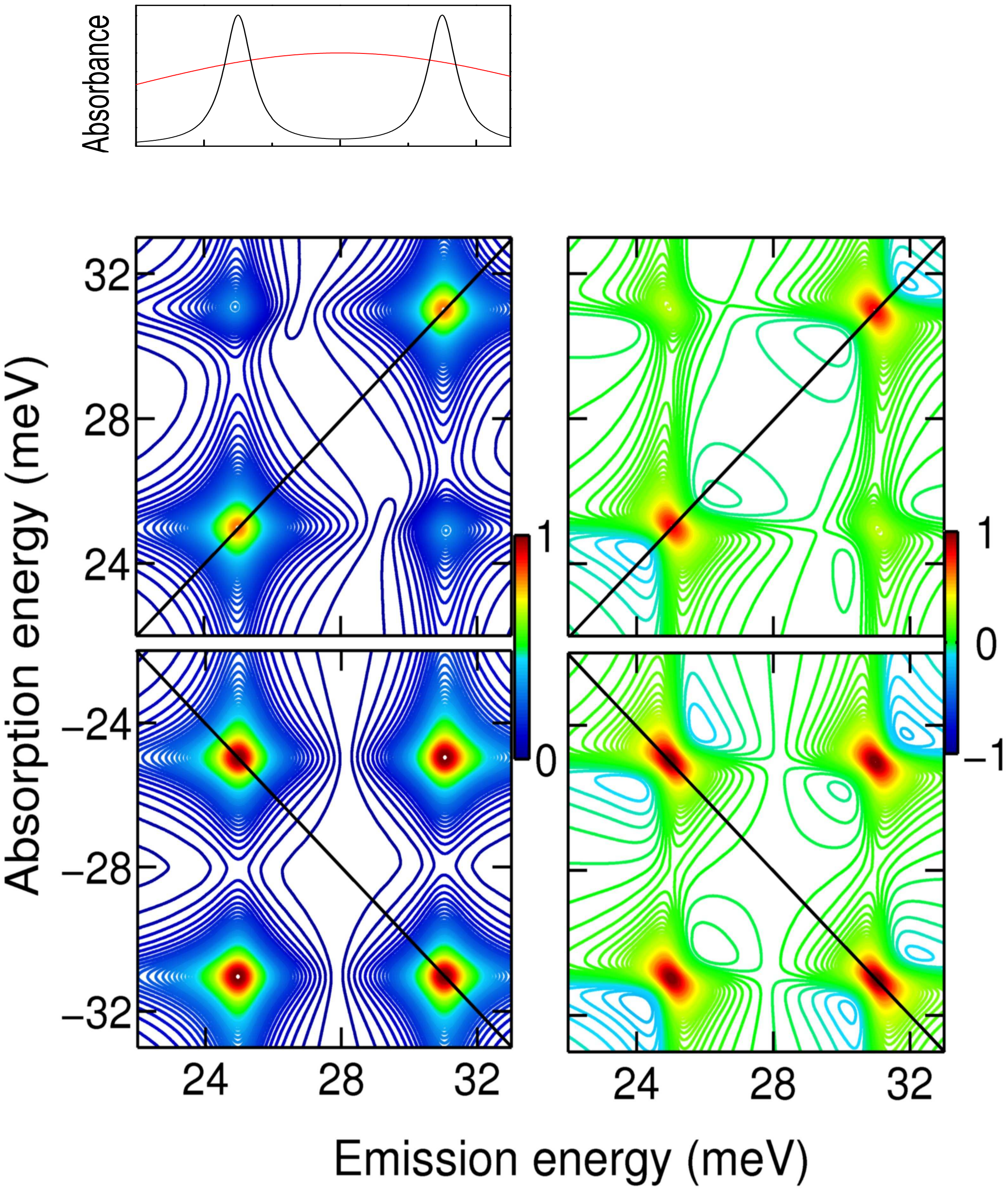

Figure 4.2: Normalized amplitude (left column) and real part (right column) 2D-FTS for the co-linear polarization case. The upper row depicts the non-rephasing mode and the lower row the rephasing mode. The upper single figure shows the normalized linear spectrum (black line) and the excitation power spectrum (red line) of the Gaussian pulse with corresponding width of 100 fs. Here the parameter set I has been used.

underlying physics for the rephasing and non-rephasing mode. In order to clarify this point we solve the Optical Bloch Equations analytically for δ-pulse excitation, as it is shown in Appendix A. The result is:

$$\begin{aligned} P_x(t,\tau,T) &= -\frac{i}{2\hbar^3} e^{i(k_c+k_b-k_a)} \Theta(t-T)\Theta(T)\Theta(\tau) \begin{pmatrix} 1 \\ 0 \end{pmatrix} \\ & \Big[\mu_2^2 e^{-i(\omega_2 - i\hbar^{-1}\gamma_2)(t-T)} (2\mu_2^2 e^{i(\omega_2+i\hbar^{-1}\gamma_2)\tau} + \mu_1^2 e^{i(\omega_1+i\hbar^{-1}\gamma_1)\tau}(1+e^{-i\Delta\omega T})) \\ &+ \mu_1^2 e^{-i(\omega_1 - i\hbar^{-1}\gamma_1)(t-T)} (2\mu_1^2 e^{i(\omega_1+i\hbar^{-1}\gamma_1)\tau} + \mu_2^2 e^{i(\omega_2+i\hbar^{-1}\gamma_2)\tau}(1+e^{i\Delta\omega T}))\Big], \end{aligned} \tag{4.5}$$

where now $\tau \geq 0$ and $T \geq 0$.

By taking T=0 and for equal dipole-matrix elements μ_1=μ_2=μ we obtain the oscillator strengths of the diagonal terms for the rephasing (non-rephasing) mode proportional to $2\mu^4$ ($3\mu^4$) and the strengths of the non-diagonal terms for the rephasing (non-rephasing) mode is $\sim 2\mu^4(\mu^4)$. In our numerical calculations (Fig. 4.2), the ratio between the maxima of the diagonal and non-diagonal peaks slightly differs from the analytical predictions for the non-rephasing mode and shows a good agreement with the analytical results for the rephasing mode. We will address this slight discrepancy in Chapter 4.3.

The other interesting feature of the rephasing mode is that the beating is now present in the non-diagonal terms. If we take $T > 0$, the oscillator strengths of the non-diagonal peaks at lower (higher) emission energy is proportional to $\mu^4[1+e^{i\Delta\omega T}]$ ($\mu^4[1+e^{-i\Delta\omega T}]$).

Now we consider the cross-linear excitation YXX. In this situation, similar to the co-linear case we expect both resonances to be coupled due to the common electron state. Figure 4.3 (upper row) shows the numerical results for the non-rephasing mode.

We can expect the distribution of the peaks to be the same as for the co-linear situation. The analytical calculations for δ-excitation pulses leads for the

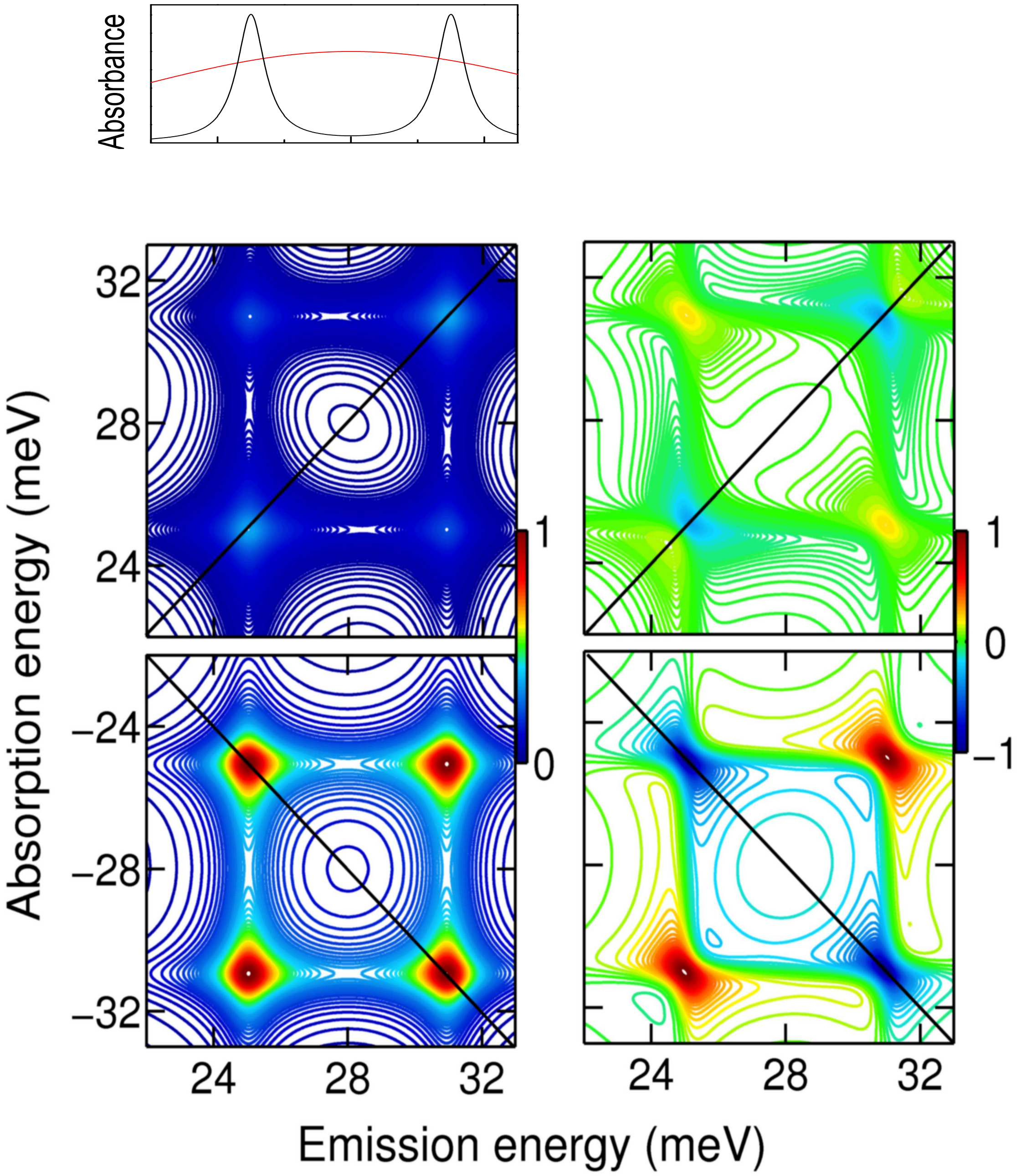

Figure 4.3: Normalized amplitude (left column) and real part (right column) 2D-FTS for the cross-linear polarization case. The upper row depicts the non-rephasing mode and the lower row the rephasing mode. The upper single figure shows the normalized linear spectrum (black line) and the excitation power spectrum (red line) of the Gaussian pulse with corresponding width of 100 fs. Here the parameter set I has been used.

non-rephasing mode to

$$\begin{aligned} P_y(t,\tau,T) &= -\frac{i}{2\hbar^3} e^{i(k_c+k_b-k_a)} \Theta(t-T)\Theta(T)\Theta(-\tau) \begin{pmatrix} 0 \\ 1 \end{pmatrix} \\ & \Big[-\mu_2^2 e^{-i(\omega_2 - i\hbar^{-1}\gamma_2)(t-T)} \big(e^{i(\omega_2 - i\hbar^{-1}\gamma_2)\tau} [2\mu_2^2 - \mu_1^2 e^{-i\Delta\omega T}] - \mu_1^2 e^{i(\omega_1 - i\hbar^{-1}\gamma_1)\tau} \big) \\ &- \mu_1^2 e^{-i(\omega_1 - i\hbar^{-1}\gamma_1)(t-T)} \big(e^{i(\omega_1 - i\hbar^{-1}\gamma_1)\tau} [2\mu_1^2 - \mu_2^2 e^{i\Delta\omega T}] - \mu_2^2 e^{i(\omega_2 - i\hbar^{-1}\gamma_2)\tau} \big) \Big] , \end{aligned} \tag{4.6}$$

where $\tau \leq 0$ and $T \geq 0$. For simplicity we take T=0 and identical dipole-matrix elements μ, and compare with the co-linear excitation case for the non-rephasing mode (cp. Eq. (4.6) and (4.4)). The oscillator strengths for the diagonal peaks in the cross-(co-)linear situation are proportional to $-\mu^4$ ($\sim 3\mu^4$), for the non-diagonal terms $\sim \mu^4$ (μ^4). This difference occurs due to interchanging of the signs, which can be identified also in the real-part 2D-FTS. The diagonal peaks of the real-part 2D-FTS for the cross-linear situation show a pronounced dispersive character, whereas for the co-linear case it is mostly absorptive. The non-diagonal peaks for both polarization cases have mostly absorptive character.

As a different behavior was found for the rephasing mode for the co-linear excitation, we also expect a different behavior for the cross-linear situation.

We compare again for the simplified situation T=0, identical dipole-matrix elements the non-rephasing and the rephasing modes (see upper and lower row of Fig. 4.3). The peak distribution has changed. For further discussion we need to compare the analytical result, which is given here for the rephasing mode:

$$\begin{aligned} P_y(t,\tau,T) &= -\frac{i}{2\hbar^3} e^{i(k_c+k_b-k_a)} \Theta(t-T)\Theta(T)\Theta(\tau) \begin{pmatrix} 0 \\ 1 \end{pmatrix} \\ & [-\mu_2^2 e^{-i(\omega_2 - i\hbar^{-1}\gamma_2)(t-T)} (2\mu_2^2 e^{-i(\omega_2 - i\hbar^{-1}\gamma_2)\tau} - \mu_1^2 e^{-i(\omega_1 - i\hbar^{-1}\gamma_1)\tau} (1 + e^{-i\Delta\omega T})) \\ &- \mu_1^2 e^{-i(\omega_1 - i\hbar^{-1}\gamma_1)(t-T)} (2\mu_1^2 e^{-i(\omega_1 - i\hbar^{-1}\gamma_1)\tau} - \mu_2^2 e^{-i(\omega_2 - i\hbar^{-1}\gamma_2)\tau} (1 + e^{i\Delta\omega T}))], \end{aligned} \tag{4.7}$$

with the result for the non-rephasing mode (Eq. (4.6)). We carry out the same simplification procedure as it has been done before for the rephasing mode and compare it with the numerical results shown in Fig. 4.3 (lower row).

We focus on the rephasing and non-rephasing modes (Fig. 4.3, left column). The oscillator strengths of the diagonal and non-diagonal peaks are proportional to $-2\mu^4$ for the rephasing mode, whereas for the non-rephasing $\sim -\mu^4$. Thus the peaks for the non-rephasing mode are suppressed by a factor of 2 (Fig. 4.3, left column). This yields the same peak distribution for the rephasing mode amplitude 2D-FTS for both linear excitations (lower row, Fig. 4.3 and 4.2). The non-rephasing mode (Fig. 4.3, upper row) shows the discrepancies between the analytical and numerical results for the peak distribution. At the same time a change of the signs in the analytical results for the cross-linear case shows up in the real-part spectrum. Thus the real part contains additional information. The diagonal and non-diagonal peaks for the cross-linear situation in the real-part 2D-FTS have absorptive and emittive character, respectively (Fig. 4.3, right lower corner), whereas for the co-linear excitation we see absorptive character (Fig. 4.2, right lower corner). Due to the complexity of the analytical results, we do not show the analytical expression for the real part here.

In the next chapter we show the pulse dependence of the non-rephasing mode for the co- and cross-linear situation.

4.3 Pulse dependence

This chapter aims at an explanation of the discrepancies between the analytical and numerical results occurring for the non-rephasing mode in Chapter 4.2. For this purpose we apply in our numerical simulation extremely short Gaussian pulses in order to approach the δ-excitation pulses (the power spectrum of the excitation pulse is shown in Fig. 4.4, upper single figure).

We begin with the co-linear excitation shown in Fig. 4.4 (upper row). In general the peak distribution in comparison to Fig. 4.2 (upper row) remains the same, but the ratio between the maxima of the diagonal and non-diagonal peaks slightly

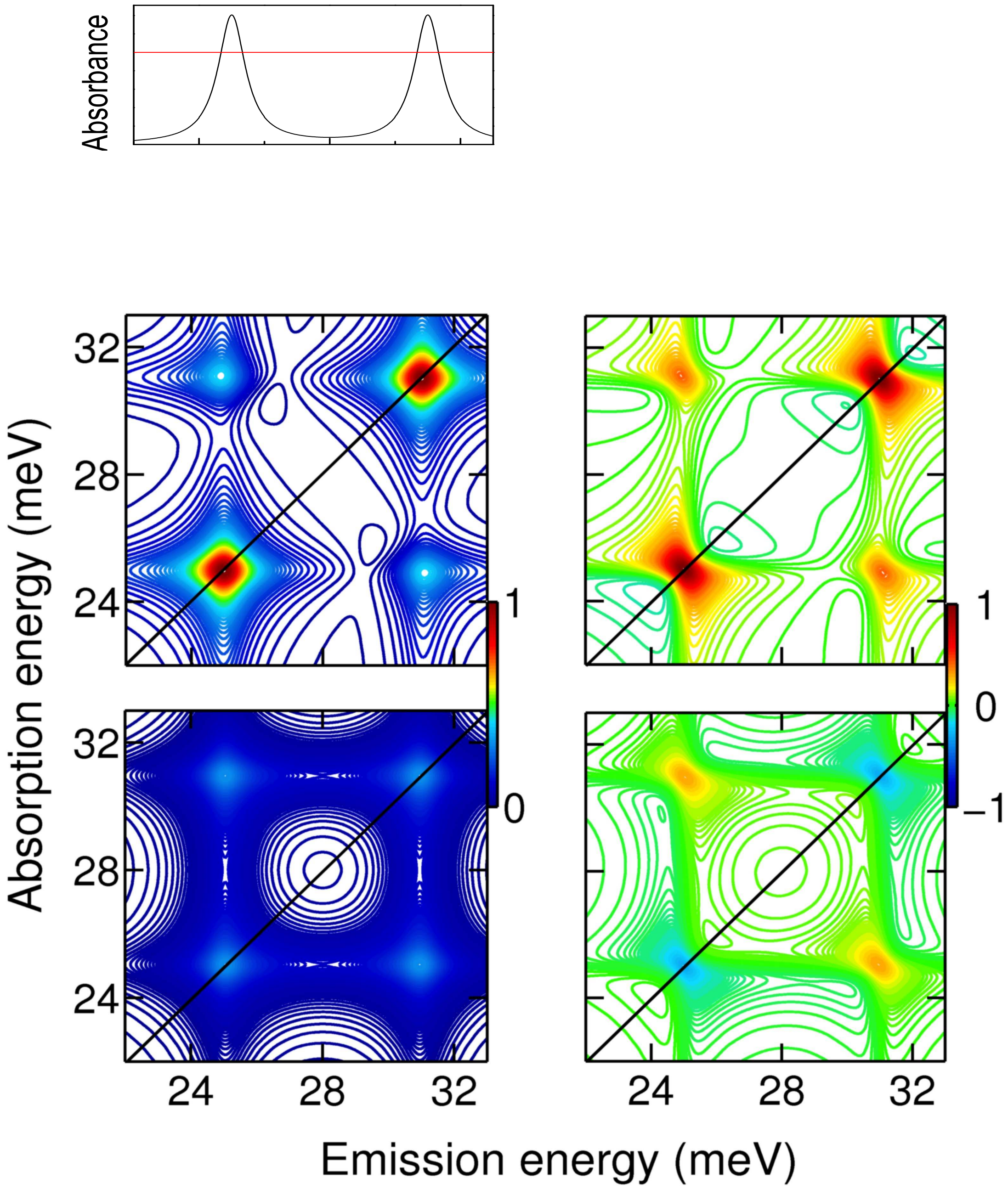

Figure 4.4: Normalized amplitude (left column) and real part (right column) 2D-FTS for the non-rephasing mode. The upper row depicts co-linear and the lower row cross-linear excitation. The upper single figure shows the normalized linear spectrum (black line) and the excitation power spectrum (red line) of the Gaussian pulse with corresponding width of 5 fs. Here the parameter set II has been used.

changes. By taking extremely short pulses (i.e. 5 fs here), the ratio in the Fig. 4.4 (upper row) now agrees with the analythical results given by Eq. (4.4). Additionally, the real-part 2D-FTS for extremely short pulses is getting a pronounced absorptive character, Fig. 4.4 (upper right corner). Obviously, the analytical results for δ-pulses provide only a rough estimate for the real situation, where Gaussian pulses are used. We can conclude, that the amplitude and the real-part 2D-FTS for the non-rephasing mode is more sensitive to the overlap with the excitation pulse than the rephasing mode. We will discuss this point in more detail at the end of this chapter.

It is interesting to look at the cross-linear excitation shown in Fig. 4.4 (lower row). We compare this amplitude 2D-FTS for the pulse width of 5 fs with the amplitude 2D-FTS for the pulse width of 100 fs (Fig. 4.3, upper row). The distribution of the oscillator strengths of the peaks has been changed by taking extremely short excitation pulses. Here the dipole-matrix elements are taken to be identical, and for $T = 0$ the analytical result yields the oscillator strength to be proportional to μ^4 (Eq. (4.6)), which agrees now with our numerical results shown in Fig. 4.4. The real part 2D-FTS for the excitation pulse width of 100 fs has clearly shown dispersive character, which is in contrast to the emittive (for the non-diagonal peaks to the absorptive) character for the excitation pulse width of 5 fs (Fig. 4.3, upper row and Fig. 4.4 lower row). This illustrates that in case of the cross-linear excitation the changes of the 2D-FTS due to overlap with the excitation pulses are more significant than for the co-linear case.

Usually in the 2D-FTS experiments available to us 100 fs pulse width is used. It is therefore important to show on hand of the simple model that the numerical results can not be interpreted by the analytical results for the non-rephasing case, in particular for the cross-linear excitation case. It is remarkable, that the non-rephasing mode seems to be more sensitive than the rephasing mode. This fact can be proved by, e.g., the dependence on the central excitation energy.

We consider the co-circular case for simplicity. In order to investigate the dependence of the 2D-FTS on the tuning of the central excitation energy, we focus on the rephasing and non-rephasing mode.

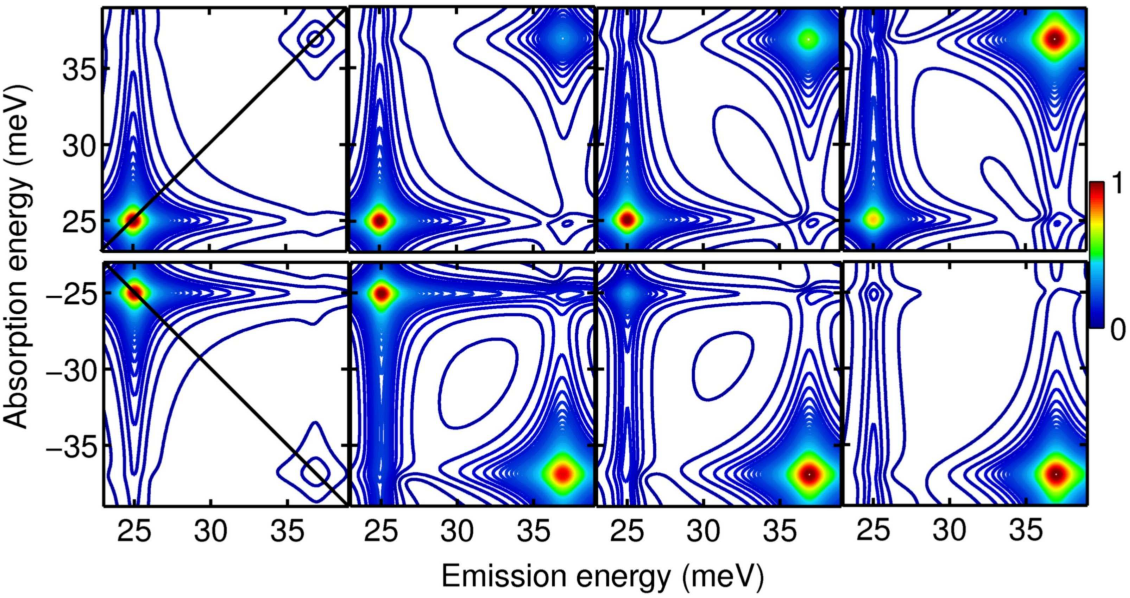

Figure 4.5: Normalized amplitude spectra calculated for the co-circular 2D-FTS. The upper line is the non-rephasing mode, the lower line is the rephasing mode for the energies tuned to (from left to right): 30, 37, 40, 45 meV. The parameter set III has been used.

Figure 4.5 illustrates the non-rephasing and rephasing modes of the amplitude 2D-FTS for different excitation energies. We will consider the set of figures in Fig. 4.5 starting from the left. The first left column corresponds to the case where the excitation pulses have been centered at the "h exciton", therefore this peak is very strong. By the excitation at the "l exciton", the oscillator strength of this peak for the non-rephasing mode increases and the strength of the "l exciton" of the rephasing mode is even comparable to that of the "h excitonic" peak. Tuning slightly above the "l exciton", the pulse overlap with the "h exciton" decreases, which results in a more pronounced "l excitonic" peak in non-rephasing case. However, the "h exciton" is still stronger than the "l exciton". Surprisingly, the rephasing mode shows, in contrast to the non-rephasing mode, much stronger oscillator strength of "l excitonic" peak than of the "h" one. This fact points at an enhanced sensitivity of the rephasing mode if compared to the non-rephasing one. The figures on the right hand side of Fig. 4.5 correspond to excitation at the energy, which is far above the "l excitonic" peak. This set of figures demonstrate fundamental differences between the rephasing and non-rephasing mode.

Thus the a priori statement that the non-rephasing mode is more sensitive to the spectral overlap with the excitation pulses has not been proved in this particular case. However, this analysis points out the fundamental difference between the modes, which needs further detailed consideration.

In Chapter 8.2 we discuss how the overlap of the pulses in the frequency domain influences the signatures of 2D-FTS for the semiconductor nanostructures.

4.4 Conclusions

In Chapter 4 the polarization dependence of the amplitude and the real-part 2D-FTS for rephasing and non-rephasing modes has been studied. We found that the co-circular excitation can be modeled by two independent level systems, whereas the linear excitations, due to coupled spin-dependent transitions, have to be modeled by two three-level systems. The diagonal peaks in both cases are identified as resonances of the system and the non-diagonal as the coupling between them, which allows us to study different kinds of coupling separately, including that due to the many-particle interaction (Part II).

By comparing co- and cross-linear excitation, we found that even for non-interacting particles they show different spectra. This difference could not be identified in the amplitude 2D-FTS, but only in the real-part spectra.

We have investigated the dependence on excitation condition, namely the spectral overlap between the pulse and the peaks of the amplitude and real-part 2D-FTS. It has been demonstrated that an essential difference exists between the non-rephasing and rephasing modes. In particular, the rephasing mode shows stronger dependence of 2D-FTS on the excitation energy due to the overlap between the excitation pulse with the resonances.

On hand of an analytical calculation we have shown how beating is represented in the frequency domain for 2D-FTS, which is well known from normal FWM-experiments in the time domain. It has been proven that the rephasing mode corresponds in a certain sense to the normal FWM-experiment and beating shows up at the non-diagonal peaks. It has been shown that beating appears even if the pulses are interchanged (non-rephasing mode). It is remarkable that for the non-rephasing mode the diagonal peaks are beating.

Part II

Interacting particles

Chapter 5

General remarks

The level models have been useful to understand the basic principles of the 2D-FTS method. In the second part of this work we include the many-body effects and investigate the real quantum well systems by 2D-FTS. It is well known that non-linear signals show a strong influence of many-body effects [4, 5].

In the following we demonstrate the theory which includes Coulomb effects beyond the Hartree-Fock approximation, i.e Coulomb correlations (Chapter 6). We show how by using 2D-FTS the weight of different kinds of couplings can be estimated, namely those due to a common state, coupling of exciton to continuum, and exciton-exciton couplings (Chapter 7).

We demonstrate some of the characteristics of the 2D-FTS method such as the dependence on details of the excitation (Chapter 8) and the influence of material parameters on the signature of 2D-FTS (Chapter 10). A special feature of this method is the additional phase information due to the real and imaginary parts, which is discussed in Chapter 9.

One of the promising applications of 2D-FTS is the determination of the inhomogeneous broadening by only measuring the rephasing and non-rephasing mode. This method is applied to a real GaAs quantum well system and compared with the theory in Chapter 11.

In Chapter 12 we illustrate the fundamental and essential difference between the CES and 2D-FTS methods.

Chapter 6

Semiconductor Bloch Equations

In this chapter we treat the optical excitation up to third order in the $\chi^{(3)}$ -limit in the coherent regime. For this propose we apply the one-dimensional tight-binding model given in Chapter 3.1.

We define the Hamiltonian tight-binding matrices T^e and T^v with diagonal elements

$$\begin{aligned} T^e_{ii} &= \epsilon^e_i, \\ T^v_{ii} &= \epsilon^{h(l)}_i, \end{aligned} \tag{6.1}$$

and non-diagonal elements

$$\begin{aligned} T^e_{ij} &= J^e, \quad \text{for } i,j \text{ nearest neighbors}, \\ T^v_{ij} &= J^{h(l)}, \quad \text{for } i,j \text{ nearest neighbors}, \\ T^e_{ij} &= T^v_{ij} = 0, \quad \text{else}, \end{aligned} \tag{6.2}$$

respectively, i.e., the non-diagonal elements are nonzero only if i, j denote nearest neighbor sites. The superscripts ^{e} and ^{v} denote the two electron states and the four (light- and heavy-) hole states, resp.

The total Hamiltonian characterizes the system of interacting particles and its optical excitation in the semiconductor material. It is given by:

$$\hat{H} = \hat{H}_0 + \hat{H}_C + \hat{H}_L, \tag{6.3}$$

where $\hat{H}_0$ is a free particle Hamiltonian, $\hat{H}_C$ represents the Coulomb Hamiltonian and $\hat{H}_L$ denotes the light-matter interaction [15].

We begin with the single-particle Hamiltonian $\hat{H}_0$, which describes the kinetics of the electrons and holes:

$$\hat{H}_0 = \sum_{i,j=1}^{N} \sum_{e} T^e_{ij} c^{e\dagger}_i c^e_j + \sum_{i,j=1}^{N} \sum_{v} T^v_{ij} d^{v\dagger}_i d^v_j, \tag{6.4}$$

where c and d are electron and hole operators. Periodic boundary conditions are applied, such that the system is a ring with radius R and circumference $Na = 2\pi R$, where N is the number of sites.

The interaction between electrons and holes on different sites is described by the monopole-monopole interaction [16] , which is represented by the Hamiltonian $\hat{H}_C$:

$$\hat{H}_C = \frac{1}{2} \sum_{ij} (\sum_{e'} c^{e'\dagger}_i c^{e'}_i - \sum_{v'} d^{v'\dagger}_i d^{v'}_i) V_{ij} (\sum_{e} c^{e\dagger}_j c^e_j - \sum_{v} d^{v\dagger}_j d^v_j). \tag{6.5}$$

The Coulomb matrix is given by:

$$V_{ij} = U_0 \frac{a}{a|i-j| + a_0}, \tag{6.6}$$

where the term a_0 regularizes the potential in order to obtain a finite exciton binding energy [17, 18]. The parameter a is the distance between the sites and U_0 characterizes the strength of the Coulomb interaction.

In order to complete the total Hamiltonian, we define the Hamiltonian H_L, which specifies the dipole interaction with the classical field:

$$\hat{H}_L = -\vec{E}(t) \cdot \hat{\vec{P}}. \tag{6.7}$$

$\vec{E}(t)$ is the external light field treated classically, which consists in our situation of a succession of pulses. Here, $\vec{E}(t)$ is the two-dimensional electric vector field in the plane perpendicular to the propagation direction of the light beam.

We only treat optical dipole transitions. The inter-band polarization operator is given by:

$$\hat{\vec{P}} = \sum_{ijev} \left[\vec{\mu}^{ve}_{ij} d^v_i c^e_j + (\vec{\mu}^{ve}_{ij})^* d^{v+}_i c^{e+}_j \right], \tag{6.8}$$

where $\vec{\mu}_{ij}^{ve}$ are the optical dipole-matrix elements (see Chapter 3.2 for details).

The macroscopic polarization $\hat{\vec{P}}$ is caused by the electric field and formed by the inter-band coherences p_{ij}^{ve} together with the corresponding optical dipole-matrix elements $\vec{\mu}_{ij}^{ve}$, which are taken to be diagonal in the site indices in accordance with the tight-binding model. The expectation value of the microscopical polarization is defined by:

$$p_{ij}^{ve} = \langle d_i^v c_j^e \rangle. \tag{6.9}$$

The p_{ij}^{ve} (p_{ij}^{ve*}) describe the annihilation (creation) of electron-hole pairs (in short: amplitude of the excitons).

We use the Heisenberg picture to calculate the temporal evolution of the inter-band coherence up to third order in the excitation field. The Heisenberg equation [4, 15, 18] for the polarization has the following form:

$$-i\hbar\ \partial_t p_{12}^{ve} = \langle\ [H, d_1^v c_2^e]\ \rangle. \tag{6.10}$$

Additionally, we consider the four-point expectation value, which describes the excitation in second order in the electrical field [19] and contains the many-particle correlations up to third order in the excitation field:

$$B_{1324}^{v_1 e v e_2} = -\langle d_1^{v_1} d_2^{v} c_3^{e} c_4^{e_2} \rangle. \tag{6.11}$$

The physical meaning of the inter-band coherence p_{ij}^{ve} is the two-particle (exciton) amplitude, and $B_{1324}^{v_1 e v e_2}$ corresponds to a coherence between two excitonic states [4] including correlations between them. Evaluating Eq. (6.10) for p_{ij}^{ve} and $B_{1324}^{v_1 e v e_2}$ we obtain:

$$\begin{aligned} -i\hbar\ \partial_t p_{12}^{ve} &= -\sum_j T_{2j}^{e} p_{1j}^{ve} - \sum_i T_{i1}^{v} p_{i2}^{ve} + V_{12} p_{12}^{ve} \\ &- \sum_{abv'e'} (V_{a2} - V_{a1} - V_{b2} + V_{b1}) [(p_{ba}^{v'e'})^* B_{ba12}^{v'e've}] \\ &+ \mathbf{E}(t) \cdot [(\boldsymbol{\mu}_{12}^{ve})^* - \sum_{abv'e'} ((\boldsymbol{\mu}_{1b}^{ve'})^* (p_{ab}^{v'e'})^* p_{a2}^{v'e} + (\boldsymbol{\mu}_{b2}^{v'e})^* (p_{ba}^{v'e'})^* p_{1a}^{ve'})], \end{aligned} \tag{6.12}$$

and

$$\begin{aligned}-i\hbar\ \partial_t B^{v'e've}_{ba12} &= -\sum_i (T^e_{2i} B^{v'e've}_{ba1i} + T^v_{i1} B^{v'e've}_{bai2} + T^e_{ai} B^{v'e've}_{bi12} + T^v_{ib} B^{v'e've}_{ia12}) \\ &+ (V_{ba} + V_{b2} + V_{1a} + V_{12} - V_{b1} - V_{a2}) B^{v'e've}_{ba12} \\ &- \mathbf{E}(t) \cdot [(\boldsymbol{\mu}^{ve}_{12})^* p^{v'e'}_{ba} + (\boldsymbol{\mu}^{v'e'}_{ba})^* p^{ve}_{12} - (\boldsymbol{\mu}^{ve'}_{1a})^* p^{v'e}_{b2} - (\boldsymbol{\mu}^{v'e}_{b2})^* p^{ve'}_{1a})].\end{aligned} \tag{6.13}$$

In Eq. (6.12), the first term is a kinetic term representing the free rotation with the pair (exciton) energy, the second term is the Coulomb term which includes the correlation term and the Hartree-Fock nonlinearity representing also the renormalization. The last one contains the Pauli-blocking nonlinearity. It is remarkable that in the coherent regime the population is given by the product of the microscopical polarization and its complex conjugated, i.e. in symbolic form pp^*. The equation (6.13) completes the set of the Semiconductor Bloch Equation in the $\chi^{(3)}$-limit in the coherent regime. The kinetic part of the four particle expectation value is shown in the first line. The Coulomb part is presented in the second line (VB, in symbolic form). The inhomogeneous part of Eq. (6.13) is given by the third line, the source term.

In fact, by solving the four-particle equation explicitly, the Coulomb-memory effects are fully included, i.e. the non-Markovian effects are taken into account on the coherent level. It has to be mentioned, that in the coherent regime weak excitation is required. That means that the population dynamics is given by the evolution of the polarization. This approximation has been successfully applied in the interpretation of non-linear optics, see Ref. [4] and the references therein.

Alternatively to Eq. (6.12) and (6.13) we can solve the equation for the microscopical polarization, which contains a pure correlation term. Thus we can investigate the pure Coulomb correlation effects, which cause, for a example, the coupling between h and l exciton for the co-circular excitation situation within the one-dimensional tight-binding model presented in Chapter 3.1. In order to extract the pure correlation term, we take advantage of the definition of the Hartree-Fock approximation [19]. That means, that the pure correlations are presented in the following form:

$$\bar{B}^{v_1 e v e_2}_{1324} = B^{v_1 e v e_2}_{1324} + p^{v_1 e_2}_{14} p^{ve}_{23} - p^{v_1 e}_{13} p^{v e_2}_{24}. \tag{6.14}$$

We rewrite Eqs. 6.12 and 6.13 in the following form:

$$\begin{aligned}
-i\hbar \frac{d}{dt} p^{ve}_{12} &= -\sum_j T^e_{2j} p^{ve}_{1j} - \sum_i T^v_{i1} p^{ve}_{i2} + V_{12} p^{ve}_{12} \\
&+ \sum_{abv'e'} (V_{a2} - V_{a1} - V_{b2} + V_{b1}) [(p^{v'e'}_{ba})^* p^{v'e}_{b2} p^{ve'}_{1a} \\
&\qquad - (p^{v'e'}_{ba})^* p^{v'e'}_{ba} p^{ve}_{12} - (p^{v'e'}_{ba})^* \bar{B}^{v'e've}_{ba12}] \\
&+ \vec{E}(t) \cdot [(\vec{\mu}^{ve}_{12})^* - \sum_{abv'e'} ((\vec{\mu}^{ve'}_{1b})^* (p^{v'e'}_{ab})^* p^{v'e}_{a2} \\
&\qquad + (\vec{\mu}^{v'e}_{b2})^* (p^{v'e'}_{ba})^* p^{ve'}_{1a})],
\end{aligned} \tag{6.15}$$

where the Coulomb term is split now into the Hartree-Fock part (in symbolic presentation it is Vp^*pp) and the pure correlation term ($\bar{B}$).

The equation of motion for $\bar{B}$ is:

$$\begin{aligned}
-i\hbar \frac{d}{dt} \bar{B}^{v'e've}_{ba12} &= -\sum_i (T^e_{2i} \bar{B}^{v'e've}_{ba1i} + T^v_{i1} \bar{B}^{v'e've}_{bai2} \\
&\qquad + T^e_{ai} \bar{B}^{v'e've}_{bi12} + T^v_{ib} \bar{B}^{v'e've}_{ia12}) \\
&+ (V_{ba} + V_{b2} + V_{1a} + V_{12} - V_{b1} - V_{a2}) \bar{B}^{v'e've}_{ba12} \\
&- (V_{ba} + V_{12} - V_{b1} - V_{a2}) p^{ve'}_{1a} p^{v'e}_{b2} \\
&+ (V_{1a} + V_{b2} - V_{b1} - V_{a2}) p^{v'e'}_{ba} p^{ve}_{12}.
\end{aligned} \tag{6.16}$$

Here the forming of the bound and unbound biexcitons, described by the pure correlation terms $\bar{B}^{v'e've}_{ba12}$, is driven by the source term Vpp.

Equations (6.15) and (6.16) are totally equivalent to Eq. (6.12) and (6.13). In this work the equations (6.15) and (6.16) have been numerically evaluated. There are several reasons for this choice. In this chapter, the damping term of the excitonic and biexcitonic state has not been explicitly shown. Indeed, in case of higher order in the excitation field, where the biexcitons occur, it would not be possible to include into the set of the p and B equations the pure biexcitonic damping term (the first reason). Obviously, Eq. (6.15) and (6.16) allows us to investigate in detail the correlation signatures such as bound and unbound biexcitons. It is very important to single out the pure correlation effects for exploring of couplings between h and l exciton (the second reason). It will be shown in the next chapter, that the non-diagonal peaks appear solely because of the correlation term for the co-circular excitation.

Chapter 7

Study of various kinds of couplings

We start from the analysis of 2D-FTS for a semiconductor nanostructure. The well known experiments based on FWM such as measurements of time integrated (TI-), time resolved (TR-) and CES-signals have been applied in the past to semiconductor structures in order to investigate the Coloumb-induced effects [20, 21, 23, 24, 25, 26]. It has been demonstrated [19] that the interaction-induced fields have a dominant influence on TI-, TR-signals.

Here we suggest to use the 2D-FTS method for the investigation of various kinds of couplings, in particular, in a quantum-well system. Many-body effects are included. We classify the couplings due to different orders in the electrical field. For this purpose we apply the Semiconductor Bloch Equations given in Chapter 6 and the procedure outlined in Chapter 2.

We begin with considering the co-circular excitation situation in the rephasing mode. The calculations are based on the one-dimensional tight-binding model (see Chapter 3.1). The valence bands, without Coulomb terms, are indicated by "h" and "l" levels (see the selection rules Fig. 3.2). Both these resonances are then uncoupled if co-circular excitation is considered (Fig. 4.1). We apply our knowledge about a three-level system in order to start the investigation of the Pauli-blocking amplitude 2D-FTS.

Figure 7.1 (d) illustrates the resulting 2D spectra for the Pauli-blocking part (see Eq. (6.15)). We obtain at the diagonal both h and l excitonic peaks, the oscillator strengths of which are given by the corresponding dipole-matrix element and the spectral overlap with the excitation field. The excitation conditions and the parameters such as ratio between dipole-matrix elements and dephasing time of the h and l excitons are fitted to the experiment shown in Fig. 7.1 (a). Since the h binding energy is smaller than the energetic separation between h and l excitons, the l exciton is placed on top of the h continuum. Hence, we have to take the continuum seriously. Another reason for the important role of the continuum is its coupling to the bound excitonic state, which has been experimentally [27] and theoretically [28] verified. Consequently, in order to model the continuum by the one-dimensional tight-binding model we should ideally take an infinite number of sites. In our numerical simulation we have, however, only 40 sites because of computer limitations. This leads to single peaks instead of a continuum in the amplitude spectrum starting from the band edge at an energy slightly below the l excitonic peak. In the 2D-FTS those signatures appear at the diagonal, which confirms that in this limit it is partly represented by an ensemble of uncoupled two-level systems. However, the vertical signatures confirm the coupling of the continuum to the exciton already by the Pauli-nonlinearity.

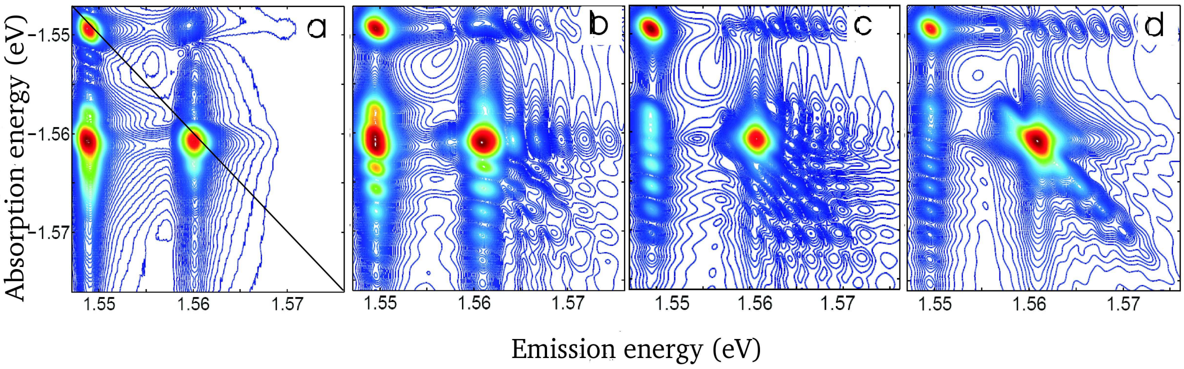

Figure 7.1: Normalized amplitude contributions of 2D-FTS for $\sigma^+\sigma^+\sigma^+$ polarized excitation: (a) experiment. Theoretical inhomogeneously broadened by Gaussian width of 0.7 meV 2D-FTS: (b) full calculation, (c) Hartree-Fock and (d) Pauli-blocking [29]. Here parameter set IV has been used.

In the Hartree-Fock results, Fig. 7.1 (c), the continuum peaks along the diagonal vanish, i.e., the ensemble of uncoupled two-level systems becomes completely inadequate. Due to the fact that for the chosen co-circular polarization the h and l excitonic resonances belong to optically uncoupled subspaces there are no mixed excitonic peaks in off-diagonal positions within Hartree-Fock. At the same time, the coupling of the continuum to the h excitonic state increases due to higher order of the Coulomb interaction. This fact is confirmed by the rise of the non-diagonal continuum signatures at the excitonic emission energies on the non-diagonal. Additionally, the strength of the h peak increases in agreement with the established fact, that the Hartree-Fock results show an increased TI-signal. In principle the l exciton amplitude should also increase, but in contrary the oscillator strength decreases. We explain this fact by an artifact due to the underlying continuum, which inherently consists of single peaks in our simulation. Since the continuum signatures have been smoothed out in the Hartree-Fock results, the l exciton oscillator strength seems to decrease relative to the Pauli-blocking result.

Including many-body correlations, Fig. 7.1 (b), leads to significant changes of the excitonic resonances on the diagonal and the appearance of their mixed contributions at non-diagonal positions. E.g., the mixed excitonic peak at the emission energy corresponding to the h exciton is a pure correlation contribution. The upper non-diagonal peak is suppressed due to small overlap with the excitation pulse spectrum together with the smaller dipole-matrix element of the l exciton. It is also evident that there are strong couplings between the excitons and the continuum due to correlations, as evidenced by the enhanced vertical continuum features. The peak distribution and their line shape show a good agreement with the experiment Fig. 7.1 (a). This demonstrates that this method is able to provide a wide spectrum of information about Coulomb-induced couplings in various systems.

It has been shown that by comparing theoretical spectra resulting from different orders in the Coulomb interaction we can clearly identify the influence of the many-particle interaction on the various signatures that are visible in 2D-FTS.

Chapter 8

Excitation dependence

On the basis of a microscopic theory, the signatures of many-particle correlations in the amplitude 2D-FTS have been identified (see Chapter 7).

In view of the selection rules embedded into the numerical simulations we expect an influence of the polarization direction of the excitation pulses on the signatures of 2D-FTS (Chapter 8.1).

The distribution of the heights of the peaks strongly depends on the interplay of material and experimental parameters, including tuning of the excitation pulses, shape and temporal full-width-at-half-maximum (FWHM) of the pulses (Chapter 8.2), ratio $\frac{\mu^h}{\mu^l}$ of h vs. l dipole-matrix elements (which due to band-mixing in the quantum well structure depart from their bulk values) and dephasing times (see Chapter 4 for details).

8.1 Polarization dependence of the amplitude 2D-FTS

In the following we concentrate on the amplitude features of 2D-FTS in the rephasing mode for the quantum well system considered in Chapter 7. We found that $|\frac{\mu^h}{\mu^l}|^2 = 2.1$ is a good choice for modeling the experiment. The simplest approach to model the h-l-exciton system is a three-level system without any interactions, but with coupling of two excited levels to a common ground state. In this model it is not possible to obtain a peak-height distribution in the 2D-FTS features that is asymmetrical with respect to the diagonal, if the excitation pulses are extremely short and $\mu^h = \mu^l$. The asymmetry of such spectra in our experiments on quantum well systems appears because of the interplay of several effects: different dipole-matrix elements, dephasing times of excitons and biexcitons, degree of overlap with the spectrum of the excitation pulses and many-particle couplings within the system, as supported by the theoretical spectra.

In Figure 8.1 we compare experimental (first column) and theoretical results for the amplitudes from the full calculation (second column) and the Hartree-Fock part (third column) for the co-circular $\sigma^+\sigma^+\sigma^+$, co-linear XXX, and cross-linear YXX polarization direction of the excitation pulses. In all figures the central excitation energy is 1 meV above the l exciton in order to compensate for the small dipole-matrix element of the l exciton.

Numerical results for the full calculation (second column) show agreement with experiments, not only for the h, l exciton and mixed peaks, but also for the h continuum at higher absorption energy ω_τ (the vertical continuum contributions in the experimental data are more apparent in a previous publication [30]). The co-circular excitation case has been discussed in detail in the previous Chapter 7. We now focus on the co-linear situation (Fig. 8.1 middle row). It looks similar to the co-circular case (Fig. 8.1 upper row), as is to be expected from the selection rules. It is remarkable, that the upper right non-diagonal mixed peak for the co-circular case (Fig. 8.1 (b)) has very small oscillator strength. As a comparison with a Hartree-Fock result (Fig. 8.1 (c)) shows, this is not due to correlations, but results from an interplay of detuning, dipole-matrix elements, and dephasing times. The many-body correlations lead to the increase of the mixed signature at higher absorption energy and to vertical features of the continuum as well. Unlike to the co-circular case, the influence of correlations on the mixed signature at higher absorption energy is less pronounced for the co-linear case. The Hartree-Fock approximation (Fig. 8.1

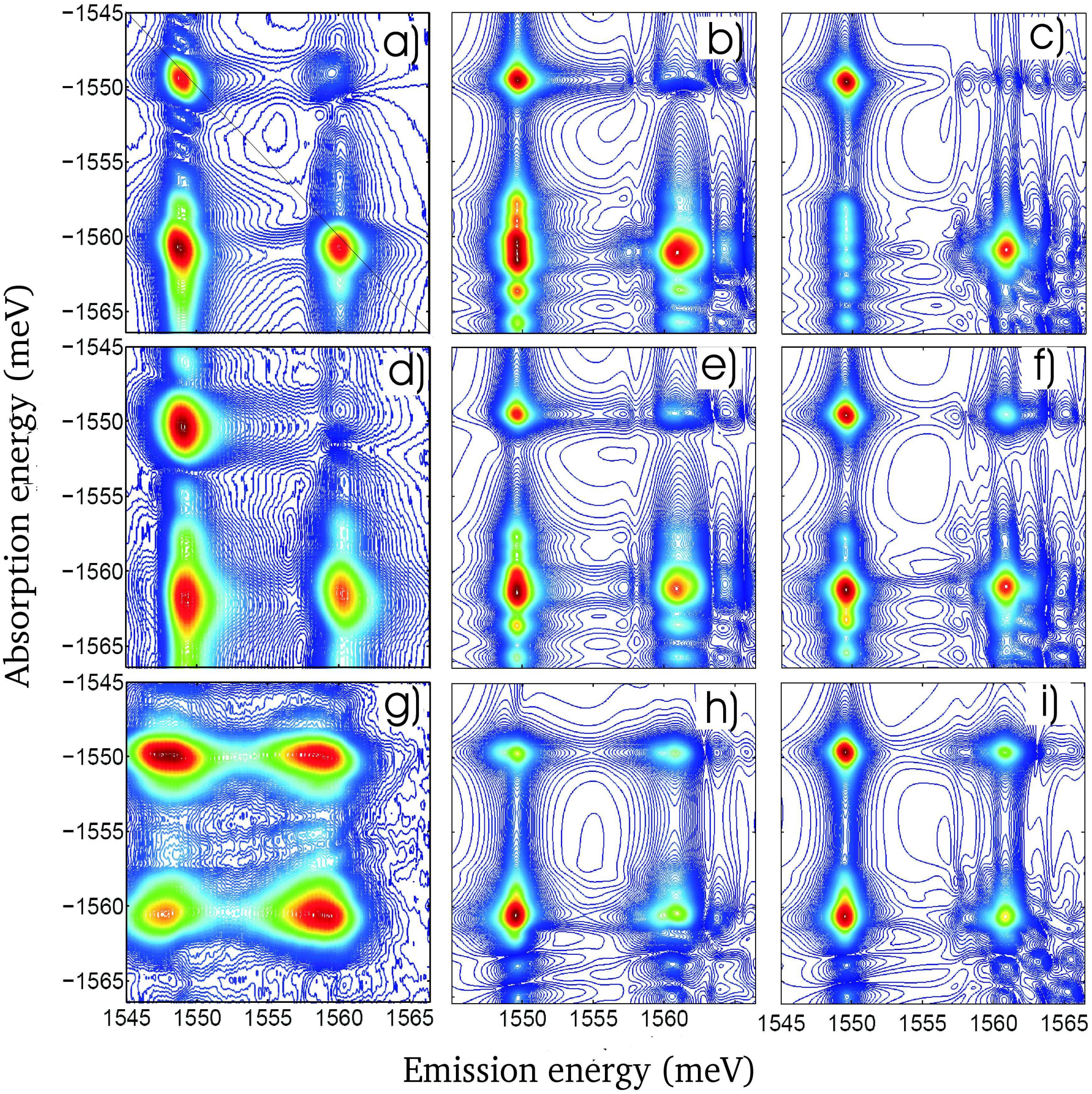

Figure 8.1: Normalized 2D-FTS amplitude spectra. Left column: experimental. Middle column: full $\chi^{(3)}$-calculation. Right column: Hartree-Fock calculation. Upper row: $\sigma^+\sigma^+\sigma^+$ polarization. Middle row: XXX co-linear polarization. Lower row: YXX cross-linear polarization, $T = 350$ fs. Theoretical spectra are weakly inhomogeneously broadened by a Gaussian width of 0.3 meV [8]. Here parameter set IV has been used.

(f)) and the full calculation (Fig. 8.1 (e)) do not differ that much for the co-linear case. This can be understood by consideration of a simple three-level system, where for the excitation $\sigma^+\sigma^+\sigma^+$ the h and l transitions resemble two independent two-level systems. The linear case contains both σ^+ and σ^- transitions, thereby such excitation couples the h and l exciton transitions resulting in two three-level systems (c.f. Chapter 3.2, 4.2). This coupling generates the mixed signatures and appears for both linear polarized cases in the Hartree-Fock calculations (Fig. 8.1 (f): XXX, (i): YXX).

The cross-linear polarized excitation case (YXX) shows additional signatures from two-exciton resonances (bound and unbound biexcitons), as predicted by the selection rules and supported by the theoretical results (Fig. 8.1 (h)). This is due to a suppression of the excitonic features with respect to the biexcitonic ones [22, 23]. Bound biexcitons show up on the low emission-energy side and unbound ones on the high emission-energy side of the exciton [23, 31, 22]. The biexciton contribution results in a horizontal elongation of the peaks compared to the XXX-case. The Hartree-Fock calculation (Fig. 8.1 (i)) clearly shows, that the horizontal elongation of the YXX spectra (Fig. 8.1 (h)) is due to correlations, i.e., bound and unbound two-exciton states. In the Hartree-Fock limit the horizontal elongation is absent (Fig. 8.1 (i)). Interestingly, the continuum contribution and, respectively, the vertical elongation of the signatures at higher excitation energy is less developed as compared to the co-linear case, which is supported by the experiment (Fig. 8.1 (d),(g)). For the cross-linear situation one can show [4, 28] that indeed the continuum becomes suppressed due to cancellation effects that result from Coulomb-correlations in this situation. Indeed, the Hartree-Fock calculation shows a more pronounced continuum contribution (and concomitantly of the superimposed l excitonic peak) in the right-lower corner of the spectrum, as compared to the full $\chi^{(3)}$-calculation.

It is surprising that the lower left non-diagonal peak is the strongest one in the theoretical spectra for the YXX-case (Fig. 8.1 (h)), in contrast to the experimental data (Fig. 8.1 (g)), where the h excitonic peak is the strongest one. At present, the reason for this discrepancy is not clear. The peak in question is a mixture of three contributions, the h and l excitonic resonances and the h continuum. Therefore it is reasonable to assume an effective dephasing of this peak, which is not included in our present treatment. On the other hand, the double structure of the diagonal and non-diagonal peaks is more pronounced in the experiment than in the numerical simulations. In Chapter 12 we demonstrate an essential difference between 2D-FTS and Coherent-Excitation-Spectroscopy methods, which has been used to prove the biexcitonic features. The fundamental difference between both methods is that the biexcitonic features in 2D-FTS are additionally damped (for more details see Chapter 12). That means that the reason for the discrepancies could have a more general basis. Namely, that excitation in the experiment has exceeded the $\chi^{(3)}$-limit. One of the reasons for the increase of the excitation power is the weak signal for the cross-linear polarized excitation pulses. Once we go beyond the $\chi^{(3)}$-limit, the homogeneous broadening of the excitons and biexcitons could be influenced by additional nonlinear terms in the corresponding equations of motion [4]. This also could lead to additional couplings, which should be visible at the non-diagonal. Thus this could be a possible scenario to explain the strong non-diagonal peak and the weak signatures of the biexcitons. Further studies are necessary to substantiate this expectation.

A comparison between the results of the full and the Hartree-Fock calculation shows that the left-lower non-diagonal peak is less prominent in the latter spectra. This difference suggests that correlations enhance this signature in the full treatment. These couplings could well be more sensitive to relaxation processes than the trivial ones which already appear in the three-level system or within a model, which only considers the phase-space (Pauli-blocking) nonlinearities.

We have not studied the dependence of the peak heights on the spectral shape of the incident laser pulses which we have here always taken as Gaussian. Our calculations have shown that the temporal duration and thus the spectral width of the laser beams strongly influences the 2D-FTS. Therefore, deviations of the pulse envelopes from a Gaussian shape will clearly significantly alter the peak heights (see

Chapter 8.2).

The amplitude of the non-diagonal signatures relative to the diagonal ones generally depends on delay time between second and third excitation pulses T. Already for a three-level system one finds that the two non-diagonal peaks show beating with respect to T for the rephasing mode, where the period is $2\pi/\Delta\omega$, with $\hbar\Delta\omega$ the energetic h and l exciton separation (see Fig. 3.1). In the experimental data shown here $T = 350$ fs has been taken. With $\hbar\Delta\omega = 11.5$ meV, corresponding to a beating period of 360 fs, this is close to the situation of maximum non-diagonal peaks. However, as mentioned above, the left-lower signature is definitely too strong if compared to the experiments. In our calculations for the YXX-case we have used $T = 350$ fs as in the experiment.

It should be noted that biexcitonic features can be observed in different kinds of nonlinear optical experiments for certain polarization cases [32, 33, 34, 35, 36]. The 2D-FTS always show the presence of biexcitonic features in the plots for amplitude or real part (not shown here), albeit to different extent, depending on polarization.

A traditional one-dimensional transient FWM (or photon echo) measurement also has trouble yielding T_2 when there are strong many-body correlations, which may result in a rapid decay of the signal which is not related to T_2 [27]. 2D-FTS is much better suited to reveal T_2 of individual resonances. As an example we consider theoretical 2D-FTS-amplitude plots for the cross-linearly polarized pulses, which show the correlation-induced features most prominently. However, now the l transitions have been given the same dephasing time as the h ones, i.e., $T_2^l = T_2^h = 1.3$ ps, while the theoretical results shown in Figure 8.1 correspond to $T_2^h = 1.3$ ps and $T_2^l = 0.8$ ps. Figure 8.2 shows, that the distribution of the peak heights changes due to the longer dephasing time of l exciton. The comparison with Fig. 8.1 (h) demonstrates the large sensitivity of the 2D-spectra on T_2-times.

In summary, it has been shown that the 2D-FTS method provides a wide spectrum of information about the many-body correlations simultaneously, such as:

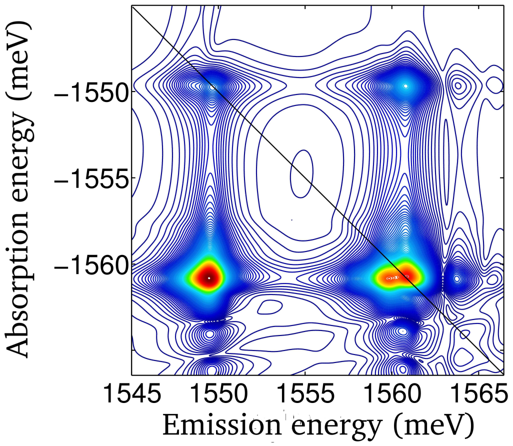

Figure 8.2: Amplitude of 2D-FTS for the YXX case. Here the same parameter set as in Fig 8.1 has been applied, except for the dephasing times, which are: $T_2^l = T_2^h = 1.3$ ps for excitons and $T_2^{ll} = T_2^{hh} = 1.3$ ps, $T_2^{hl} = T_2^{lh} = 0.65$ ps for biexcitons. Theoretical spectra are slightly inhomogeneously broadened by a Gaussian width of 0.3 meV [8].

the strength of the couplings between excitons, biexcitons and continua, character of continuum excitations, dephasing times, and dependences of these features on the polarization directions. Depending on polarization directions of the excitation pulses, characteristic signatures of many-particle correlations can be identified in the amplitude spectra. Differences between experiment and theory point towards the action of relaxation processes on many-particle correlations, which are not included in the present purely coherent treatment in the $\chi^{(3)}$-limit.

In the next chapter we discuss the influence of the overlap between the signatures of 2D-FTS with the excitation pulses on amplitude and real part 2D-FTS for the cross-linear excitation situation.

8.2 Pulse dependence

As it was mentioned in the previous chapter, the peak distribution is strongly dependent on different aspects, including the excitation conditions. In [37] we have demonstrated the experimental and theoretical results for different tunings. The rephasing mode has shown a strong influence of the tuning on the peak distribution and the character of the real-part 2D-FTS in theory and experiment as well. Here, we focus in the following on excitation parameters such as the pulse duration and the pulse form.

In Chapter 4.3 the influence of the tuning frequency on the peaks of 2D-FTS has been investigated for the non-interacting system. In particular, it has been shown, that the rephasing mode is more sensitive to the spectral overlap between the excitation pulse and the peaks. In this chapter we concentrate on the rephasing mode and consider the more interesting case, namely excitation by the cross-linear polarized pulses. It will be interesting to look at the non-diagonal peak at the higher absorption energy and at the form of the peaks: These details have shown some discrepancies with the experiment in the previous chapter.

We start with the consideration of different excitation pulses as shown in Fig. 8.3. The linear spectrum shows the h and l excitons around 15 meV and 27 meV, respectively. The other peaks appear due to the small number of sites, respectively due to the discrete continuum representation. The excitation pulses are centered at the l exciton in order to compensate for its weak oscillator strength. Of particular interest are now the excitation pulses shown in Fig. 8.3. We focus on the amplitude and real-part 2D-FTS for the excitation pulses shown in Fig. 8.3 (a), (b) and (c).

Figure 8.4 illustrates the amplitude (a) and corresponding real-part (d) 2D-FTS for Gaussian pulses with the $\delta_{1,2,3}$=0.1 ps.

The amplitude spectrum for N=40 has been shown in Fig. 8.1 (h). The h excitonic peak in the real-part spectrum Fig. 8.4 (d) shows slightly dispersive character,

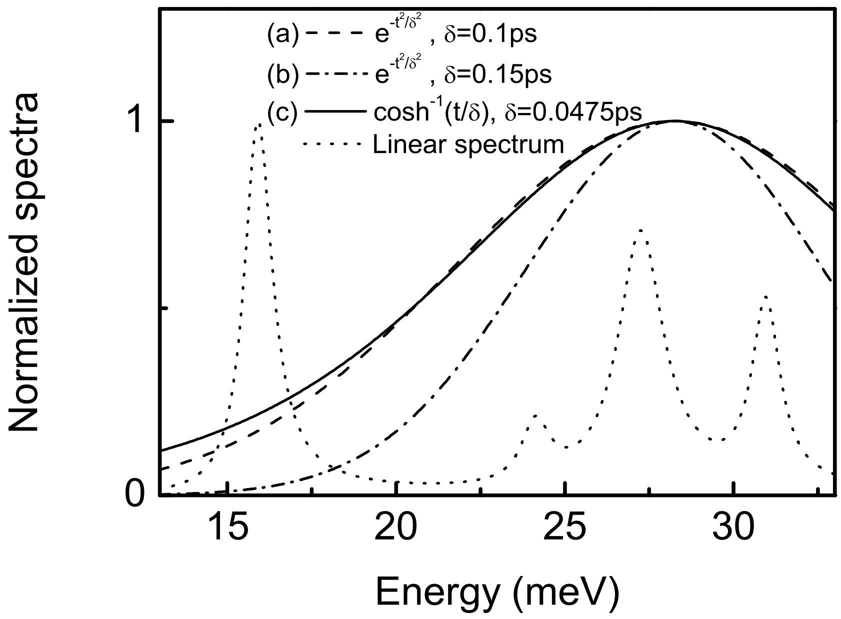

Figure 8.3: The normalized linear spectrum (dotted line) and power spectra of the excitation Gaussian pulses with $\delta_{1,2,3}$=0.1 ps (a), $\delta_{1,2,3}$=0.15 ps (b) and $1/cosh(t/\delta)$, where $\delta_{1,2,3}$=0.0475 ps (c). The parameter set V for (a) has been used, for (b) and (c) as well, except for $\delta_{1,2,3}$.

the horizontal elongation of the negative part is due to bound biexcitons. The l excitonic peak at the higher absorption energy on the diagonal has mostly absorptive character, which could have several reasons. The fact that the l excitonic peak is placed on top of the continuum could change the character of the line shape of l exciton. As a consequence the second reason follows, namely the insufficient representation of the continuum. Thus it is clear that for the comparison with the experiment (as it has been done in Fig. 8.1 (h)) and the detailed analysis of the single peaks and their distribution, a much larger number of sites is required.

In our particular case we are interested in the effect of the spectral overlap between the excitation pulses and the peaks. For this reason we compare Fig. 8.4 (a) and (b), which correspond to FWHM of the power spectrum of about 15.5 meV

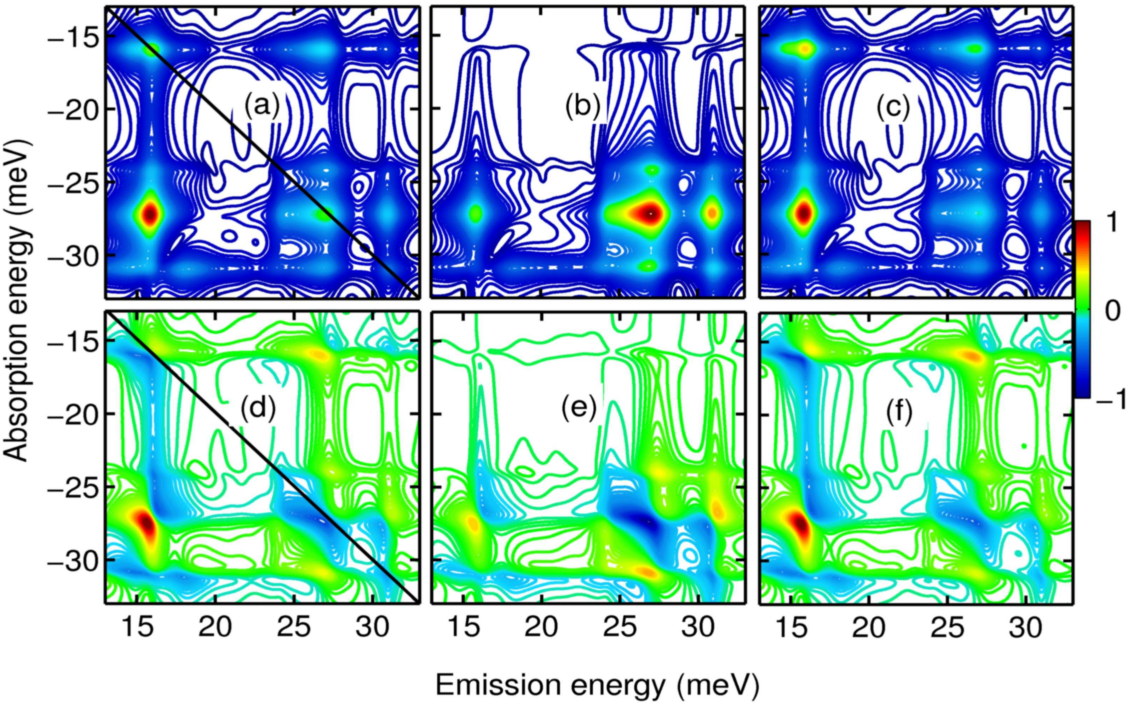

Figure 8.4: Normalized amplitude (upper row) and real-part (lower row) 2D-FTS calculated for cross-linear polarized excitation pulses. Gaussian pulses with $\delta_{1,2,3}$=0.1 ps (a) and (b) $\delta_{1,2,3}$=0.15 ps are taken. In (c) excitation pulses given by $1/cosh(t/\delta)$ with $\delta_{1,2,3}$=0.0475 ps are considered. The parameter set V has been used.

and 10.3 meV, respectively. Since the overlap of the pulses with the peaks is reduced in Fig. 8.4 (b) and the pulses are centered at the l exciton, the oscillator strength of the h excitonic peak decreases. As a result we obtain a strong l excitonic peak and weak non-diagonal peaks, which indicate the couplings between the l and the h exciton. At the same time, the coupling to nearest-neighbor continuum peaks is becoming more pronounced. The real-part 2D-FTS for both excitation cases shown in Fig. 8.4 (d) and (e) in general do not differ that much. The peak distribution has been changed due to different overlap with the excitation pulses and the character of the line shape is kept the same. Thus we see that the influence of the excitation on the peaks is predictable.

It is interesting to consider the special case where the excitation pulses do not have Gaussian form, but are given by the following function: $1/cosh(t/\delta)$, a so-called sech-pulse (secans hyperbolicus). Figure 8.3 (c) shows the power spectrum of the pulse given by this function. We have chosen a certain δ for this pulse in order to obtain the same FWHM as in Figure 8.3 (a). We compare the amplitude 2D-FTS given in Fig. 8.4 (a) and (c). As a consequence of the long “tails” of the sech-excitation pulse, the overlap with the peaks increases, in particular with the h exciton. This leads to a rise of the oscillator strength of the h excitonic peak and concomitantly to a rise of the non-diagonal peaks. Hence the peak distribution is slightly changed. The oscillator strength of the non-diagonal peak at the lower absorption energy is bigger than the oscillator strength of the diagonal l excitonic peak. It is remarkable, that the horizontal elongation due to biexcitons is more pronounced, which is in agreement with the experiment shown in Fig. 8.1 (g). The real-part 2D-FTS in Fig. 8.4 (d) and (f) confirm the fact that the biexcitonic features are more pronounced for the excitation with sech-pulses. The line shape of the peaks, however, is kept the same.

In conclusion, we have investigated the influence of the spectral overlap between the excitation pulses and the signatures of the amplitude and the real-part 2D-FTS of the rephasing mode. We found, that a variation of 30% of the spectral overlap leads to a drastic change of the peak distribution. Though, the line shape of the peaks in real 2D-FTS has not been influenced. The amplitude 2D-FTS indicate even slight changes of the form of the excitation pulse.

8.3 Conclusions

In this chapter the influence of the different excitation conditions on 2D-FTS was of particular interest. It has been shown that the two-dimensional spectra contain information about the material parameters of the considered system and the excitation condition as well. This information can be extracted by proper modeling of the excitation conditions such as tuning, polarization of the excitation pulses, their form and duration, as well as by choosing suitable material parameters. In the specific case of narrow quantum wells, where the l exciton might be placed on top of the continuum, good continuum representation is needed.

It was furthermore shown that the non-diagonal peak at higher absorption energy is not influenced by the form of the excitation pulses.

Chapter 9

Determination of the overall constant phase

In this chapter we address the uncertainty which can exist in the experimental data due to insufficient knowledge of the overall constant phase. This phase can possibly be extracted from comparing calculated real- and imaginary-part 2D-FTS. The measurement in the optical regime of the phase between excitation pulses and the signal in 2D-FTS experiments is more complex than for the IR regime due to fluctuations in the path length and beam direction [3]. Additional complexities exist in the experiment, when the pulses are cross-linearly polarized [38]. This leads to a lager error by the determination of an overall constant phase, called here the global phase. In the following we consider theoretical results for arbitrary global phase and compare them with the experimental real- and imaginary-part spectra for the rephasing mode.

Figure 9.1 illustrates the real-part (upper row) and imaginary-part (lower row) 2D-FTS for different choices of the global phase.

It is clear, that the real-part spectrum for the global phase equal to zero is the same as the imaginary part for the global phase equal 90° (see Fig. 9.1 (a) and (f)). The character of all peaks is strongly influenced by the global phase. E.g., the h excitonic peak changes its character from dispersive for the global phase 0° Fig. 9.1 (a) to absorptive character for the 90° (c). A dispersive line yields generally

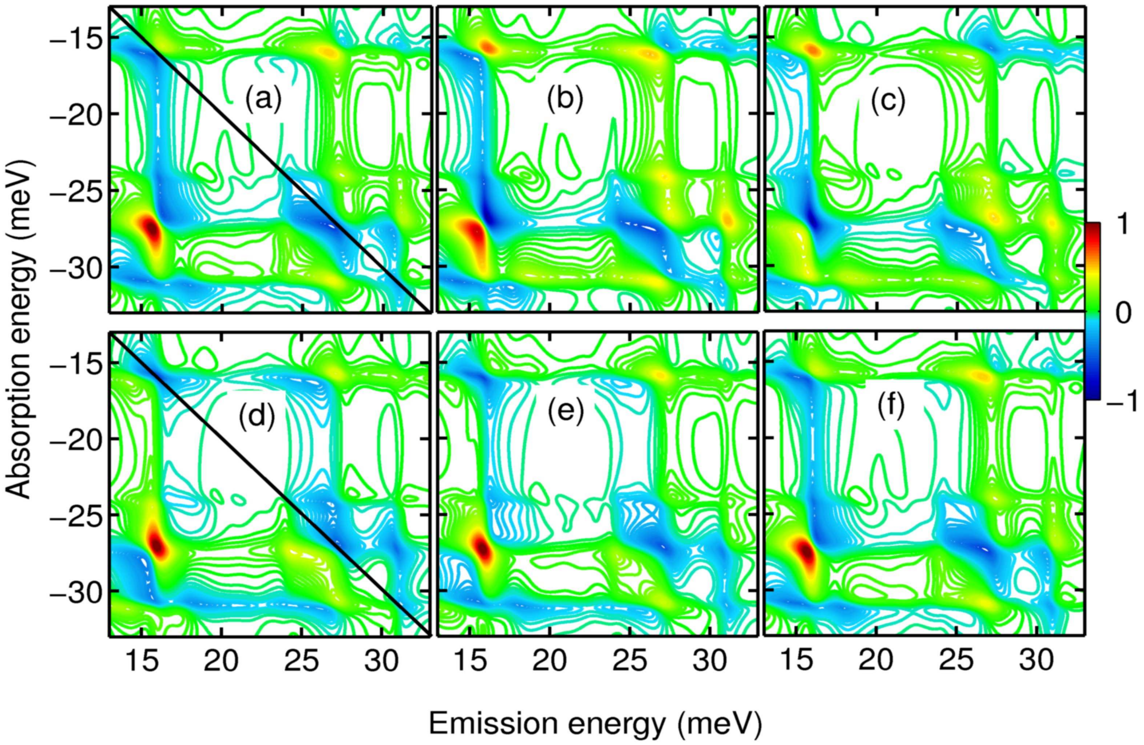

Figure 9.1: Normalized real-part (upper row) and imaginary-part (lower row) 2D-FTS for the cross-linear excitation situation, rephasing mode. The global phases are equal to 0° ((a) and (d)), 45° ((b) and (e)) and 90° ((c) and (f)). The parameter set V has been used.

more detailed information. The horizontal elongation in the amplitude 2D-FTS, which has been identified as the bound biexciton, shows up in the negative part of the dispersive excitonic peak (Fig. 9.1 (a), (b) and (f)). That means, that the non-linear features, such as biexcitons, can no longer be identified in the real-part 2D-FTS for the global phase equal 90° (Fig. 9.1 (c)), but in the imaginary part (Fig. 9.1 (f))! The same situation is valid for the imaginary part, Fig. 9.1 (d), which corresponds to global phase equal to zero. Thus the real- and imaginary-part 2D-FTS yield additional information about the global phase and calls for a precise comparison between experiment and theory. Such a comparison has been done for the sample given in Ref. [8]. The real- and imaginary-part 2D-FTS for the co-circular and co-linear excitation cases have shown a very good agreement with the experiment (not shown here) [37]. More interesting is the cross-linear situation.

In Fig. 9.2 the results of the numerical simulation (first column) and the measured (second column) real- and imaginary-part 2D-FTS are depicted.

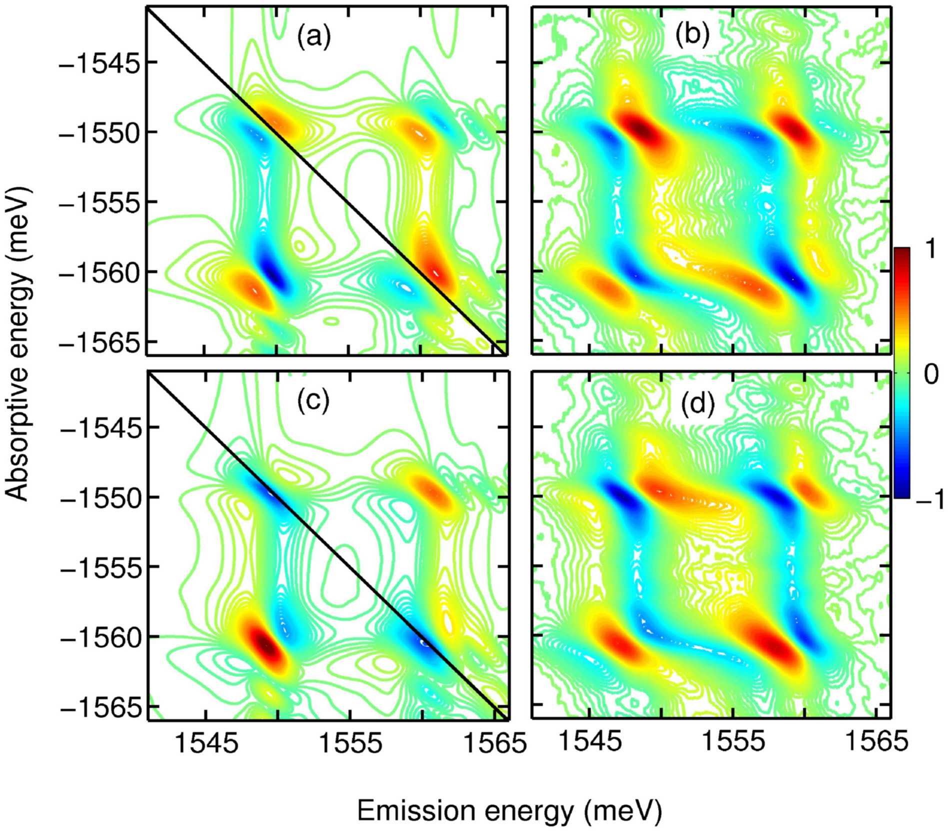

Figure 9.2: Normalized real- (upper row) and imaginary-part (lower row) 2D-FTS for the cross-linear excitation situation, rephasing mode. The global phase is 45° ((a) and (c)). (b) and (d) represent the experimental data measured by T. Zhang. The parameter set IV for T=350 fs has been used.

The theoretical results have been inhomogeneously broadened by a Gaussian function with δ=1 meV. This leads to a slight change of the spectra due to elongation along the diagonal. Since we are comparing the calculated spectra with the experiment, 40 sites have been taken in the numerical simulations. The h exciton in the real-part 2D-FTS shows dispersive character, which is in agreement with the experiment (Fig. 9.2 (a) and (b)). The l exciton diagonal peak shows nearly dispersive character, but differs from the experiment. The reason for that could be an insufficient representation of the continuum. Thus the single resonances of the continuum in the calculations add to the l excitonic peak and change its character. Furthermore, the total peak distribution has not been fitted to the experiment. This leads to a different distribution of the oscillator strengths, in particular also to different weights of the positive and negative parts for each single resonance. This is in particular important for the non-diagonal peaks, which indicate the coupling between the excitons. Most discrepancies are recognizable at the non-diagonal within the central square which is surrounded by the four dominant peaks. These observations are also true for the imaginary-part 2D-FTS (Fig. 9.2 (c) and (d)). Good agreement is achieved for the h excitonic peak and the non-diagonal peak at the higher absorption energy. It has to be noted, that the real- and imaginary-part 2D-FTS in the experiment and numerical simulations as well, in this particular case look similar.

In spite of certain discrepancies, which can have their origin also in additional physical mechanisms such as an additional or more complex dephasing processes, which have not been included in the theory, or in higher order of the excitation in the experiment, it was, possible, by comparing the real- and imaginary-part theoretical 2D-FTS with the experimental data to find the global phase of 45°. This seems to be the appropriate choice for these particular measurements.

The phase information contained in the real- and imaginary-part spectra will be shown to yield additional information about the material parameters of the sample. This will be discussed in Chapter 11.

Chapter 10

Band structure effects

In our first paper on the comparison between experiment and theory for 2D-FTS [8], we have made a presumption that one of the reasons for the discrepancy between experiment and theory for the cross-linear excitation situation is a band-mixing effect, which has not been modeled in this work. The aim of this chapter is to investigate such band-mixing effects and to prove the presumption.

10.1 Intra-site heavy-light hole coupling

In this chapter we investigate the effects on 2D-FTS caused by the valence-band structure. For this reason we amend the one-dimensional tight-binding model further more by including an additional coupling between heavy- and light-hole bands J^{hl}. In our extended model (see Fig. 10.1), we take only the dominant intra-site heavy-light hole coupling.

We modify our hermitian matrix given in Chapter 3.1 by including additional coupling J^{hl} as follows:

$$\begin{pmatrix}
\epsilon_1^e & 0 & 0 & J^e & 0 & 0 & \dots & J^e & 0 & 0 \\
0 & \epsilon_1^h & J^{hl} & 0 & J^h & 0 & \dots & 0 & J^h & 0 \\
0 & J^{hl} & \epsilon_1^l & 0 & 0 & J^l & \dots & 0 & 0 & J^l \\
\vdots & & & & & & & & & \vdots \\
J^e & 0 & 0 & 0 & 0 & 0 & \dots & \epsilon_N^e & 0 & 0 \\
0 & J^h & 0 & 0 & 0 & 0 & \dots & 0 & \epsilon_N^h & J^{hl} \\
0 & 0 & J^l & 0 & 0 & 0 & \dots & 0 & J^{hl} & \epsilon_N^l
\end{pmatrix}$$

Now, since the analytical calculation seems no more possible, we rely on a numerical

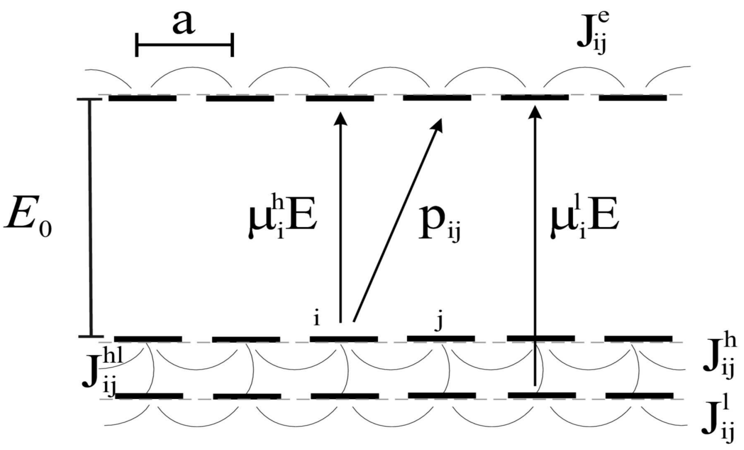

Figure 10.1: Extend one-dimensional tight-binding model. J^{hl} is h-l coupling parameter. For further details see Fig. 3.1.

diagonalization of the matrix. In order to find the eigenstates numbered by n with corresponding k_n-values we use the same procedure as it was described in Chapter 3.1. As a result we obtain the band structure, which differs from the previous cosine-like one (Eq. (3.3)).

In the following we focus on the comparison of the band structure, calculated by the one-dimensional tight-binding model without (Fig. 10.2, left) and with (Fig. 10.2, right) intra-site heavy-light hole coupling (valence band mixing effects). In both cases the offset between h and l is kept the same.

By including valence-band mixing effects changes in the linear spectra, hence also in the amplitude 2D-FTS, are expected. That means that the spectral overlap of the peaks of 2D-FTS with the excitation pulse will be different. Consequently such 2D-FTS spectra are not comparable. However, as we are here interested in pure valence-band mixing effects, we compensate the changes due to above mentioned effects in the linear spectra by changing parameters such as the heavy-light hole offset ($\hbar\Delta\omega$), the dipole-matrix element and the Coulomb strength. For simplification we begin with the discussion of the co-circular case.

Figure 10.3 shows the linear spectrum (a), the 2D-FTS for the Pauli-blocking

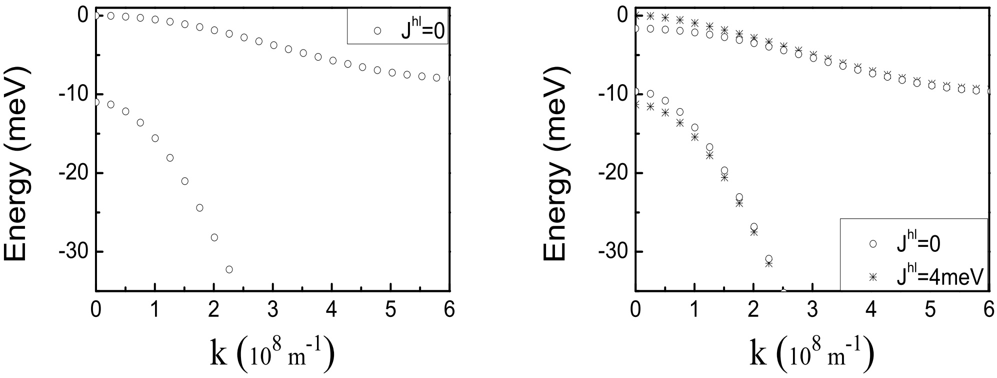

Figure 10.2: Band structure calculated using the one-dimensional tight-binding model. Left: without including intra-site heavy-light hole coupling ($J^{hl} = 0$ meV), right: with ($J^{hl} = 4$ meV, stars) and without ($J^{hl} = 0$ meV, circles) valence band mixing effects.

case (b) and full the calculation (c) for the situation without band mixing effects. The Pauli-blocking calculation (Fig. 10.3 (b)) is expected to yield approximately the

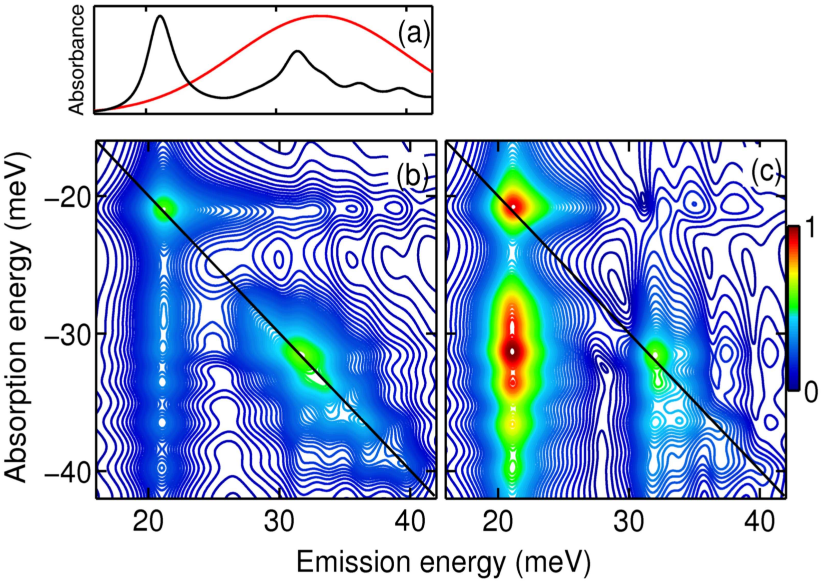

Figure 10.3: Linear spectrum (a), amplitude 2D-FTS for the co-circular excitation case without valence-band mixing effects ($J^{hl} = 0$ meV) for Pauli-blocking (b) and full calculation (c). Here parameter set VI has been used. The corresponding valence-band structure is given in Fig. 10.2, left.

same results as for the three-level system (see Chapter 4.1). Here, by including the Coulomb term in the electron-hole attraction terms only, we obtain weak vertical and horizontal elongated signatures of continua at the non-diagonal positions[1]. The full calculation illustrates an increase of the h exciton and the appearance of non-diagonal peaks due to correlations (Fig. 10.3 (c)).

Figure 10.4 demonstrates the amplitude 2D-FTS for the band structure given in Fig. 10.2 (case $J^{hl} = 4$ meV). Since the changes of the band structure are small, we

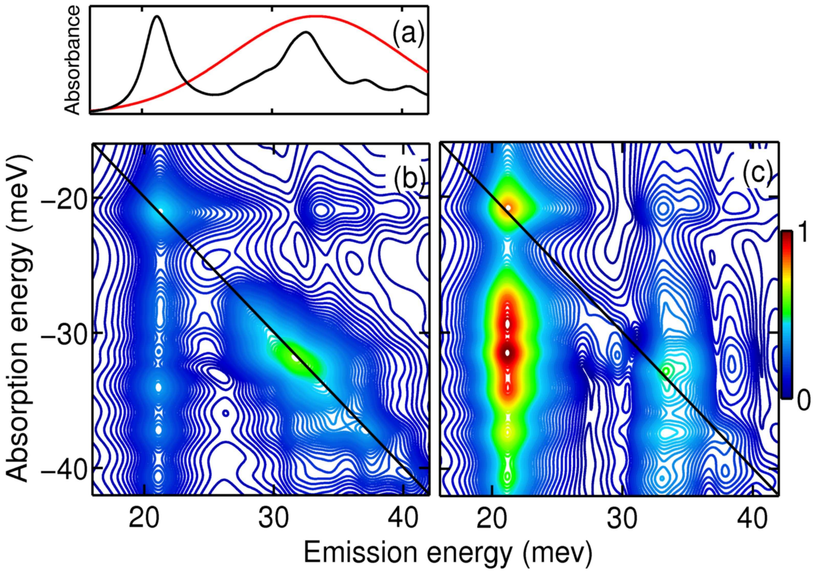

Figure 10.4: Linear spectrum (a). Amplitude 2D-FTS for the co-circular excitation case with valence-band-mixing effects ($J^{hl} = 4$ meV) for Pauli-blocking (b) and full calculation (c). Here parameter set VII has been used. The corresponding valence band structure is given in Fig. 10.2, right.

would not expect a significant changing of the amplitude spectra. We compare the Pauli-blocking result for the case without (Fig. 10.3 (b)) and with (Fig. 10.4 (b)) band-mixing effect. The intra-site heavy-light hole coupling leads to the appearance of non-diagonal peaks at the absorption and emission energy of the second (higher-energy) exciton, which has a weak strength due to weak coupling. The full calcu-

---

[1] The discrete character of continua signatures illustrated in Fig. 10.3 is due to finite number of continua states in our numerical calculations.

lation given in Fig. 10.3 (c) shows, by including additional coupling (Fig. 10.4 (c)), a decrease of the oscillator strength of the diagonal peaks, so an increase of the non-diagonal peaks. Thus, as it has been expected, an additional weak coupling J^{hl} shows up slightly at the non-diagonal sectors, which depict such couplings as exciton-exciton and exciton-continuum couplings.

A more interesting situation is the case of crossing valence bands. Figure 10.5 demonstrates such a band structures.

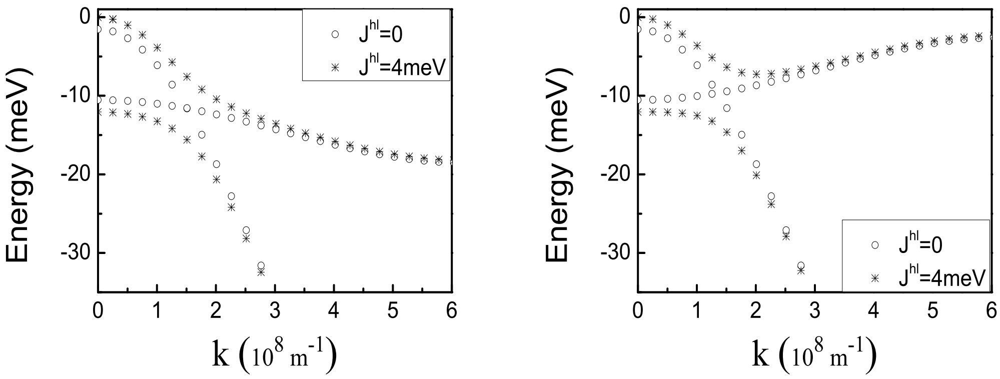

Figure 10.5: Band structures calculated using the one-dimensional tight-binding model without ($J^{hl} = 0$ meV, circles) and with ($J^{hl} = 4$ meV, stars) including intra-site heavy-light hole coupling. Left: upper band is monotonous. Right: upper band has a minimum.

In our numerical simulation of the initial (before crossing) band structure the parameters such as the effective masses are taken to be the same, however, we change its sign for the lower, h valence band (Fig. 10.5, left vs. right). Such preparations are necessary in order to extract the changes of the 2D-FTS caused by pure band-mixing effects.

We begin with the situation corresponding to the band structure given in Fig. 10.5, left. Differently to Fig. 10.2, the upper valence band has a smaller effective mass at the wave vector close to zero. Even though the linear spectrum for the case with and without coupling J^{hl} has been adjusted for a model having 10 sites, the offset between h and l excitons increases by taking more sites, which leads to different linear spectra for both cases (Fig. 10.6 (a) and Fig. 10.3 (a)). Hence, the comparison of amplitude 2D-FTS without (Fig. 10.3) and with (Fig. 10.6) pure band-mixing effects is not equitable.

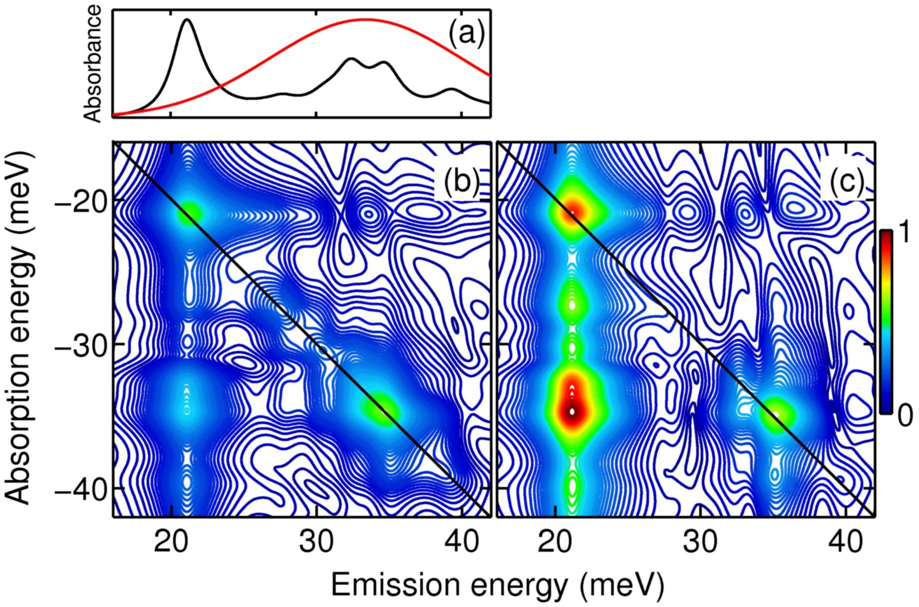

Figure 10.6: Linear spectrum (a). Amplitude 2D-FTS for the co-circular excitation case with valence-band mixing effects ($J^{hl} = 4$ meV) for Pauli-blocking (b) and full calculation (c), corresponding to the valence-band structure given in Fig. 10.5 on the left hand side. Here parameter set VIII has been used.

Here the difficulties and the numerical effort involved in such a comparison of 2D-FTS have to be mentioned. The first complication is the definition of the ratio between the matrix elements of the h and l excitons. This ratio is very important, because of its strong influence on the distribution of the oscillator strengths of the peaks. Since we model the continuum by a finite number of the states, it might happen that the excitonic state falls exactly on top of a single continuum state, which would lead to a virtual increase of its oscillator strength in the linear spectrum. That means, even for similar linear spectra, the ratio of the dipole-matrix elements in our particular case, where the h exciton is sitting in the continuum, might be somewhat inaccurate. The problem of the correct ratio of the dipole-matrix elements could only be solved by taking an infinite number of sites.

Another important point, which is also connected to the number of sites, is the resolution of the wave function. The spectra for our particular case show a convergence for the number of sites larger than 48. Figure 10.7 demonstrates, that by changing the number of sites from 40 (Fig. 10.6 (c)) to 48 (Fig. 10.7) the exciton at the higher[2] absorption energy is shifted, thereby the offset is reduced by 1.75 meV. This allows us to compare the amplitude spectrum (Fig. 10.3 (c)) with (Fig. 10.7) and extract the band-mixing effects for the case given in Fig. 10.5, left. At the non-diagonal sector, the vertical signatures of the continua show significant differences. The diagonal peaks do not show such differences and the peak distribution remains the same. That means that the intra-site heavy-light hole coupling has no significant influence on excitonic peaks, but it modifies the continuum signatures of 2D-FTS at least for the excitation case with co-circular polarized pulses.

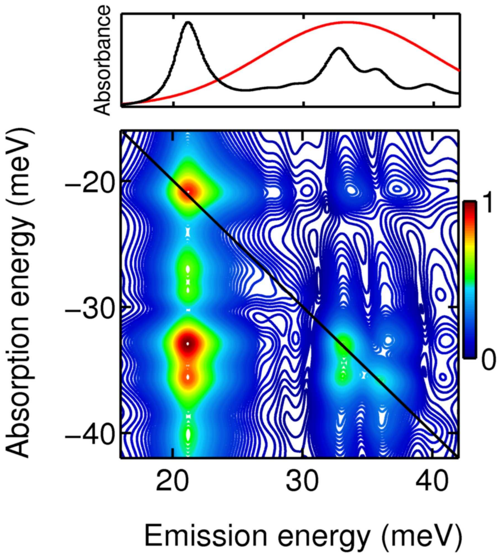

Figure 10.7: Amplitude 2D-FTS for the co-circular excitation case with valence-band mixing effects ($J^{hl} = 4$ meV), correspond to the valence band structure given in Fig. 10.5 on the left hand side. Here parameter set VIII with number of sites 48 has been used.

---

[2] Here, this means the absolute value of the energy.

We now focus on the special case, where the lower band has a positive curvature (Fig. 10.5 right), but the absolute value of the effective mass is taken to be the same. Such positive curvature of the valence band has been found from $k \cdot p$ calculations, for a example, for the quantum-well structure considered in Ref.[8]: 10 nm GaAs QW with AlGaAs barriers. We compare amplitude 2D-FTS for the band structure shown on the left-hand Figure 10.5 and on the right-hand one. We begin with the Pauli-blocking spectra shown in Fig. 10.6 (b) and Fig. 10.8 (b). The differences of those spectra are negligible, which could be explained by very similar linear spectra shown in (a) of Figs. 10.6 and 10.8. It is interesting that such drastic changes in the valence band are not appearing in the Pauli-blocking calculations. By including terms in higher order in the Coulomb interaction the spectra do exhibit changes due to band-mixing effects (Figs. 10.6 (c) and 10.8 (c)). On hand of the linear spectra we would expect that the higher diagonal peak is stronger than the lower one. The amplitude spectra for both band-curvature cases prove this, however, the

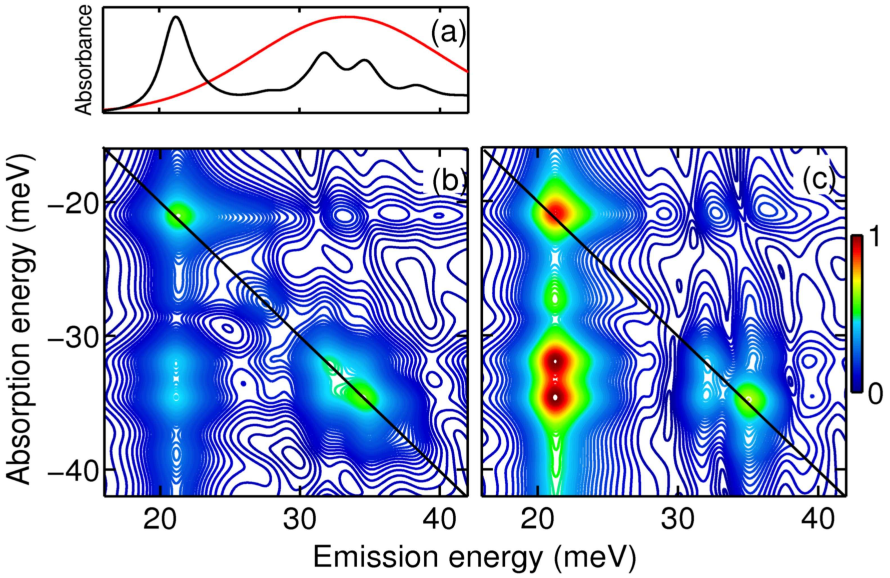

Figure 10.8: Linear spectrum (a). Amplitude 2D-FTS for the co-circular excitation case with valence-band mixing effects ($J^{hl} = 4$ meV) for Pauli-blocking (b) and full calculation (c), corresponding to the valence-band structure given in Fig. 10.5 on the right-hand side. Here parameter set IX has been used.

ratio between the oscillator strength of the diagonal peaks is slightly different. In fact, for a simple three-level model, the oscillator strength of the non-diagonal peaks is given by the product of the matrix elements of the diagonal peaks, it causes their (non-diagonal peaks) differences of the amplitude spectra. Additionally, in Fig. 10.8 (c) the lower diagonal peak has a more pronounced double structure. The question is: What is the reason for the double structure of that peak?

In order to understand this result, we use the scheme of the band structure with optical transitions shown by vertical lines (Fig. 10.9). It is well known that the excitonic peaks are built from optical transitions for wave vectors close to zero. In our case we would expect two kinds of optical transitions: from the upper and lower bands. Since the lower band has a positive curvature, the band-mixing effects lead to additional band minima at the crossing point (at k=1.5 10^8 m^{-1}, see Fig. 10.5, right). The band minima lead to a rise of the density of states, which is just at the energy between the energies of l and h excitons. Obviously, the additional signature in the amplitude 2D-FTS (Fig. 10.8 (c)) is an artifact of our model. The positive curvature of the h valence band in our model is taken for the whole Brillouin zone, which is not realistic. However, by using 2D-FTS we can identify the artifacts of the model, but also can state that weak intra-site heavy-light hole coupling has only slight influence on the nonlinear spectra.

In conclusion, we have investigated the band-structure effects on 2D-FTS for the co-circular excitation situation. We found that, by including only the intra-site heavy-light hole coupling for the co-circular excitation case, this has no significant influence on the amplitude 2D-FTS. This result could probably be due to the chosen weak coupling strength. It has been demonstrated that an artifact of the model can be identified by the amplitude 2D-FTS.

The motivation at the beginning of this chapter was to find strong band-mixing effects for the cross-linear excitation case. Since such excitations lead to a suppression of the single excitonic peak (as opposed to biexcitonic peaks), we can expect that

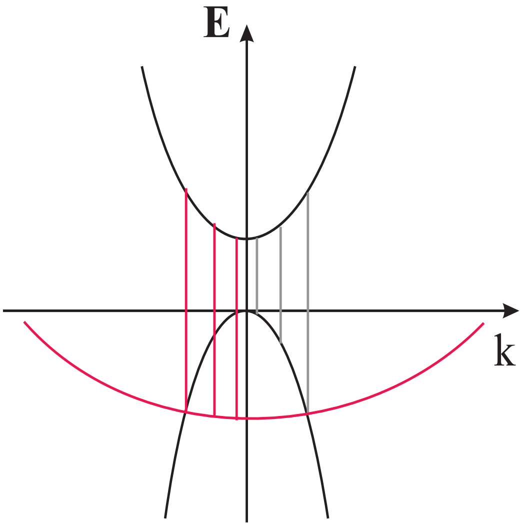

Figure 10.9: Schema of the band structure, where h valence band (red) has a positive curvature. Thus by band mixing the additional optical transition at the crossing point will be lifted up.

additional couplings would also contribute to the suppression of the non-diagonal peaks at the energies corresponding to single excitonic states.

We begin with the situation for the band structure given in Fig. 10.2, left. The linear and the amplitude spectra for the cross-linear excitation case are shown in Fig. 10.10 (a). The linear spectrum (a) displays the relative to (b) and (c) strong second excitonic peak. Thus we expect two comparable excitonic peaks at the diagonal and at the non-diagonal of the amplitude spectra, respectively. This is in agreement with the results of the amplitude 2D-FTS shown in Fig. 10.10 (a). Generally, the continuum signatures for the cross-linear excitation case are expected to be suppressed. Figure 10.10 (a) illustrates such a suppression of continuum signatures at the higher[3] absorption energy. In case of band mixing, corresponding to Fig. 10.5, left, 2D-FTS given in Fig. 10.10 (b) shows strong continua suppression also at the lower absorption energy. The peak distribution of 2D-FTS differs from that for the case without band-mixing effects (Fig. 10.10 (a)) due to different linear spectra. The oscillator strength of the non-diagonal peak is not decreasing when

---

[3] Here, this means the absolute value of the energy.

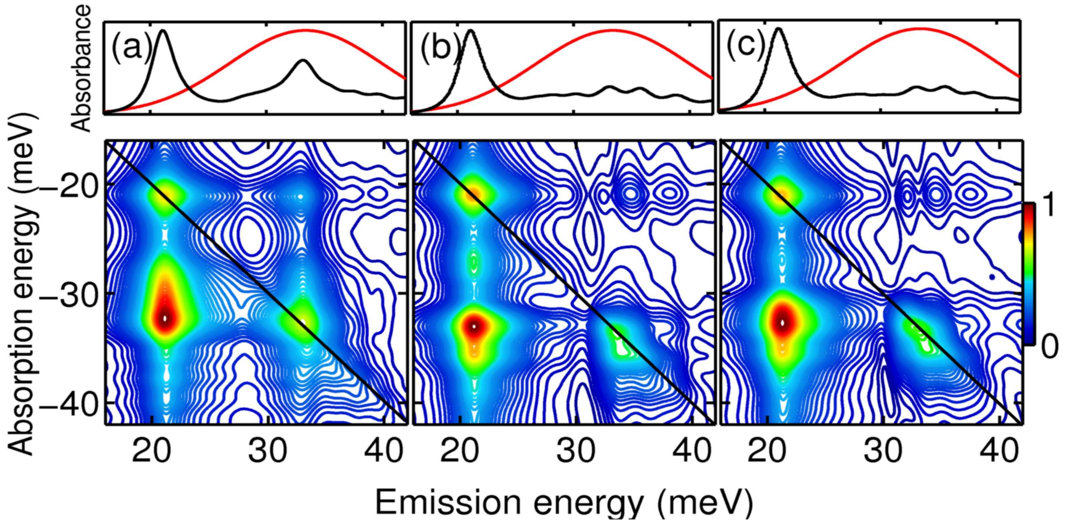

Figure 10.10: Amplitude 2D-FTS for the cross-linear excitation case without (corresponding to the valence-band structure given in Fig. 10.2, left) (a) and with valence band-mixing effects (b) and (c), which correspond to the valence-band structure given in Fig. 10.5, left and right, respectively. Here parameter set X for (a), VIII for (b), and IX for (c) with number of sites N =58 have been used.

the intra-site heavy-light hole coupling is included. Therefore, the presumption that only this type of coupling could reduce the oscillator strength of the non-diagonal peak could not be substantiated. A scenario with positive band curvature does not solve the problem with the strong non-diagonal peak either. Figure 10.10 (c) demonstrates a very similar linear spectrum like case (b) for the negative band curvature, which gives a more accurate estimate of the extraction of the band-mixing effects by comparison of 2D-FTS. Here we observe a slight elongation of the non-diagonal peak at higher absorption energy. The peak distribution remains similar to the previous case.

In conclusion, we have investigated the band mixing-effects in order to find a reason why the non-diagonal peak at higher absorption energy has such big oscillator strength in our model if compared to experimental findings for the cross-linear excitation case. It is obvious that by including only the intra-site heavy-light hole coupling, the reduction of the oscillator strength of this peak can not be achieved.

This was proved for both the co-circular and cross-linear cases.

In the next chapter we consider the cross-linear excitation situation and we investigate the influence of the material parameters such as the effective masses on 2D-FTS.

10.2 Biexcitonic features

It is well known that FWM experiments for the cross-linear excitation situation provide evidence for biexcitonic signatures. This has been demonstrated also for 2D-FTS and compared with the experiment for the rephasing mode [8].

In the previous chapter we considered the amplitude 2D-FTS for the cross-linear excitation case. However, biexcitonic signatures actually did not show up.

The motivation for this chapter is to answer the question why the biexcitonic signatures were not visible in Fig. 10.10. Furthermore, the presumption about the dependence of the amplitude 2D-FTS on the effective masses will be substantiated.

We begin with the comparison of the amplitude 2D-FTS for electron-coupling parameters J^e=6 meV as well as 22 meV. The last value corresponds, together with the chosen lattice constant a, to the effective mass of the electron for the bulk within our present one-dimensional tight-binding model. Figure 10.11 (a) and (b) illustrate amplitude 2D-FTS for the electron-coupling parameters 6 meV and 22 meV for the case with finite inter-site heavy-light hole coupling.

In Appendix B we calculate the effective masses on the basis of the parameters, which we use in the one-dimensional tight-binding model (Fig. 3.1). Changing of the electron-coupling parameter J^e leads to a change of the reduced mass of the h and l excitons. Since our valence bands are coupled we can only approximately estimate the influence on the values of the effective hole, and thus reduced exciton, masses. The reduced mass of the h exciton m_r^h is proportional to 0.125 and for the l exciton $m_r^l \propto$ 0.07 in the case presented in Fig. 10.11 (a) and, respectively, for the parameter chosen in Fig. 10.11 (b): $m_r^h \propto$ 0.04 and $m_r^l \propto$ 0.033. In fact the exciton binding

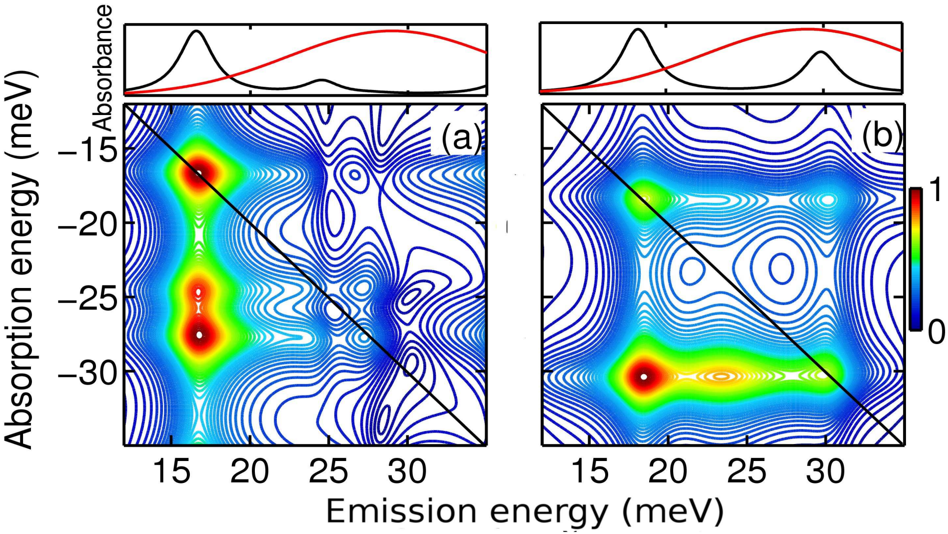

Figure 10.11: Amplitude 2D-FTS for the cross-linear excitation case including intra-site heavy-light hole coupling without crossing of the valence bands. For the electron-coupling parameter J^e=6 meV (a) and 22 meV (b) has been applied. Here parameter set XI (in case (b) J^e has been taken equal 22 meV) has been used.

energy is propotional to its reduced mass, thus the reduction of the effective mass provokes a reduction of the exciton binding energy. That means that the excitonic state approaches the continuum states (cp. Fig. 10.12 (a) and (b)).

If Fig. 10.11 (a) is compared with Fig. 10.11 (b) one sees an additional feature at emission energies above the lower lying exciton. The amplitudes 2D-FTS in Fig. 10.11 show that by increasing the electron-coupling parameter J^e a horizontal double structure of the peaks appears. It will be shown below that this feature is exclusively due to correlations. This gives evidence for the fact that by moving the excitonic resonance towards the continuum the structures due to correlations (here unbound biexcitonic states) are pushed away from the exciton. It has been shown previously [28] that for the cross-linear excitation situation the continuum states are strongly determined by correlations. Therefore it seems plausible that there could be repulsion between continuum states and unbound biexcitonic states if these spectral features approach each other. If this reasoning is correct, then the signatures in Fig. 10.11 (b) should be identified as a signature of the biexcitons. Of

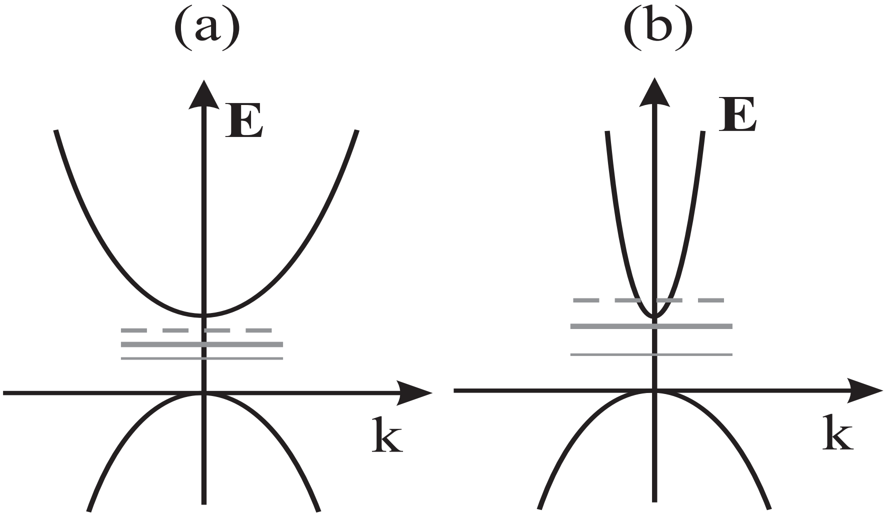

Figure 10.12: Scheme of the band structure for the electron-coupling parameter J^e (a), which is smaller than J^e in (b). Thick solid gray line depicts a single excitonic resonance, the thin gray line is a bound biexcitonic state and the dashed gray line is an unbound biexcitonic state.

course, more calculations are necessary to prove this interesting interpretation in detail.

It should also be noted that the first excitonic peak shifts due to changing the J^e parameter. As a consequence of this shift of the exciton the overlap with the excitation pulses and thus the peak distribution has been changed. Since here we are not interested in studying the distribution of the peak strengths, we only qualitatively estimate the change of the amplitude spectra due to the change of the J^e parameter, i.e, the effective electron (reduced exciton) mass. The general feature of 2D-FTS is the appearance of the horizontal elongation when the effective mass is changed. This could not be induced by the different overlap with the excitation pulse.

We now show that the feature shown in Fig. 10.11 (b) is in fact due to correlations. Figure 10.13 demonstrates the change of the amplitude 2D-FTS when the biexcitonic dephasing time is altered. Here, we have used the same parameters as in Fig. 10.11 (b), except of the dephasing times of the biexcitons (c.p. parameter sets

XI and XII). Since the dephasing time has now been decreased, the biexcitonic features are smoothed out. That means that, by chosing certain material parameters, the biexcitonic features can no longer be identified, as it was the case in Fig. 10.10.

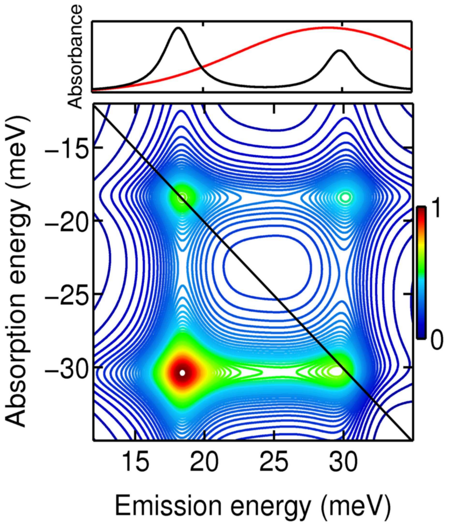

Figure 10.13: Amplitude 2D-FTS for the cross-linear excitation case including intra-sites heavy-light hole coupling without crossing of the valence bands. For the electron-coupling parameter J^e=22 meV. Here parameter set XII has been used.

In conlusion, we have seen that the excitonic reduced masses play an important role for the biexcitonic features in 2D-FTS. Such features could also be measured by the cross-linear excitation scheme and give a possibility for a detailed investigation of bound and unbound biexcitons.

10.3 Conclusions

As it has been shown in Chapeter 10, the provision for only the intra-site heavy-light hole coupling, does not influence the amplitude 2D-FTS for the cross-linear case shown in Figure 10.10. Thus the reason for the reduction of this non-diagonal peak in Ref. [8] could be possibly found in future work by including into our model such mechanisms like inter-site heavy-light hole coupling or by investigation of the influence of the effective masses or by the population dynamics. Additionally, we have discussed the interesting case of the artifact of the model due to positive curvature of the valence band. In fact, this case has similar reasons for appearing of the third exciton as it has been demonstrated for the dimerized lattice [4, 39]. In our case we have the optical transition at the intersection point, which in dimerized lattice would corresponds to the parallel bands. It would be interesting to prove such a presumption for our situation by studing of the wave functions.

The theoretical presumption (mechanism) in Chapter 10.2 about the influence of the electron-coupling parameter, respectively the electron effective mass, on biexcitonic binding energy has to be proved experimentally. The fact that the bound biexciton has not been observed in amplitude 2D-FTS could be ascribed to the chosen parameter set. Even though the electron-coupling parameter of 22 meV corresponds to the effective mass of the GaAs bulk, this does not mean that the bulk properties have been modeled properly. Only the complete set of parameters could possibly lead to a satisfactory modeling of the realistic case. We do not rule out that by choosing the proper set of the parameters the influence of the intra-site heavy-light hole coupling could probably have a more pronounced effect.

Chapter 11

Disorder effects on 2D-FTS

A detailed description of nonlinear optics of coupled systems in the presence of disorder-induced inhomogeneous broadening is a formidable task. In this chapter we demonstrate how the imaginary and real parts of the spectra of the rephasing and non-rephasing modes of 2D-FTS can be used to obtain a good estimate of the homogeneous and the inhomogeneous broadening of the excitonic resonances in semiconductor nanostructures. We illustrate this method on hand of a model of two quantum well structures. At the beginning we give a short review and an example of the well known nonlinear experiments, which are used for the determination of homogeneous and inhomogeneous broadenings.

11.1 Application of nonlinear experiments to disordered samples

In the past decades, various optical techniques have been used to investigate and unravel the structure of electronic states in semiconductor nanostructures and other material systems [4, 5, 15, 40, 41]. Spatially resolved linear optical measurements give information about homogeneous and inhomogeneous broadening separately. Typically, however, they provide only general information, e.g., the total line width. In addition, different nonlinear optical techniques were used to investigate the amounts of homogeneous and inhomogeneous broadening, see Ref. [4] and references therein.

In semiconductor nanostructures, many-body Coulomb interaction strongly alters the nonlinear optical response [4, 15, 21, 41, 42]. Even at the Hartree-Fock level, e.g., the traces of time-resolved FWM are significantly modified and signals for the *wrong* time ordering appear [4, 15, 20, 41, 43]. Additionally, already in the low-intensity third-order $\chi^{(3)}$-limit, characteristic dependencies of the nonlinear transients and spectra on the polarization directions of the incident pulses and couplings among optically-isolated resonances appear due to many-body correlations [4, 15, 21, 23, 31, 41, 44, 45, 46].

As mentioned, a detailed microscopic description of coupled excitons in the presence of disorder is a formidable task. Thus, well-established knowledge is lacking on this topic. It was, however, shown that Hartree-Fock renormalizations influence the temporal width of photon echoes in weakly disordered semiconductor quantum wells [24]. Very interesting biexciton-induced polarization-dependent quantum beats have been measured in strongly disordered quantum wells and were modeled on the basis of a simplified level scheme in Ref. [34]. Later, it became possible to describe these phenomena on the basis of a microscopic many-body theory that phenomenologically includes disorder-induced inhomogeneous broadening [47]. Ref. [14] includes both biexciton correlations and disorder on a microscopic level. The numerically computed FWM transients presented there show, in agreement with experiments, a polarization-dependent disorder-induced dephasing, i.e., a disorder-induced decay of the FWM amplitude that depends on the polarization directions of the incident beams.

Pump-probe measurements provide one-dimensional spectral information that cannot distinguish between homogeneous and inhomogeneous broadening. Hole burning can find the homogeneous contribution to the optical line width and by comparing to the linear spectrum provides an estimation of the inhomogeneous contribution [4].

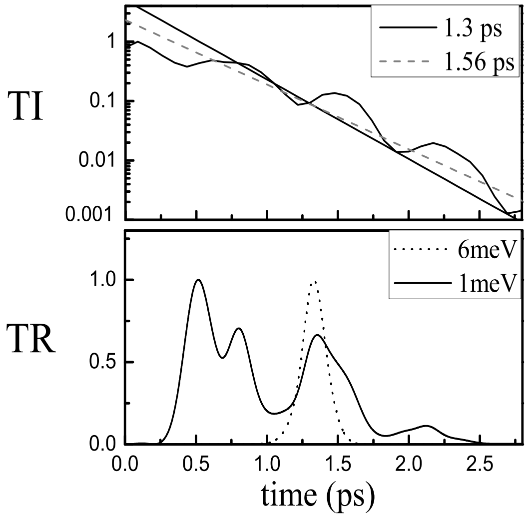

Figure 11.1: Time-integrated and time-resolved traces for $\sigma^+\sigma^+\sigma^+$ excitation. The TI-(TR)-data have been calculated using inhomogeneous Gaussian broadening $\gamma^{inhom} = 1$ meV ($\gamma^{inhom} = 1$ meV and 6 meV). Dipole-matrix elements are taken to be identical and $T_2^{h,l} = 1.3$ ps. Solid (dashed) lines in the TI figure correspond to dephasing times 1.3 (1.56) ps [48]. Here parameter set XIII has been used.

Four-wave-mixing experiments show photon-echoes in the time-resolved (TR) traces [4, 49]. Their temporal width is determined by the inhomogeneous line width. However, for systems where more than a single resonance is simultaneously excited, the width of the echo is ill defined due to beating [4, 6, 50], in particular for small inhomogeneous broadening. Figure 11.1 demonstrates the TR-signal for a quantum well system, where the separation between h and l excitons is around 6 meV and the inhomogeneous broadening has been modeled by a Gaussian function with the width of both 1 meV and 6 meV. The homogeneous broadening of the h and l excitons in our simulations has been taken for the simplicity to be the same (0.51 meV) for these data. Even for inhomogeneous broadening twice bigger than the homogeneous one, the simulations show (lower figure in Fig. 11.1), that the determination of the temporal width, consequently the inhomogeneous broadening is not possible. Another problem in the interpretation of photon echo experiments on a quantum well system is that the contribution of the single exciton to inhomogeneous broadening can not be extracted due to beating.

In order to determinate the ratio between the homogeneous and inhomogeneous broadening further measurements are needed, namely time-integrated (TI) traces (upper figure in Fig. 11.1). The TI-data yield the dephasing rate, i.e., the homogeneous width. However, in the presence of more than just a single optical resonance the decay parameter can not uniquely be determined and a fitting procedure is needed. It must also be mentioned, that the fitting procedure is a non-trivial task due to non-Markovian effects [51]. Non-Markovian effects lead to a plateau of the TI-trace at short timescale after/during the pulse excitation. That means, that only by taking memory effects into account, it would be possible to estimate the reference point of the straight lines. Otherwise, by doing numerical simulations, by a fit the correct dephasing times can be obtained.

In this chapter we demonstrate, that in particular for weak disorder the well known methods based on FWM experiments are not effective for the determination of the homogeneous and inhomogeneous broadenings. We suggest here to use the 2D-FTS experiment in order to determine the ratio of the homogeneous and inhomogeneous broadening in the presence of different kinds of couplings, including many-body couplings, for such systems, which show more than one single resonance. It will be shown that this ratio can be defined for each resonance separately. In the following chapter we consider an artificial quantum well structure as a demonstration of the method and later we apply this method to a real quantum well structure.

11.2 Determination of the homogeneous and inhomogeneous broadenings

One of the benefits of 2D-FTS is the possibility to measure the imaginary and real parts of the spectra simultaneously. In the following, we focus on the imaginary part and compare the spectrograms of the non-rephasing and the rephasing modes

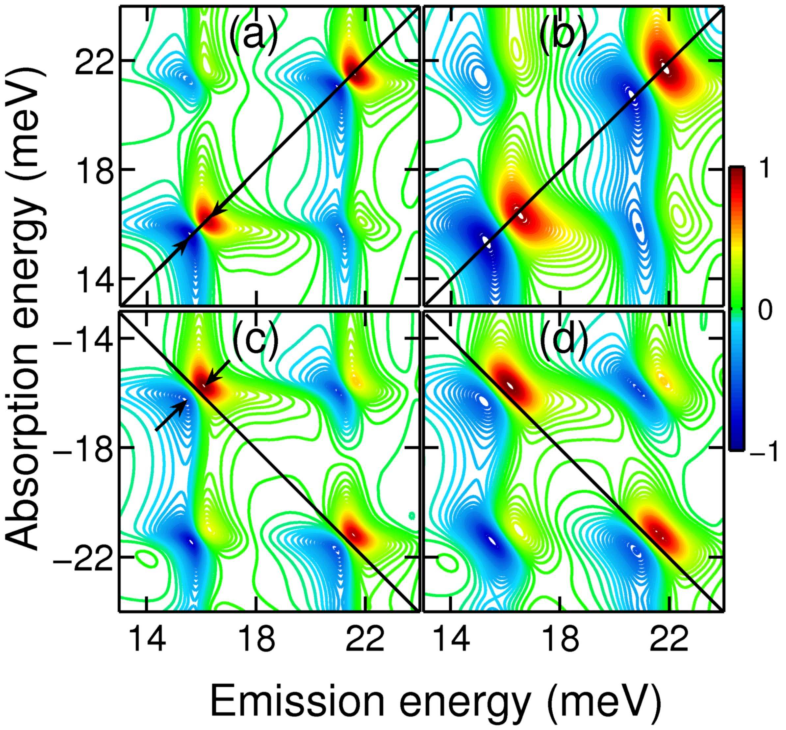

Figure 11.2: Normalized imaginary-part spectra for $\sigma^+\sigma^+\sigma^+$ excitation. For the non-rephasing (rephasing) mode homogeneously- (a) ((c)) and inhomogeneously-broadened spectra (b) ((d)). In (b) and (d) the spectra have been broadened by a Gaussian of width $\gamma^{inhom} = 0.6$ meV. The arrows in (a) and (c) indicate $\Delta\Omega^{hom}$ of the h exciton [48]. Here parameter set XIII has been used.

for an artificial quantum well system.

In order to make the following analysis more transparent, we use in our calculations the same magnitude for the heavy- and light-hole matrix elements, i.e., we neglect the (ideal)[1] reduction factor of $1/\sqrt{3}$ for the light-hole transitions. Furthermore, we consider a symmetric situation where the excitation pulses are tuned to the middle in between the resonances and take equal dephasing times of the h- and l-resonances. The optical transition dipole-matrix elements μ are chosen to model circularly polarized selection rules, see Fig. 3.2.

Numerically calculated results for the imaginary parts of 2D-FTS spectra are shown in Fig. 11.2. Generally, the line shapes of the signatures near the diagonal

---

[1] This value corresponds to the GaAs bulk material.

show a dispersive character for all considered cases. This observation allows us to suggest a method for the determination of the amount of the homogeneous and inhomogeneous broadening from a combination of the rephasing and non-rephasing 2D-FTS measurements.

We begin with the homogeneously broadened imaginary part 2D-FTS for the $\sigma^+\sigma^+\sigma^+$ excitation for the non-rephasing and rephasing modes, see Figs. 11.2 (a) and (c), respectively. If the Coulomb correlations are neglected, i.e., on the Hartree-Fock level, this set-up generates uncoupled h and l excitonic transitions. The rephasing and non-rephasing modes yield h and l excitonic peaks on the diagonal. These resonances are, however, coupled by many-body Coulomb correlations, e.g., biexcitons [4, 47, 52]. As a result of the Coulomb-correlation induced coupling, two off-diagonal features appear (Chapter 7). Figs. 11.2 (a) and (c) show that the strengths of the non-diagonal peaks for the rephasing mode is stronger than for the non-rephasing mode, which could be a general feature of the two modes (see the similar behavior for three-level system, Fig. 4.2).

In general, the non-rephasing (Fig. 11.2 (a), (b)) and the rephasing (Fig. 11.2 (c), (d)) spectra differ in orientation of the dispersivity of the peaks. In the rephasing case, we see that the nodes between positive and negative contributions are oriented parallel to the diagonal. In the non-rephasing case, however, the nodes are oriented perpendicularly to the diagonal. This constitutes a fundamental difference in the character of the spectral signatures in the two modes of 2D-FTS. As in, e.g., dispersive off-resonant pump-probe spectra, the energetic separation of the positive maxima and negative minima $\Delta\Omega^{hom}$, which for the h excitonic peak is shown by the arrows in Figs. 11.2 (a) and (c), is proportional to the homogeneous line width of this particular peak. If only the homogeneous broadening is presented, the energetic interval $\Delta\Omega^{hom}$ does not depend on the mode of the experiment, cp. Figs. 11.2 (a) and (c), nor does it depend on polarization directions of the incident beams (not shown in figure).

We now phenomenologically incorporate inhomogeneous broadening into our calculations (Figs. 11.2 (b) and (d)), by convoluting the 2D-FTS signal along the diagonal with Gaussian functions of width γ^{inhom} [4, 10]. Clearly, this procedure leads to an elongation of the peaks along the diagonal for both the rephasing and the non-rephasing modes. Due to the perpendicular orientation of the dispersive line shape in the non-rephasing and the rephasing cases, see Figs. 11.2 (a) and (c), the inhomogeneous broadening acts differently on the two modes. The main difference is that due to the orientation of the dispersive line shape along the diagonal in the non-rephasing case the inhomogeneous broadening basically adds to the homogeneous one, while in the rephasing case, due to the perpendicular orientation, the homogeneous and inhomogeneous contributions, they remain mainly separated.

Also in the presence of the inhomogeneous broadening, Figs. 11.2 (b) and (d), we determine the energetic distance between the maxima and minima of the h exciton along the diagonal for non-rephasing and perpendicular to the diagonal for rephasing spectra as shown by the arrows in Figs. 11.2 (a) and (c), i.e., we use the same definition of $\Delta\Omega$ for the inhomogeneously broadened spectra. To analyze the behavior of $\Delta\Omega$ when inhomogeneous broadening is added, we show in Fig. 11.3 the ratio $\Delta\Omega^{total}/\Delta\Omega^{hom}$ as a function of the input parameters $\gamma^{inhom}/\gamma^{hom}$, i.e., the ratio between inhomogeneous and homogeneous broadening in the model. The dotted lines display the idealized expectations, i.e., $\Delta\Omega^{total}/\Delta\Omega^{hom}$=1 for the rephasing case and $\Delta\Omega^{total}/\Delta\Omega^{hom} = (\gamma^{inhom} + \gamma^{hom})/\gamma^{hom}$ for the non-rephasing mode, respectively. While for the rephasing situation $\Delta\Omega^{total}$ stays nearly constant as γ^{inhom} increases, Fig. 11.3 shows a nearly linear increase for the non-rephasing case. The deviations from the expected dependencies are partly caused by the half-moon shape of the maxima and minima in imaginary 2D-FTS and due to the overlap between the excitonic peaks. This suggestion can be proved by the calculations for the system with a lager energetic distance between the resonances.

On the other hands, the distance between minima and maxima $\Delta\Omega^{hom}$ is only

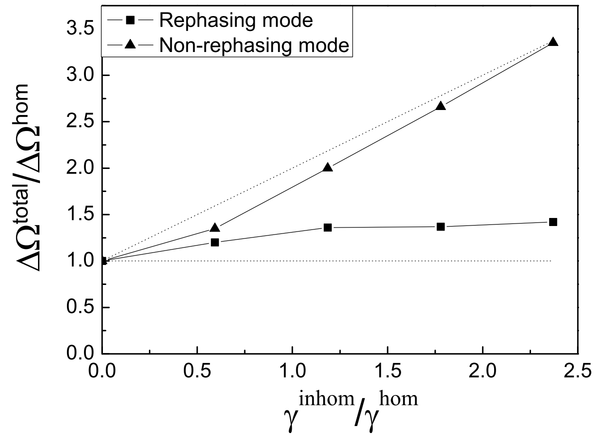

Figure 11.3: Relation of energetic distance between the maximum and the minimum of the h excitonic peak (i) $\Delta\Omega^{hom}$ for the imaginary-part homogeneously broadened spectrum and (ii) $\Delta\Omega^{total}$ for the inhomogeneously broadened 2D-FTS, both for $\sigma^+\sigma^+\sigma^+$ polarization as a function of $\frac{\gamma^{inhom}}{\gamma^{hom}}$. The inhomogeneous broadening parameter has been chosen to be γ^{inhom} =0., 0.3, 0.6, 0.9, and 1.2 meV and dephasing rate for the h exciton $\gamma_h = \gamma^{hom}$ =0.51 meV. The dotted lines identify the idealized expectation. Here parameter set XIII has been used.

proportional to γ^{hom}. Therefore we have some coefficient, which results from the deviation of the parallel line from the ideal case for the rephasing mode. This fact and the fact that overlap between the peaks increases by increasing of the inhomogeneous broadening leads to the discrepancies for the small $\gamma^{inhom}/\gamma^{hom}$ and good agreement for bigger values of the ratio for the non-rephasing mode (Fig. 11.3).

In our particular case, we modeled a rather wide quantum well with quite small energetic separation between the h- and l excitons and therefore the overlap between these resonances rises significantly with increased inhomogeneous broadening. This leads to an increase of the rephasing curve above 1 in Fig. 11.3 which would be absent for a larger energetic distance between the resonances, e.g., narrower quantum wells.

In the non-rephasing case, inhomogeneous broadening leads to a partial cancellation of the negative and positive contributions to the imaginary-part spectrum, which does not happen in the rephasing situation. Therefore, we expect a different behavior of the amplitude at the positions of the excitons when including inhomoge-

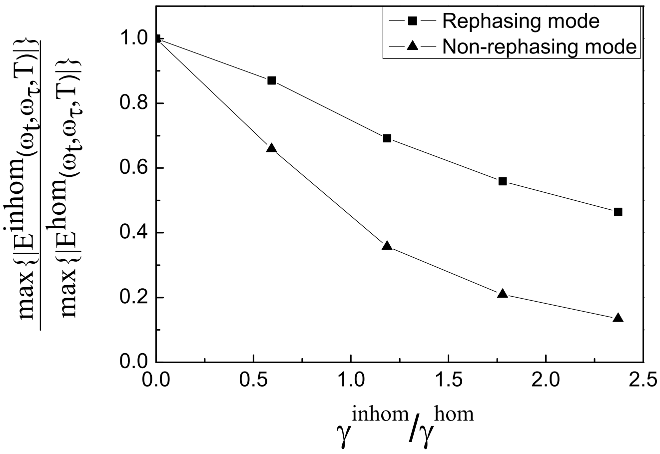

Figure 11.4: Decay of the normalized maxima of amplitude 2D-FTS at the h excitonic peak for the $\sigma^+\sigma^+\sigma^+$ polarization as a function of $\frac{\gamma^{inhom}}{\gamma^{hom}}$ for inhomogeneous broadening parameter γ^{inhom} =0., 0.3, 0.6, 0.9, and 1.2 meV and dephasing rate for the h exciton $\gamma_h = \gamma^{hom}$ =0.51 meV. Here parameter set XIII has been used.

neous broadening for the two modes. This is indeed the case, as is shown in Fig. 11.4, where we have plotted the maximum of the h exciton amplitude as function of the inhomogeneous broadening. As expected, the decay of the non-rephasing amplitude with the increase of the inhomogeneous broadening is clearly stronger than that of the rephasing mode, i.e., one can also use the ratio between the rephasing and non-rephasing amplitudes as a measure of the degree of inhomogeneous broadening. This theoretical results are in agreement (not shown here) with the experimental data for the sample considered in the next chapter.

The emphasis of this chapter lies on the difference of rephasing vs. non-rephasing spectra. It has been shown that even for otherwise identical model parameters, inhomogeneous broadening influences both kinds of spectra in a profoundly different way. This suggests to use two-dimensional Fourier-transform spectroscopy as a novel method for the determination of inhomogeneous broadening in such cases, where the material system exhibits several optical resonances, which might be both homogeneously and inhomogeneously broadened to a different extent. The advantage of our method is that we analyze *dispersive* line shapes, instead of spectra with *absorptive* character. Line-shape analysis of absorptive lines yields lager errors if compared to that of dispersive lines. In the following chapter we apply this method to a real quantum well structure in order to determine the ratio of the inhomogeneous to homogeneous broadening for h and l excitons.

11.3 Comparison between theory and experiment

In this chapter we consider a GaAs quantum well structure with AlGaAs barriers (given in [37]). Usually, the first excitonic peak (h) has a longer dephasing time as the second (l) one (here we use the parameter set XIV in Appendix B). In order to compensate for the oscillator strength of the strong h exciton, the excitation pulses are centered at the l exciton.

We begin with the h excitonic peak and consider the real and imaginary part for the rephasing and non-rephasing modes of 2D-FTS (Fig. 11.5 and 11.6, respectively). The analysis of the line shape of the h excitonic peak shows that the real-part 2D-FTS for this exciton has a dispersive character. Thus we choose the rephasing and non-rephasing mode of the real-part 2D-FTS to estimate the ratio between homogeneous and inhomogeneous broadenings for the h exciton.

It was demonstrated in the Chapter 11.2, that the homogeneous broadening is proportional to the energetic separation of the positive maxima and negative minima in the rephasing spectra. Here, the homogeneous broadening extracted from Fig 11.5 (c) for the h exciton is $\Omega_{rephasing} \propto 1.14$ meV. Since the parameter set has been used to fit the experiment shown in Fig 11.5 (d), the homogeneous broadening of the h exciton in the experiment yields the same value of 1.14 meV.

Additionally, the inhomogeneous broadening can be extracted from the non-rephasing mode presented in Fig 11.5 (a) (theory) and Fig 11.5 (b) (experiment). The pure inhomogeneous broadening is $\propto \Omega_{non-rephasing} - \Omega_{rephasing}$, thus 0.69 meV arises from the experiment and 0.717 meV from the theory.

The width of the Gaussian function used in the numerical simulation was

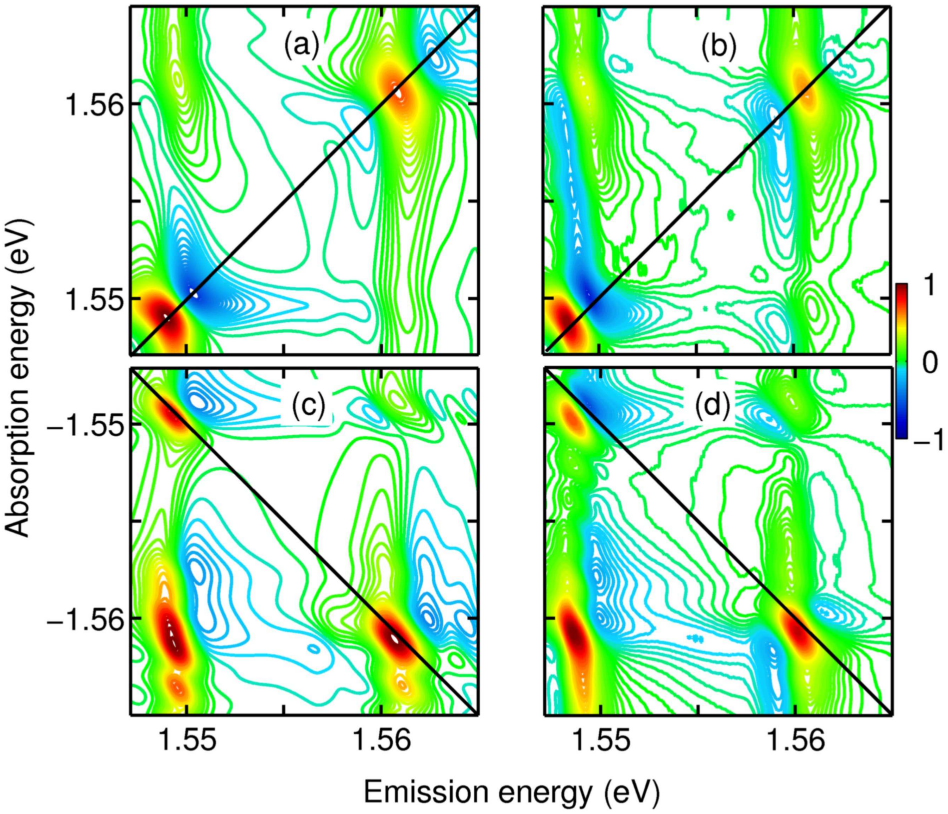

Figure 11.5: Normalized real-part 2D-FTS for the co-circular excitation case at the l excitonic peak. Rephasing and non-rephasing mode: theory (a), (c) and experiment (b),(d), respectively [37]. For the numerical calculations the spectra have been inhomogeneously broadened by a parameter γ^{inhom} =0.72 meV using a Gaussian function. Here parameter set XIV has been used.

0.72 meV, which means that the coefficient input/output for the estimation of the inhomogeneous broadening approaches unity for our theory. The input for the homogeneous broadening, which corresponds to $\hbar$/(dephasing time) of the h exciton, provides the coefficient around 0.45. (It would be interesting to check how "robust" those coefficients are for the l exciton.) The fact that the coefficient approaches unity for inhomogeneous broadening means that the degree of inhomogeneous broadening can well be determined by measuring the non-rephasing and rephasing modes. Furthermore, by definition the pure inhomogeneous broadening does not depend on the homogeneous one.

The ratio of the homogeneous and inhomogeneous broadening extracted from the theory (Fig 11.5 (a) and (c)) is $\propto$ 1.59 meV and from the experiment $\propto$ 1.65 meV, which differ by only 3.6%. This discrepancy is due to a too large value of the inhomogeneous broadening taken in our calculations.

The input ratio following from the input data is the $\hbar$/(dephasing time) of the h exciton to the Gaussian width is 0.71 (1.59) meV, without (with) taking into account the coefficients. It has to be noted, that modeling of disorder by Gaussian functions is a rough model for the estimation of the inhomogeneous broadening, but still good in our particular case. Differently to the quantum well considered in Chapter 11.2 the quantum well here has a larger h-l energetic separation, which is about 11 meV.

We should also note that we are here studying inhomogeneous broadening which is of the same order as the homogeneous one. Thus we are in a regime of Fig. 11.3 where the numerical results deviate considerably from the idealized expectation, due to a coefficient for the homogeneous broadening.

We now focus on the l exciton. In order to estimate the ratio for the l exciton, the l excitonic peak has to feature the dispersive character. Due to large h-l separation and small h exciton binding energy, the l exciton is placed on top of the continuum of the h exciton. This changes the line shape of the l excitonic peak to absorptive like (see diagonal peak at the higher[2] energy Fig 11.5). We therefore make profit from applying our method to the imaginary-part 2D-FTS (Fig 11.6), which shows dispersive line shape for the l exciton.

We consider the rephasing mode (Fig 11.6 (c) and (d)) and find that homogeneous broadening is $\propto$ 1.585 meV for the theory and 1.41 meV for the experiment, which gives a variance of about 11%. If the coefficient 0.45 is correct also for the l exciton, then the dephasing time for the l exciton extracted from the experiment is about 1.04 ps, instead of 0.8 ps taken in the numerical simulations in Fig 11.6 (c). In fact, bigger dephasing time and the corresponding dipole-matrix-element ratio would lead to a better agreement (Fig 11.6 (a), (c)) for the peak distribution and

---

[2] Here it means the absolute value of the energy.

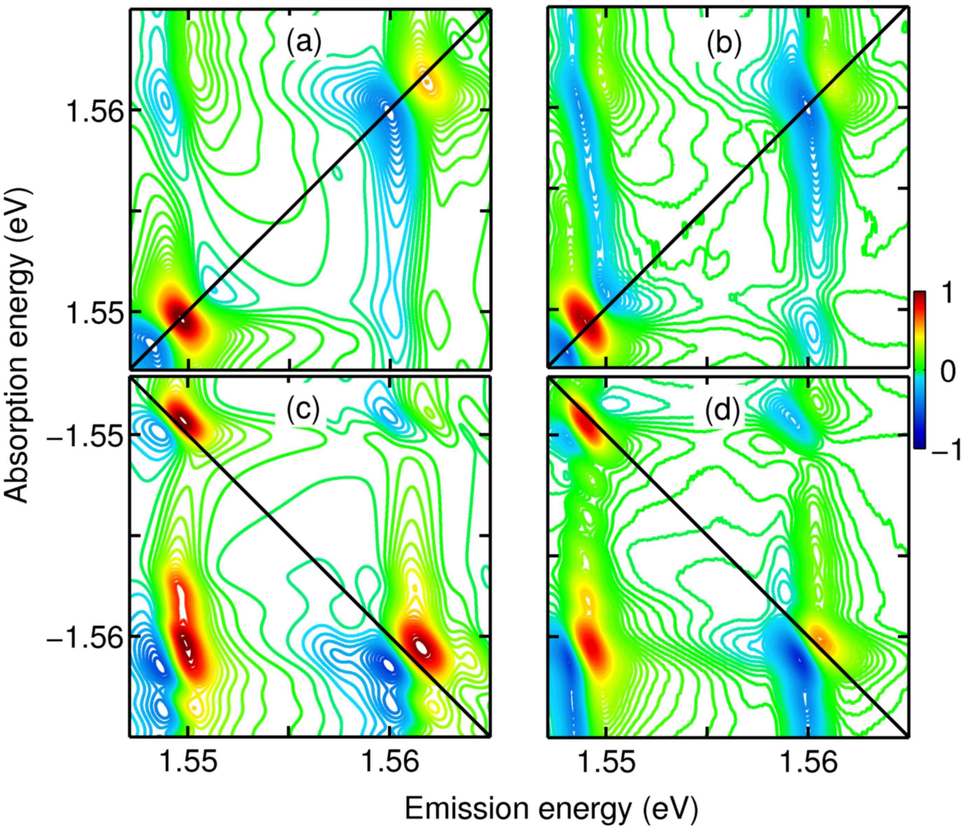

Figure 11.6: Normalized imaginary-part 2D-FTS for the co-circular excitation case at the l excitonic peak. Rephasing and non-rephasing mode: theory (a), (c) and experiment (b),(d), respectively [37]. For the numerical calculations the spectra have been inhomogeneously broadened by a parameter γ^{inhom} =0.72 meV using a Gaussian function. Here parameter set XIV has been used.

homogeneous broadening with experiment (Fig 11.6 (b), (d)). As it was mentioned in previous chapters the fitting of the linear spectra is not a simple procedure due to its dependence on the number N of the sites. Furthermore, the coefficient input/output has to be substantiated by further calculations. It also might depend on the material under study.

We concentrate now on the non-rephasing mode of the experimental and theoretical spectra (Fig 11.6 (a) and (b)). Defined in the same way as for the h exciton, the pure inhomogeneous broadening extracted from the numerical simulation yields 0.715 meV (the input value is 0.72 meV) and the experimental data provides 0.35 meV. If the presumption for the coefficient is true, we can interpret these values as absolute values of the inhomogeneous broadening.

The discrepancy of the experimentally determined value of the pure inhomogeneous broadening and the theoretical one could have several reasons. The first reason is that the modeling of the disorder by a Gaussian convolution of the total spectrum is not good for the l exciton in our particular case, i.e. disorder acts on h and l exciton differently. In fact, it would be surprising if both excitons are influenced by disorder in the same way, given their different wave functions and energies. On the other hand, using our method suggested here, one is able to determine different degrees of inhomogeneous broadening for different resonances from the experiment alone, without performing any numerical calculation.

Another point, which certainly has an influence is the fact that the l exciton is sitting on top of the h exciton continuum, i.e. due to the spectral position of the l exciton the influence of the disorder on this peak can not be modeled by Gaussian function. This physical reason might also change the coefficient input/output (0.72/0.715 meV$\simeq$1, Fig 11.6 (a)) for the experimental value (Fig 11.6 (b)). All of this interesting hypothesis have to be substantiated further in order to demonstrate the power of this novel method for the determination of homogeneous and inhomogeneous broadenings.

11.4 Conclusions

The imaginary- and real-part of 2D-FTS in the rephasing and non-rephasing modes is used to analyze the homogeneous and inhomogeneous broadening of excitonic resonances for different quantum well structures. Microscopic calculations that include h and l excitons as well as coherent biexcitonic many-body correlations reveal distinct differences between the rephasing and non-rephasing spectra. A procedure is proposed that allows us to separate disorder-induced broadening in complex systems that show several coupled resonances. We obtain, by comparing experiment and theory, the ratio between the homogeneous and inhomogeneous broadenings for the h exciton with the accuracy about 4%. This small error is due to a too large value of the inhomogeneous broadening taken in the calculations. For the l exciton it is about 46%, which is due to a not optimal choice of the dephasing time for the l exciton, and probably also to different inhomogeneous broadenings for h and l excitons, which is not implemented in our theory.

It has been shown by comparing experiment and theory for h and l excitons, that the pure inhomogeneous broadening could be defined with very good accuracy below 1%, which luckily does not dependent on how good the homogeneous broadening has been estimated. Thus, the initial idea to consider the ratio between homogeneous and inhomogeneous broadening defined by using 2D-FTS as a unique value, calls for comparison with experiments.

It is remarkable that the good accuracy of the estimation of the inhomogeneous broadening by using rephasing and non-rephasing modes does not need the comparison with a theoretical calculation. That means only by measuring of these both modes it is possible to extract the inhomogeneous broadening for each resonance separately. These resonances also include biexcitonic ones, which allows the detailed investigation of those homogeneous and inhomogeneous broadenings of the biexcitons as well.

We do not claim, that the theory based on the one-dimensional tight-binding model is able to model the exact values of the homogeneous and inhomogeneous broadenings. On the other hand, using this approach we are able to suggest a novel method for the determination of the various broadenings of simultaneously excited resonances. Thus, in this chapter, we demonstrated the power of the 2D-FTS measurements.

Chapter 12

Coherent excitation spectroscopy

In this chapter we discuss a method which is similar to 2D-FTS, the Coherent-Excitation-Spectroscopy (CES), in that it also yields two-dimensional spectral information. This method has been developed in the 90ths and has been successfully applied to the investigation of excitonic features in ordered and disordered systems [10] as well as of the biexcitonic ones, see Ref. [4] and references therein. The sequence of the pulses in CES corresponds to the rephasing mode of 2D-FTS. However, the first pulse is spectrally narrow, i.e., has a long temporal duration. The most important question is: How different is the information extracted from 2D-FTS and CES. In the following we compare 2D-FTS and CES, and illustrate the differences for an artificial quantum well system as a case study.

12.1 Comparison with 2D-FTS

We begin with a quantum well system which features a single exciton. The linear spectrum and the excitation pulses for CES and 2D-FTS experiments are illustrated in Fig. 12.1 (upper figure). We prepare the experiment in such a way, that the excitation conditions in both cases differ only by the first pulse. In CES we apply a long Gaussian pulse with δ=10 ps, which is centered at the exciton and in 2D-FTS it is centered at the continuum edge with δ=0.005 ps. Generally, in CES all three pulses excite the system simultaneously. On the other hand, the 2D-FTS method

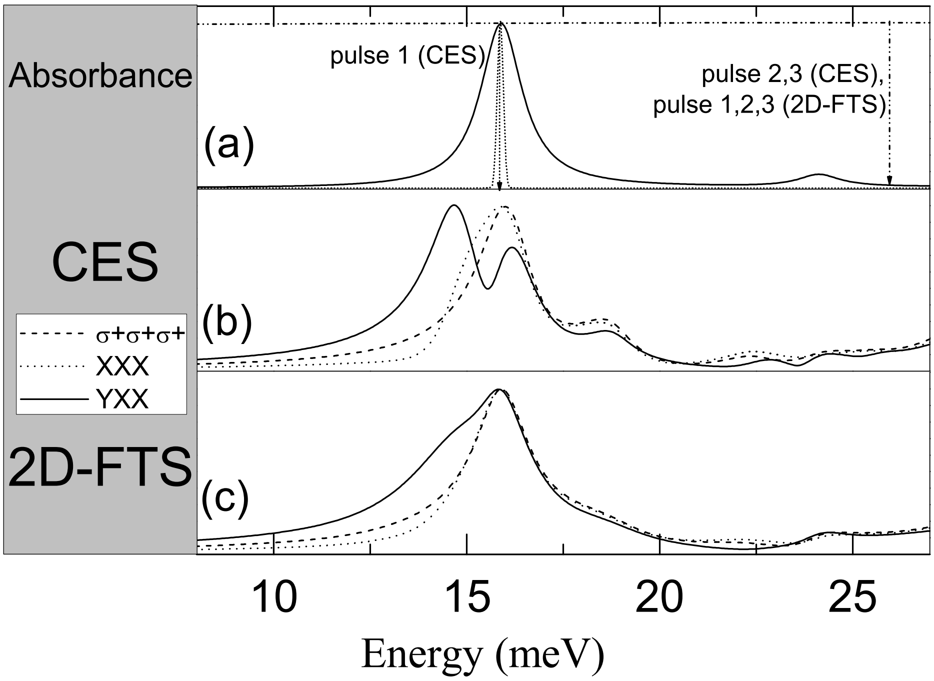

Figure 12.1: The upper figure presents the linear spectrum (solid line) and the spectra of the Gaussian pulses with the δ=10 ps (short dot) and δ=0.005 ps (dash dot dot). The middle figure presents the amplitude CES-signal for the co-circular (dashed line), co-linear (dotted line) and cross-linear (solid line) cases, respectively. The lower figure shows a cut of 2D-FTS at the excitonic absorption energy of 15.87 meV. Here parameter set XV has been used.

implies the variation of the delay time between the first and second (third) pulses. In order to compare those methods we consider a cut in 2D-FTS at the absorption energy of the exciton. The emission energy then corresponds to the detection energy in CES. Figure 12.1 (middle figure) shows the amplitude CES-signal [1] for the co-circular, co- and cross-linear excitation situations and Fig. 12.1 (lower figure) shows the corresponding cuts of the 2D-FTS. The biexcitonic signatures have been expected in CES and they have been seen also in 2D-FTS [8]. Since the biexcitonic binding energy is about 1 meV, we detect the bound biexcitons below the excitonic

---

[1] Normally, the CES-signal is a square of the absolute value of the amplitude.

peak and, respectively, unbound biexcitons above it. These features are present also in 2D-FTS. However, not so strongly pronounced like in CES. Generally, the single excitonic signature is suppressed for the cross-linear excitation case due to correlations which leads to more pronounced biexcitonic features. Interestingly the proportion between the absolute values exciton/biexciton in CES and 2D-FTS is different and for the cross-linear excitation in CES the excitonic signature is even weaker than the biexcitonic one (Fig. 12.1, solid line). It is noteworthy that the Pauli-blocking calculations show no differences between the CES data and the cut of 2D-FTS. That means that the Coulomb effects are responsible for the differences between 2D-FTS and CES.

To make those differences more transparent, we discuss both methods in the time domain. For this reason we apply the simplified Semiconductor Bloch Equations, shown in Chapter 6 and calculate the contribution P^{Cb} to the third-order polarization, which contains only the Hartree-Fock and the correlation terms. The Pauli-blocking term is omitted since it is the same for CES and 2D-FTS. We transform the polarization in the time domain into the frequency domain by Fourier-transformation with respect to real time t for CES and for 2D-FTS. For the latter additionally also with respect to the delay time τ. We concentrate on the excitonic peak. For the CES this means, that the excitation energy $\hbar\omega_{exc}$, respectively the excitation pulse frequency, corresponds to the excitonic frequency ω_X. For the 2D-FTS we consider the cut at the absorption energy $\hbar\omega_{absrp}$ corresponding to this excitonic frequency, $\hbar\omega_{absrp} = \hbar\omega_{exc}$.

Thus the Coulomb term for CES is:

$$P^{Cb}_{CES}(\omega_{det} = \omega_t, \omega_{exc} = \omega_X) \propto \frac{V}{\hbar^4} \frac{|\mu|^2 \; E_1^* \; \theta(t) \; E_2 \; \mu^* E_2}{i\gamma\hbar^{-1} \; (2i\omega_X - i\omega_{BX} - (\beta\hbar^{-1} - \gamma\hbar^{-1}))}$$

$$\left(\frac{1}{i(\omega_X - \omega_{BX} - \omega_t) - \beta\hbar^{-1}} + \frac{1}{i(\omega_X - \omega_t) + \gamma\hbar^{-1}} \right) \tag{12.1}$$

We compare Eq. 12.1 with the Coulomb term for 2D-FTS, which results in:

$$P^{Cb}_{2D-FTS}(\omega_{emiss}=\omega_t,\omega_{absrp}=\omega_X) \propto \frac{V}{\hbar^4}\ \frac{|\mu|^2\ E_1^*\ \theta(t)\ E_2\ \mu^* E_2}{i\gamma\hbar^{-1}\ (2i\omega_X - i\omega_{BX} - \beta\hbar^{-1})}$$

$$\left(\frac{1}{i(\omega_X-\omega_{BX}-\omega_t)-(\gamma\hbar^{-1}+\beta\hbar^{-1})}+\frac{1}{i(\omega_X-\omega_t)+\gamma\hbar^{-1}}\right), \tag{12.2}$$

where ω_{BX} corresponds the biexcitonic frequency, $\gamma\hbar^{-1}$ and $\beta\hbar^{-1}$ are the dephasing rates of the exciton and biexciton, respectively. These equations show different dephasings of the biexcitons for CES and 2D-FTS.

Usually, in 2D-FTS extremely short pulses are used. They excite all the relevant transitions when they arrive at the sample. The subsequent dynamics is then freely evolving, including the relaxation due to dephasing. Differently to 2D-FTS, in CES the first Gaussian pulse with δ=10 ps can be considered as a continuous excitation on the timescale of the experiment. That means that in CES the system, respectively the excitons, are driven continuously with the pulse frequency of the exciton while 2D-FTS involves the free evolution of the coherent excitation in the many-body system. This renders the 2D-FTS method a special tool for the investigation of many-body couplings. In our particular case it has been analytically proven (Eq. 12.1 and Eq. 12.2), that the excitation of the whole excitonic spectrum influences via the many-body effects the biexcitonic signatures, in particular, their homogeneous width. The homogeneous broadening of the bound biexcitons in CES is given by β and 2D-FTS yields $\beta+\gamma$. The Figure 12.2 is a schematical representation of the CES and 2D-FTS amplitudes for the cross-linear excitation situation. The amplitude CES shows the strong biexcitonic peak at the lower energy, which has the same homogeneous broadening γ like the exciton[2] (Fig. 12.2, green line). Since in 2D-FTS the biexcitonic peak obtains an additional broadening γ, the excitonic

---

[2] In our numerical simulations presented in Fig. 12.1 we have used γ=β.

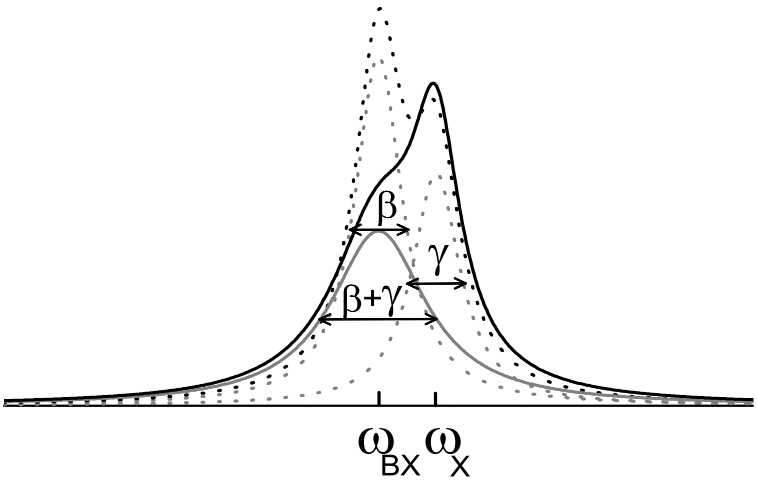

Figure 12.2: Schematical representation of the formation of CES- (black dotted line) and 2D-FTS- (black solid line) amplitude spectra for the cross-linear excitation. ω_X and ω_{BX} correspond to excitonic and bound biexcitonic resonances, respectively (gray lines).

peak now is much stronger than the biexcitonic one, even though the single excitonic peak is further suppressed by the cross-linear excitation.

Obviously, for small homogeneous broadening γ the excitonic and the biexcitonic signature must be more pronounced, and for a vanishing γ the difference between CES and 2D-FTS should be absent. Figure 12.3 proves this fact. We consider the case when the homogeneous broadening of the exciton γ and biexciton β are equal (Fig. 12.3(a)) and compare with the situation $\beta = 2\gamma$ (Fig. 12.3(b)). The differences between CES and 2D-FTS are clearly reduced with decreasing of γ. That proves our analytical results.

In summary, we suggest that the above demonstrated features of the nonlinear experiments can be generalized in the following way. As an example, we consider the linear response of an optical short pulse excitation. If the power of the excitation pulse increases, at a certain point the linear response turns into a nonlinear one. That means nonlinear processes start to play a role. The prediction based

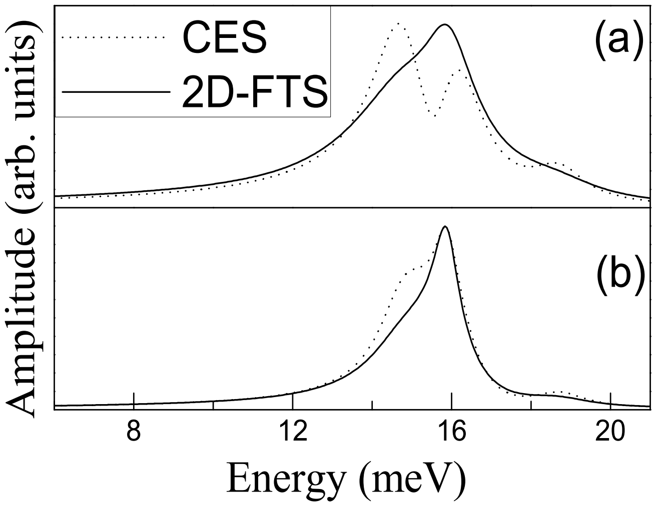

Figure 12.3: Amplitude spectra calculated for the cross-linear case CES (dotted line) and 2D-FTS (solid line). The upper figure (a) is taken from Fig. 12.1 (the solid lines for CES and 2D-FTS in Fig.12.1). The parameter set XV has been used for (a) and the same parameter set except $\gamma\hbar^{-1}$=0.5 ps^{-1} and $\beta\hbar^{-1}$=1 ps^{-1} for (b).

on the discussion above is that the spectrum (called "pseudo-linear" now) will show transitions, which obtain additional broadening due to many-body couplings. Those couplings will be caused by the nonlinearities, which are a consequence of the high power excitation. Thus the short high power excitation pulse leads to a nonlinear response, which contains the information about many-body coupling within the highly excited system. Hence the pseudo-linear spectrum will obtain additional broadening due to many-body coupling. As a conclusion, the measurement of linear spectra by the short excitation pulse should be done very carefully in order to stay in the linear regime. This prediction could be analytically proved for example by including additional equations of motion for the population beyond the coherent limit.

Chapter 13

Summary and outlook

The goal of this work was the interpretation of experimental data obtained by applying the recently developed optical two-dimensional Fourier-transform spectroscopy method to semiconductor nanostructures. For this purpose a one-dimensional tight-binding model has been applied. Thus, when starting this work, a quantitative agreement between numerical simulations and experiments was not expected to exist.

In order to gain a basic understanding of the 2D-FTS method and to illustrate its fundamental features, in particular the dependence on polarization direction of the excitation pulses, we began by considering non-interacting particles. In fact, this method being based on a FWM-experiment, we have expected a polarization dependence also of 2D-FTS. In this tutorial part we took advantage of extremely short excitation pulses. This allowed us to treat non-interacting particles analytically. We established the signatures of 2D-FTS for a so called three-level system roughly modeling a system exhibiting heavy-hole and light-hole excitonic transitions. The 2D spectra displayed additionally to the diagonal peaks, which correspond to each single transition, also non-diagonal peaks, which identify the coupling between single resonances. This illustrates the benefits of this method, namely separate information about the resonances and about their mutual couplings. Notably, additional information is contained in the imaginary-part and real-part spectra. They display different spectral signatures for the co- and cross-linear excitation cases, but the same amplitude spectra for this simple model. We have also explained the fundamental difference between rephasing and non-rephasing modes, which initially seems to be trivial. Later, for more realistic models of a semiconductor quantum well we took advantage of this difference.

Generally, in this work mostly the rephasing mode has been considered. This has several reasons. The first reason was the available experimental data, the second is that the rephasing mode in certain sense corresponds to the well-known photon-echo experiment, thus we had some background for the investigation of novel features. However it was also important to demonstrate the analytical calculation and the fundamental study for non-interacting particles in non-rephasing case. This will be a basis for further exploring of the non-rephasing mode. It is interesting that for a normal FWM-experiment the *wrong* sequence of the pulses yields no signal for a simple level system. However, in the non-rephasing mode we have a sequence of pulses which differs from the conventional one in wrong-sequence FWM-experiments. The specific feature of this mode is the appearance of beating of the diagonal peaks (transitions), while for the rephasing mode the beating of the "coupling"-peaks occurs in the off-diagonal positions.

Additionally, in this preliminary part we also gained information about the dependence of the spectra of the two modes on material parameters such as optical dipole-matrix elements and dephasing times. Thus by comparing experiment with theoretical simulation it should be possible to estimate the material parameters. In order to proceed, the Coulomb interaction, including correlations, had to be taken seriously. It turned out that such a comparison enhances the numerical effort considerably.

The main part of this work was concerned with many-body effects. For the detailed investigation of the influence of various aspects of the Coulomb interaction we have applied the Semiconductor Bloch Equations which were written in terms of the pure correlation term. In the frame of our extended one-dimensional tight-binding model the non-diagonal peaks for the co-circular excitation occur only due to correlation. It was expected that this leads to beating of the non-diagonal terms for the rephasing mode and to beating of the diagonal terms for the non-rephasing mode. Thus by treating the Coulomb effects on different levels it is possible to estimate the weight of each aspect of the many-particle interaction separately. Here it was necessary to adjust the oscillator strengths of the peaks and to consider the real- or imaginary-part spectra. The advantage is that the couplings (including Coulomb-induced couplings) can be treated separately from the resonances. In particular, this feature of the method is interesting for the application to novel semiconductor compounds.

In addition, by considering the continuum transitions it was possible to monitor the change of their character from pure inhomogeneous towards mixed (additional homogeneous) character by looking at 2D-FTS at different contributions of Coulomb interaction, i.e., only Pauli-blocking, Hartree Fock, and correlations.

Including the correlation term up to third order in the light field allowed us to investigate in detail different correlation signatures such as bound, unbound and mixed biexcitons. We have proposed a mechanism of exciton-biexciton coupling. We suggested that changing the reduced mass of the exciton leads to a change of the biexcitonic binding energy. By taking different biexcitonic dephasing times, this influence can be extracted due to the identification of bound, unbound and mixed biexcitons. This scenario has to be proved by experiment (for example: measurements of 2D-FTS for different material systems).

Also polarization dependence provides information about Coulomb-induced correlations. It is to be noted that these correlations are taken in the coherent $\chi^{(3)}$-limit. That means that the excitation is chosen to be sufficiently weak, i.e. the population dynamics is given by that of the product of the polarization and its complex conjugated. Furthermore, as we consider only weak excitation fields we are able to truncate the hierarchy of the differential equations and take into account correlations consistently in this limit. This allowed us to make a fair comparison with the experiment, albeit on the basis of a simplified model system. Here the discrepancies had to be mentioned, which we have encountered in the comparison for the cross-linear case. Possible reasons are: additional relaxation processes, which were not included in the theory, the low dimensionality of our model or going beyond the $\chi^{(3)}$-limit in the experiment.

Furthermore, band-mixing effects could be an issue. In order to investigate these effects, at the first time the one-dimensional tight-binding model has been extended to including intra-site coupling. We have diagonalized the matrix in order to fit the band structure calculated by a $k \cdot p$-theory, and applied the model parameters extracted from this study in our numerical calculations. It has been shown, that this particular intra-site coupling does not solve the above mentioned problem with the non-diagonal peak for the cross-linear case. Probably the intra-site coupling parameter has been taken to small or further couplings such as inter-site couplings should be taken into account. In order to prove this hypothesis, the comparison between experiment and theory has to be done on both the experimental as well as the theoretical side more systematically in the future.

It is noteworthy, that the experimental data for different polarization directions show different strength of the peak, which is not surprising, but they also show different dephasing times. This interesting point has to be investigated more carefully in the future as well. It would be more reasonable to start from a system which contains only a single excitonic resonance. In this way we avoid additional couplings between different kinds of excitons (h and l) due to correlations. A possible reason for the dependence of the dephasing time on polarization could be the above mentioned coupling. This has to be studied further.

One of the benefits of 2D-FTS is the additional information due to real- and imaginary-part spectra. By comparing experimental and theoretical spectra we could determine the global phase. It turned out to be generally important to simulate exactly the experimental conditions such as the excitation pulses. We have demonstrated that 2D-FTS does depend on excitation conditions. In particular, real- and imaginary-part spectra are even more sensitive to changes in these conditions.

We have found that these spectra for rephasing and non-rephasing modes due to their dispersive character and fundamental difference between the modes can be applied for determination of the homogeneous and inhomogeneous broadenings. The advantage of this method is that it is applicable also in case of small disorder (compared to homogeneous width), whereas the methods in the time domain have their own difficulties. One of such difficulties is the beating if more than just a single resonance is excited. Since our method of determination of the widths is based on an analysis of the line shape, the amplitude is irrelevant. The most important difference to other experiments is that in 2D-FTS we can determinate the broadenings (or, in general, analyze them) for each single resonance (in our case, exciton) separately, even in the presence of couplings, which include Coloumb-induced couplings. The most significant issue is that the inhomogeneous broadening can be determinate with very good accuracy by only analyzing experimental data for rephasing and non-rephasing modes. Theoretical calculations that have to be fitted to experimental data are not necessary. We also showed that the 2D-FTS method fundamentally differs from the Coherent-Excitation-Spectroscopy method.

Finally we can state that 2D-FTS could solve problems arising in the other methods based on the FWM-experiment and thus complements these nonlinear experimental schemes. This stimulates further investigation of this method and its applications.

Bearing in mind the knowledge gained in this thesis, we see that the 2D-FTS method is capable for investigation a new materials. It allows us to characterize details of disorder effects. Correlations, which leads to different kinds of biexcitons can be studied in detail. In general, since this method is applicable to various kinds of couplings, one can envisage its application also to material systems contained in an optical micro cavity, showing exciton-cavity coupling. This would prove the great potential of 2D-FTS for a large variety of systems, a method that was derivated from NMR originally.

Chapter 14

Zusammenfassung

Das Ziel dieser Dissertation ist die Interpretation von Daten, die mit der kürzlich entwickelten optischen zweidimensionalen Fourier-Transform-Spektroskopie (2D-FTS) von Halbleiter-Nanostrukturen gewonnen werden können. Dies erfordert auch eine Analyse der Möglichkeiten dieser Methode und ihres Anwendungsbereiches.

Diese multi-dimensionale spektroskopische Methode stammt von der Methode Nuklear-Magnetischen-Resonanz (NMR) ab [1]. NMR und ihre Analoga haben ihre Anwendung sowohl in der Biologie als auch in den anderen Naturwissenschaften wie Chemie und Physik gefunden [2].

Hier wenden wir in Analogie zu NMR die 2D-FTS Methode auf Halbleiter-Nanostrukturen an und vergleichen theoretische Ergebnisse mit den Experimenten, die bisher in der Arbeitsgruppe von Prof. S. Cundiff durchgeführt wurden [3]. Die Hauptidee von 2D-FTS ist es, Informationen über das angeregte System und über die Kopplungen innerhalb des angeregten Systems zu entflechten. 2D-FTS basiert auf dem Vier-Wellen-Mischungs-(VWM)-Experiment. Dabei wird die Probe durch eine Reihe von drei Anregungspulsen a, b, c für die Rephasing-Mode und b, a, c für die Non-rephasing-Mode angeregt. Das Signal wird dann in die Richtung $-k_a + k_b + k_c$ gemessen. Dieses Signal wird Fourier-transformiert bezüglich der realen Zeit t und der Zeitverzögerung τ zwischen erstem und zweitem Puls.

Die Arbeit stellt die erste theoretische Behandlung der 2D-FTS Methode auf der Basis eines ein-dimensionalen tight-binding Models dar. Deshalb wird im ersten

Teil der Arbeit ein System nicht-wechselwirkender Teilchen betrachtet. Wir lernen die fundamentalen Unterschiede zwischen Rephasing und Non-rephasing-Moden kennen. Diese Unterschiede und die zusätzlichen Informationen, so wie sie in den Realteil- und Imaginärteil-Spektren vorliegen, werden im zweiten Teil ausgenutzt, um die inhomogene und homogene Verbreiterung reeller Quantenfilme zu bestimmen.

Wir haben festgestellt, dass die Vergleiche zwischen Theorie und Experiment eine gute Anpassung der unterschiedlichen Modellparameter erfordern. Die Berücksichtigung der Coulomb-Wechselwirkung, einschließlich der Coulomb-induzierte Korrelationen ist dabei ganz wesentlich.

Die weiteren theoretischen Untersuchungen von 2D-FTS betreffen die Auswirkung von verschiedenen Ordnungen der Coulomb-Wechselwirkung. Zusätzlich haben wir den Einfluss der Anregungsbedingungen betrachtet und deren Einfluss auf die Amplituden- und insbesondere die Realteil- und Imaginärteil-Spektren studiert.

In dieser Arbeit wurde zum ersten Mal das ein-dimensionale tight-binding Model erweitert. Wir haben zusätzliche Intra-Site Schwerloch-Leichtloch-Kopplung eingeführt und deren Wirkung auf 2D-FTS erforscht. Dies erlaubte uns, Bandstrukturen zu simulieren, die denen der realen Heterostrukturen ähneln.

Schließlich haben wir bewiesen, dass die 2D-FTS Methode sich von der kohärenten Anregungsspektroskopie in einem wichtigen Punkt unterscheidet.

Wir haben gezeigt, dass unsere Methode einige Probleme, die bei den anderen nichtlinear Methoden auftauchen können, die auf dem VWM-Experiment basieren, nicht aufweist.

Vorausblickend und basierend auf den Erkenntnissen, die in dieser Arbeit gewonnen wurden, glauben wir, dass 2D-FTS gut geeignet ist für die Untersuchungen an neuen Halbleitermaterialen, für deren detaillierte Charakterisierung bezüglich der Unordnung und der Coulomb-Korrelationen. Letztere schließen verschiedene Arten der Biexcitonen mit ein.

Im Allgemein kann 2D-FTS auf verschiedene Systeme angewendet werden, die Kopplungen aufweisen, z.B. Exciton-Cavity Systeme. Diese Anwendung würde das große Anwendungspotenzial der Methode deutlich machen, die ursprünglich im Rahmen der NMR entwickelt wurde.

Appendix A

Optical Bloch Equations for three-level systems

A.1 Non-rephasing mode

In the following we consider non-interacting particles. We apply the one-dimensional tight-binding model, include the selection rules (see Chapter 3.2) and solve the Optical Bloch Equations analytically up to third order, i.e in the $\chi^{(3)}$-regime.

Here we denote the modulus of the dipole-matrix element by μ_1 and the dephasing rate by γ_1 for the transition with the lower energy ("heavy-hole" transition), for the higher energy transition ("light-hole" transition) we use μ_2 and γ_2, respectively.

We start with the non-rephasing mode and calculate the third-order polarization for the cross-linear excitation situation. We use the following δ-excitation pulses:

$$\begin{aligned}
\vec{E}_a(t) &= \eta_0 e^{i\vec{k_a}\cdot\vec{r}}\delta(t)\begin{pmatrix}0\\1\end{pmatrix}\ , \\
\vec{E}_b(t) &= \eta_0 e^{i\vec{k_b}\cdot\vec{r}}\delta(t-\tau)\begin{pmatrix}1\\0\end{pmatrix}\ , \\
\vec{E}_c(t) &= \eta_0 e^{i\vec{k_c}\cdot\vec{r}}\delta(t-T)\begin{pmatrix}1\\0\end{pmatrix}, \qquad \text{(A.1)}
\end{aligned}$$

where $\tau \leq 0$ and $T \geq 0$. It is to be noted, that in the time domain for the non-rephasing case we have the following ordering of the pulses: b, a, c. In this work we use the following notation: the abbreviation of the polarization direction of the signal $-k_a + k_b + k_c$ for the cross-linear excitation pulses is YXX. That means the second pulse a is linearly Y-polarized.

We solve the Optical Bloch Equations in rotating-wave approximation for the polarization $p_{h_1e_2}$ and for the populations and intra-band coherences in the valence bands $n_{h_1h_2}$ and the conduction band, respectively $n_{e_1e_2}$ [4]. We use the extended one-dimensional tight-binding model given in Chapter 3.1, however, with the couplings and the Coulomb-terms put to zero.

$$\begin{aligned}
\frac{d}{dt}p_{h_1e_2} &= (-i\omega_{h_1e_2} - \hbar^{-1}\gamma_{h_1e_2})p_{h_1e_2} + \frac{i}{\hbar}\vec{E}(t)\cdot \\
&\quad [\vec{\mu}^*_{h_1e_2} - \sum_e \vec{\mu}^*_{h_1e} n^e_{ee_2} - \sum_h \vec{\mu}^*_{he_2} n^h_{hh_1}], \qquad (A.2) \\
\frac{d}{dt}n^e_{e_1e_2} &= \frac{i}{\hbar}\sum_h [\vec{E}(t)\cdot\vec{\mu}^*_{he_2}p^*_{he_1} - \vec{E}^*(t)\cdot\vec{\mu}_{he_1}p_{he_2}], \qquad (A.3) \\
\frac{d}{dt}n^h_{h_1h_2} &= i\omega_{h_1h_2}n^h_{h_1h_2} + \frac{i}{\hbar}\sum_e [\vec{E}(t)\cdot\vec{\mu}^*_{h_2e}p^*_{h_1e} - \vec{E}^*(t)\cdot\vec{\mu}_{h_1e}p_{h_2e}]. \qquad (A.4)
\end{aligned}$$

In the following we use the same notation as given in Fig. 3.2.

The first linearly X-polarized pulse b generates the polarizations p_{11}, p_{31}, p_{22}, p_{42} where the spin-dependency of the corresponding transitions are taken into account. This leads to the following equation:

$$\frac{d}{dt}p^{(0|1|0)}_{11} = (-i\omega_{11} - \hbar^{-1}\gamma_2)\, p^{(0|1|0)}_{11} + \frac{i}{\hbar}\,\vec{\mu}^*_{11}\cdot\vec{E}_b \qquad (A.5)$$

The notation $p^{(-1|1|1)}$ means the FWM-propagation direction $(-k_a|k_b|k_c)$. By solving the differential equation Eq. A.5 for all polarizations generated by the first pulse, we obtain:

$$\begin{aligned}
p^{(0|1|0)}_{11} &= \frac{i}{\sqrt{2}\hbar}\,\mu_2\eta_0\theta(t-\tau)e^{-i(\omega_{11}-i\hbar^{-1}\gamma_2)(t-\tau)}e^{i\vec{k}_b\cdot\vec{r}}, \\
p^{(0|1|0)}_{31} &= \frac{i}{\sqrt{2}\hbar}\,\mu_1\eta_0\theta(t-\tau)e^{-i(\omega_{31}-i\hbar^{-1}\gamma_1)(t-\tau)}e^{i\vec{k}_b\cdot\vec{r}}, \\
p^{(0|1|0)}_{22} &= \frac{i}{\sqrt{2}\hbar}\,\mu_2\eta_0\theta(t-\tau)e^{-i(\omega_{22}-i\hbar^{-1}\gamma_2)(t-\tau)}e^{i\vec{k}_b\cdot\vec{r}}, \\
p^{(0|1|0)}_{42} &= \frac{i}{\sqrt{2}\hbar}\,\mu_1\eta_0\theta(t-\tau)e^{-i(\omega_{42}-i\hbar^{-1}\gamma_1)(t-\tau)}e^{i\vec{k}_b\cdot\vec{r}}. \qquad (A.6)
\end{aligned}$$

The second pulse generates the populations $n^{e(-1|1|0)}_{11}$ and $n^{e(-1|1|0)}_{22}$ in the electron band:

$$\frac{d}{dt}n^{e(-1|1|0)}_{11} = -\frac{i}{\hbar}\vec{E}^*_a\cdot\sum_h \vec{\mu}_{h1}p^{(0|1|0)}_{h1}, \qquad (A.7)$$

where h=1, 2, 3, 4. We obtain an analogous result for the population in the electron band $n_{22}^{e(-1|1|0)}$, which characterizes the light-hole transition. It yields:

$$\begin{aligned} n_{11}^{e(-1|1|0)} &= \frac{i}{2\hbar^2}\,\eta_0^2 e^{i(-\vec{k}_a+\vec{k}_b)\cdot\vec{r}}\theta(t)\theta(-\tau)(e^{i(\omega_{11}-i\hbar^{-1}\gamma_2)\tau}\mu_2^2 - e^{i(\omega_{31}-i\hbar^{-1}\gamma_1)\tau}\mu_1^2), \\ n_{22}^{e(-1|1|0)} &= \frac{i}{2\hbar^2}\,\eta_0^2 e^{i(-\vec{k}_a+\vec{k}_b)\cdot\vec{r}}\theta(t)\theta(-\tau)(e^{i(\omega_{42}-i\hbar^{-1}\gamma_1)\tau}\mu_1^2 - e^{i(\omega_{22}-i\hbar^{-1}\gamma_2)\tau}\mu_2^2). \end{aligned} \tag{A.8}$$

The differential equations of motion for the populations and coherences of the holes in the valence bands are given as:

$$\begin{aligned} \frac{d}{dt}n_{11}^{h(-1|1|0)} &= -\frac{i}{\hbar}\vec{E}_a^* \cdot \vec{\mu}_{11}p_{11}^{(0|1|0)}, \\ \frac{d}{dt}n_{31}^{h(-1|1|0)} &= i\Delta\omega n_{31}^{(-1|1|0)} - \frac{i}{\hbar}\vec{E}_a^* \cdot \vec{\mu}_{11}p_{11}^{(0|1|0)}, \end{aligned} \tag{A.9}$$

where $\Delta\omega = \omega_{11} - \omega_{31} = \omega_{22} - \omega_{42}$ is the frequency difference between $''h''$ and $''l''$ valence states. Analogous equations exist for the other hole densities and coherences. We solve the differential equations for all the populations and coherences. This yields:

$$\begin{aligned} n_{11}^{h(-1|1|0)} &= i\left(\frac{\mu_2\eta_0}{\sqrt{2}\hbar}\right)^2\ \theta(t)\theta(-\tau)e^{i(-\vec{k}_a+\vec{k}_b)\cdot\vec{r}}e^{i(\omega_{11}-i\hbar^{-1}\gamma_2)\tau}, \\ n_{31}^{h(-1|1|0)} &= -\frac{i}{2\hbar^2}\ \mu_1\mu_2\eta_0^2\theta(t)\theta(-\tau)e^{i(-\vec{k}_a+\vec{k}_b)\cdot\vec{r}}e^{-i\Delta\omega t}e^{i(\omega_{11}-i\hbar^{-1}\gamma_2)\tau}, \\ n_{13}^{h(-1|1|0)} &= \frac{i}{2\hbar^2}\ \mu_1\mu_2\eta_0^2\theta(t)\theta(-\tau)e^{i(-\vec{k}_a+\vec{k}_b)\cdot\vec{r}}e^{i\Delta\omega t}e^{i(\omega_{31}-i\hbar^{-1}\gamma_1)\tau}, \\ n_{33}^{h(-1|1|0)} &= -i\left(\frac{\mu_1\eta_0}{\sqrt{2}\hbar}\right)^2\ \theta(t)\theta(-\tau)e^{i(-\vec{k}_a+\vec{k}_b)\cdot\vec{r}}e^{i(\omega_{31}-i\hbar^{-1}\gamma_1)\tau}, \\ n_{22}^{h(-1|1|0)} &= -i\left(\frac{\mu_2\eta_0}{\sqrt{2}\hbar}\right)^2\ \theta(t)\theta(-\tau)e^{i(-\vec{k}_a+\vec{k}_b)\cdot\vec{r}}e^{i(\omega_{22}-i\hbar^{-1}\gamma_2)\tau}, \\ n_{42}^{h(-1|1|0)} &= \frac{i}{2\hbar^2}\ \mu_1\mu_2\eta_0^2\theta(t)\theta(-\tau)e^{i(-\vec{k}_a+\vec{k}_b)\cdot\vec{r}}e^{-i\Delta\omega t}e^{i(\omega_{22}-i\hbar^{-1}\gamma_2)\tau}, \\ n_{24}^{h(-1|1|0)} &= -\frac{i}{2\hbar^2}\ \mu_1\mu_2\eta_0^2\theta(t)\theta(-\tau)e^{i(-\vec{k}_a+\vec{k}_b)\cdot\vec{r}}e^{i\Delta\omega t}e^{i(\omega_{42}-i\hbar^{-1}\gamma_1)\tau}, \\ n_{44}^{h(-1|1|0)} &= i\left(\frac{\mu_1\eta_0}{\sqrt{2}\hbar}\right)^2\ \theta(t)\theta(-\tau)e^{i(-\vec{k}_a+\vec{k}_b)\cdot\vec{r}}e^{i(\omega_{42}-i\hbar^{-1}\gamma_1)\tau}. \end{aligned} \tag{A.10}$$

The third pulse enters and generates a polarization, which is described by the following equations of motion:

$$\begin{aligned}
\frac{d}{dt}p_{11}^{(-1|1|1)} &= (-i\omega_{11}-\hbar^{-1}\gamma_2)\,p_{11}^{(-1|1|1)} - \frac{i}{\hbar}\,\vec{E}_c\cdot(\vec{\mu}^*_{11}n_{11}^{e(-1|1|0)} + \vec{\mu}^*_{11}n_{11}^{h(-1|1|0)} + \vec{\mu}^*_{31}n_{31}^{h(-1|1|0)}),\\
\frac{d}{dt}p_{31}^{(-1|1|1)} &= (-i\omega_{31}-\hbar^{-1}\gamma_1)\,p_{31}^{(-1|1|1)} - \frac{i}{\hbar}\,\vec{E}_c\cdot(\vec{\mu}^*_{31}n_{11}^{e(-1|1|0)} + \vec{\mu}^*_{11}n_{13}^{h(-1|1|0)} + \vec{\mu}^*_{31}n_{33}^{h(-1|1|0)}),\\
\frac{d}{dt}p_{22}^{(-1|1|1)} &= (-i\omega_{22}-\hbar^{-1}\gamma_2)\,p_{22}^{(-1|1|1)} - \frac{i}{\hbar}\,\vec{E}_c\cdot(\vec{\mu}^*_{22}n_{22}^{e(-1|1|0)} + \vec{\mu}^*_{22}n_{22}^{h(-1|1|0)} + \vec{\mu}^*_{42}n_{42}^{h(-1|1|0)}),\\
\frac{d}{dt}p_{42}^{(-1|1|1)} &= (-i\omega_{42}-\hbar^{-1}\gamma_1)\,p_{42}^{(-1|1|1)} - \frac{i}{\hbar}\,\vec{E}_c\cdot(\vec{\mu}^*_{42}n_{22}^{e(-1|1|0)} + \vec{\mu}^*_{22}n_{24}^{h(-1|1|0)} + \vec{\mu}^*_{42}n_{44}^{h(-1|1|0)}).
\end{aligned} \tag{A.11}$$

At this stage we denote $\omega_2=\omega_{11}=\omega_{22}$, $\omega_1=\omega_{31}=\omega_{42}$ and the difference between them $\Delta\omega=\omega_2-\omega_1$. From the resulting microscopical polarizations arise the following total macroscopic polarizations for the cross-linear excitation YXX:

$$\begin{aligned}
\vec{P}^{(-1|1|1)}\quad(t,\tau,T) \;&= \vec{\mu}_{11}p_{11}^{(-1|1|1)} + \vec{\mu}_{31}p_{31}^{(-1|1|1)} + \vec{\mu}_{22}p_{22}^{(-1|1|1)} + \vec{\mu}_{42}p_{42}^{(-1|1|1)}\\
&= \frac{1}{4}\left(\frac{\eta_0}{\hbar}\right)^3 e^{i(\vec{k}_c+\vec{k}_b-\vec{k}_a)\cdot\vec{r}}\,\Theta(t-T)\Theta(T)\Theta(-\tau)\\
&\Bigg[\begin{pmatrix}1\\ i\end{pmatrix}\mu_2^2 e^{-i(\omega_2-i\hbar^{-1}\gamma_2)(t-T)}\big(e^{i(\omega_2-i\hbar^{-1}\gamma_2)\tau}[2\mu_2^2-\mu_1^2e^{-i\Delta\omega T}]-\mu_1^2e^{i(\omega_1-i\hbar^{-1}\gamma_1)\tau}\big)\\
&-\begin{pmatrix}1\\ -i\end{pmatrix}\mu_1^2 e^{-i(\omega_1-i\hbar^{-1}\gamma_1)(t-T)}\big(e^{i(\omega_1-i\hbar^{-1}\gamma_1)\tau}[2\mu_1^2-\mu_2^2e^{i\Delta\omega T}]-\mu_2^2e^{i(\omega_2-i\hbar^{-1}\gamma_2)\tau}\big)\\
&-\begin{pmatrix}1\\ -i\end{pmatrix}\mu_2^2 e^{-i(\omega_2-i\hbar^{-1}\gamma_2)(t-T)}\big(e^{i(\omega_2-i\hbar^{-1}\gamma_2)\tau}[2\mu_2^2-\mu_1^2e^{-i\Delta\omega T}]-\mu_1^2e^{i(\omega_1-i\hbar^{-1}\gamma_1)\tau}\big)\\
&+\begin{pmatrix}1\\ i\end{pmatrix}\mu_1^2 e^{-i(\omega_1-i\hbar^{-1}\gamma_1)(t-T)}\big(e^{i(\omega_1-i\hbar^{-1}\gamma_1)\tau}[2\mu_1^2-\mu_2^2e^{i\Delta\omega T}]-\mu_2^2e^{i(\omega_2-i\hbar^{-1}\gamma_2)\tau}\big)\Bigg],
\end{aligned} \tag{A.12}$$

$$\begin{aligned}
\vec{P}^{(-1|1|1)}(t,\tau,T) \;&=\; \frac{i}{2}\left(\frac{\eta_0}{\hbar}\right)^3 e^{i(\vec{k}_c+\vec{k}_b-\vec{k}_a)\cdot\vec{r}}\,\Theta(t-T)\Theta(T)\Theta(-\tau)\begin{pmatrix}0\\ 1\end{pmatrix}\\
&\Big[\mu_2^2 e^{-i(\omega_2-i\hbar^{-1}\gamma_2)(t-T)}\big(e^{i(\omega_2-i\hbar^{-1}\gamma_2)\tau}[2\mu_2^2-\mu_1^2e^{-i\Delta\omega T}]-\mu_1^2e^{i(\omega_1-i\hbar^{-1}\gamma_1)\tau}\big)\\
&+\;\mu_1^2 e^{-i(\omega_1-i\hbar^{-1}\gamma_1)(t-T)}\big(e^{i(\omega_1-i\hbar^{-1}\gamma_1)\tau}[2\mu_1^2-\mu_2^2e^{i\Delta\omega T}]-\mu_2^2e^{i(\omega_2-i\hbar^{-1}\gamma_2)\tau}\big)\Big],
\end{aligned} \tag{A.13}$$

where $\tau \leq 0$ and $T \geq 0$.

If three excitation pulses are co-linearly polarized, the macroscopic polarization would also be given by Eq. A.13, however, with the four minus signs replaced by plus signs.

The co-circular situation $\sigma^+\sigma^+\sigma^+$ is more simple. Here we would have just two positive terms, as given in Eq. 4.2.

A.2 Rephasing mode

We continue with the calculation of the polarization for the rephasing mode. Here we use the following δ-excitation pulses:

$$\begin{aligned}\vec{E}_a(t) &= \eta_0 e^{i\vec{k_a}\cdot\vec{r}}\delta(t+\tau)\begin{pmatrix}0\\1\end{pmatrix}\\ \vec{E}_b(t) &= \eta_0 e^{i\vec{k_b}\cdot\vec{r}}\delta(t)\begin{pmatrix}1\\0\end{pmatrix}\\ \vec{E}_c(t) &= \eta_0 e^{i\vec{k_c}\cdot\vec{r}}\delta(t-T)\begin{pmatrix}1\\0\end{pmatrix},\end{aligned} \tag{A.14}$$

where now $\tau \geq 0$ and $T \geq 0$. It is to be noted, that in the time domain for the rephasing case we have the following ordering of the pulses: a, b, c. That means the abbreviation for the cross-linear excitation rephasing mode remains YXX as above.

The Y-polarized excitation pulse a enters first and generates the linear polarizations p_{11}, p_{31}, p_{22}, p_{42}. By carrying out the equations of motion Eq. A.2 we obtain:

$$\frac{d}{dt}p_{11}^{(1|0|0)} = \left(-i\omega_{11} - \hbar^{-1}\gamma_2\right) p_{11}^{(1|0|0)} + \frac{i}{\hbar}\vec{\mu}_{11}^* \cdot \vec{E}_a. \tag{A.15}$$

In order to achieve a signal in the FWM-propagation direction, differently to the non-rephasing situation, now the first pulse has to be conjugated. Therefore, by solving the differential equations, we obtain:

$$\begin{aligned}
p_{11}^{*(1|0|0)} &= \frac{1}{\sqrt{2}\hbar}\ \mu_2\eta_0\theta(t+\tau)e^{i(\omega_{11}+i\hbar^{-1}\gamma_2)(t+\tau)}e^{-i\vec{k}_a\cdot\vec{r}}, \\
p_{31}^{*(1|0|0)} &= -\frac{1}{\sqrt{2}\hbar}\ \mu_1\eta_0\theta(t+\tau)e^{i(\omega_{31}+i\hbar^{-1}\gamma_1)(t+\tau)}e^{-i\vec{k}_a\cdot\vec{r}}, \\
p_{22}^{*(1|0|0)} &= -\frac{1}{\sqrt{2}\hbar}\ \mu_2\eta_0\theta(t+\tau)e^{i(\omega_{22}+i\hbar^{-1}\gamma_2)(t+\tau)}e^{-i\vec{k}_a\cdot\vec{r}}, \\
p_{42}^{*(1|0|0)} &= \frac{1}{\sqrt{2}\hbar}\ \mu_1\eta_0\theta(t+\tau)e^{i(\omega_{42}+i\hbar^{-1}\gamma_1)(t+\tau)}e^{-i\vec{k}_a\cdot\vec{r}}. \qquad \text{(A.16)}
\end{aligned}$$

The second pulse b enters and generates the population and intra-band coherences. Equation A.3 is now modified corresponding to the propagation direction:

$$\frac{d}{dt}n_{11}^{e(-1|1|0)} = \frac{i}{\hbar}\vec{E}_b\cdot\sum_h \vec{\mu}_{h1}^{*}p_{h1}^{*(0|1|0)}, \qquad \text{(A.17)}$$

where h=1, 2, 3, 4. It leads to

$$\begin{aligned}
n_{11}^{e(-1|1|0)} &= \frac{i}{2\hbar^2}\ \eta_0^2 e^{i(-\vec{k}_a+\vec{k}_b)\}\cdot\vec{r}}\theta(t)\theta(\tau)(e^{i(\omega_{11}+i\hbar^{-1}\gamma_2)\tau}\mu_2^2 - e^{i(\omega_{31}+i\hbar^{-1}\gamma_1)\tau}\mu_1^2), \\
n_{22}^{e(-1|1|0)} &= \frac{i}{2\hbar^2}\ \eta_0^2 e^{i(-\vec{k}_a+\vec{k}_b)\cdot\vec{r}}\theta(t)\theta(\tau)(e^{i(\omega_{42}+i\hbar^{-1}\gamma_1)\tau}\mu_1^2 - e^{i(\omega_{22}+i\hbar^{-1}\gamma_2)\tau}\mu_2^2)
\end{aligned}$$

$$\text{(A.18)}$$

We solve the equation of motion for the populations and coherences in the valence bands Eq. A.4:

$$\begin{aligned}
n_{11}^{h(-1|1|0)} &= i\left(\frac{\mu_2\eta_0}{\sqrt{2}\hbar}\right)^2\ \theta(t)\theta(\tau)e^{i(-\vec{k}_a+\vec{k}_b)\cdot\vec{r}}e^{i(\omega_{11}+i\hbar^{-1}\gamma_2)\tau}, \\
n_{31}^{h(-1|1|0)} &= -\frac{i}{2\hbar^2}\ \mu_1\mu_2\eta_0^2\theta(t)\theta(\tau)e^{i(-\vec{k}_a+\vec{k}_b)\cdot\vec{r}}e^{-i\Delta\omega t}e^{i(\omega_{31}+i\hbar^{-1}\gamma_1)\tau}, \\
n_{13}^{h(-1|1|0)} &= \frac{i}{2\hbar^2}\ \mu_1\mu_2\eta_0^2\theta(t)\theta(\tau)e^{i(-\vec{k}_a+\vec{k}_b)\cdot\vec{r}}e^{i\Delta\omega t}e^{i(\omega_{11}+i\hbar^{-1}\gamma_2)\tau}, \\
n_{33}^{h(-1|1|0)} &= -i\left(\frac{\mu_1\eta_0}{\sqrt{2}\hbar}\right)^2\ \theta(t)\theta(\tau)e^{i(-\vec{k}_a+\vec{k}_b)\cdot\vec{r}}e^{i(\omega_{31}+i\hbar^{-1}\gamma_1)\tau}, \\
n_{22}^{h(-1|1|0)} &= -i\left(\frac{\mu_2\eta_0}{\sqrt{2}\hbar}\right)^2\ \theta(t)\theta(\tau)e^{i(-\vec{k}_a+\vec{k}_b)\cdot\vec{r}}e^{i(\omega_{22}+i\hbar^{-1}\gamma_2)\tau}, \\
n_{42}^{h(-1|1|0)} &= \frac{i}{2\hbar^2}\ \mu_1\mu_2\eta_0^2\theta(t)\theta(\tau)e^{i(-\vec{k}_a+\vec{k}_b)\cdot\vec{r}}e^{-i\Delta\omega t}e^{i(\omega_{42}+i\hbar^{-1}\gamma_1)\tau}, \\
n_{24}^{h(-1|1|0)} &= -\frac{i}{2\hbar^2}\ \mu_1\mu_2\eta_0^2\theta(t)\theta(\tau)e^{i(-\vec{k}_a+\vec{k}_b)\cdot\vec{r}}e^{i\Delta\omega t}e^{i(\omega_{22}+i\hbar^{-1}\gamma_2)\tau}, \\
n_{44}^{h(-1|1|0)} &= i\left(\frac{\mu_1\eta_0}{\sqrt{2}\hbar}\right)^2\ \theta(t)\theta(\tau)e^{i(-\vec{k}_a+\vec{k}_b)\cdot\vec{r}}e^{i(\omega_{42}+i\hbar^{-1}\gamma_1)\tau}. \qquad \text{(A.19)}
\end{aligned}$$

The third pulse generates the polarization and Eq. A.11 is valid for the rephasing case as well. The same abbreviation for the frequencies as used for the non-rephasing mode we apply below. We solve the differential equations for the microscopic polarization. This yields the macroscopic polarization:

$$
\begin{aligned}
\vec{P}^{(-1|1|1)}(t,\tau,T) &= \vec{\mu}_{11}p_{11}^{(-1|1|1)} + \vec{\mu}_{31}p_{31}^{(-1|1|1)} + \vec{\mu}_{22}p_{22}^{(-1|1|1)} + \vec{\mu}_{42}p_{42}^{(-1|1|1)} \\
&= \frac{1}{4}\left(\frac{\eta_0}{\hbar}\right)^3 e^{i(\vec{k}_c+\vec{k}_b-\vec{k}_a)\cdot\vec{r}}\Theta(t-T)\Theta(T)\Theta(\tau) \\
&\quad \Bigg[\begin{pmatrix}1\\ i\end{pmatrix} \mu_2^2 e^{-i(\omega_2-i\hbar^{-1}\gamma_2)(t-T)}(2\mu_2^2 e^{i(\omega_2+i\hbar^{-1}\gamma_2)\tau} - \mu_1^2 e^{i(\omega_1+i\hbar^{-1}\gamma_1)\tau}(1+e^{-i\Delta\omega T}) \\
&\quad - \begin{pmatrix}1\\ -i\end{pmatrix} \mu_1^2 e^{-i(\omega_1-i\hbar^{-1}\gamma_1)(t-T)}(2\mu_1^2 e^{i(\omega_1+i\hbar^{-1}\gamma_1)\tau} - \mu_2^2 e^{i(\omega_2+i\hbar^{-1}\gamma_2)\tau}(1+e^{i\Delta\omega T}) \\
&\quad - \begin{pmatrix}1\\ -i\end{pmatrix} \mu_2^2 e^{-i(\omega_2-i\hbar^{-1}\gamma_2)(t-T)}(2\mu_2^2 e^{i(\omega_2+i\hbar^{-1}\gamma_2)\tau} - \mu_1^2 e^{i(\omega_1+i\hbar^{-1}\gamma_1)\tau}(1+e^{-i\Delta\omega T}) \\
&\quad + \begin{pmatrix}1\\ i\end{pmatrix} \mu_1^2 e^{-i(\omega_1-i\hbar^{-1}\gamma_1)(t-T)}(2\mu_1^2 e^{i(\omega_1+i\hbar^{-1}\gamma_1)\tau} - \mu_2^2 e^{i(\omega_2+i\hbar^{-1}\gamma_2)\tau}(1+e^{i\Delta\omega T})\Bigg],
\end{aligned}
\tag{A.20}
$$

$$
\begin{aligned}
\vec{P}^{(-1|1|1)}(t,\tau,T) &= -\frac{i}{2}\frac{\eta_0^3}{\hbar}e^{i(\vec{k}_c+\vec{k}_b-\vec{k}_a)\cdot\vec{r}}\Theta(t-T)\Theta(T)\Theta(\tau)\begin{pmatrix}0\\ 1\end{pmatrix} \\
&\quad \Big[-\mu_2^2 e^{-i(\omega_2-i\hbar^{-1}\gamma_2)(t-T)}(2\mu_2^2 e^{i(\omega_2+i\hbar^{-1}\gamma_2)\tau} - \mu_1^2 e^{i(\omega_1+i\hbar^{-1}\gamma_1)\tau}(1+e^{-i\Delta\omega T})) \\
&\quad - \mu_1^2 e^{-i(\omega_1-i\hbar^{-1}\gamma_1)(t-T)}(2\mu_1^2 e^{i(\omega_1+i\hbar^{-1}\gamma_1)\tau} - \mu_2^2 e^{i(\omega_2+i\hbar^{-1}\gamma_2)\tau}(1+e^{i\Delta\omega T}))\Big],
\end{aligned}
\tag{A.21}
$$

where $\tau \geq 0$ and $T \geq 0$.

For the co-linear situation all terms in the Eq. A.21 are positive. Much more simple is the co-circular case, where the polarization contains only two terms, see Eq. 4.3.

Appendix B

Model parameters

set	I	II	III	IV	V
N number of the sites	10	10	10	40	10
a (nm) site separation	5	5	5	5	5
a_0/a regularization parameter	5	5	5	5	5
J^e(meV) coupling strength of the electron band	0	0	0	6	6
J^h(meV) coupling strength of the heavy-hole band	0	0	0	2	2
J^l(meV) coupling strength of the light-hole band	0	0	0	2.35	2.35
J^{hl}(meV) coupling strength between heavy- and light-hole band	0	0	0	0	0
T_2^h (ps) dephasing time of the heavy-hole exciton	1.3	1.3	1.3	1.3	1.3
T_2^l (ps) dephasing time of the light-hole exciton	1.3	1.3	0.8	0.8	0.8
T_2^{hh} (ps) dephasing time of the heavy-hole biexciton	1.04	1.04	1.3	1.3	1.3
T_2^{ll} (ps) dephasing time of the light-hole biexciton	1.04	1.04	0.8	0.8	0.8
$T_2^{(hl,lh)}$ (ps) dephasing time of the mixed (heavy- and light-hole) biexciton	0.52	0.52	0.5	0.5	0.5
$\hbar\Delta\omega$ (meV) heavy-light hole offset	6	6	11.9	11.9	11.9
$\lvert\frac{\mu_h}{\mu_l}\rvert^2$ relation of the heavy- and light-hole dipole-matrix element	1	1	2.1	2.1	2.1
U_0 (meV) Coulomb strength	0	0	0	8.54	8.54
Excitation parameter: pulse width δ and its central frequency ω					
Pulse 1: δ_1 (ps)	0.1	0.005	0.1	0.1	0.1
$\hbar\omega_1$ (meV)	28	28	30	1563	28.25
Pulse 2: δ_2 (ps)	0.1	0.005	0.1	0.1	0.1
$\hbar\omega_2$ (meV)	28	28	30	1563	28.25
Pulse 3: δ_3 (ps)	0.1	0.005	0.1	0.1	0.1
$\hbar\omega_3$ (meV)	28	28	30	1563	28.25
delay time $T(ps)$	0	0	0	0.1	0.35

set	VI	VII	VIII	IX	X
N number of the sites	40	40	40	40	58
a (nm) site separation	5	5	5	5	5
a_0/a regularization parameter	5	5	5	5	5
J^e(meV) coupling strength of the electron band	10	10	10	10	10
J^h(meV) coupling strength of the heavy-hole band	2	2	2	-2	2
J^l(meV) coupling strength of the light-hole band	18.5	18.5	18.5	18.5	18.5
J^{hl}(meV) coupling strength between heavy- and light-hole band	0	4	4	4	0
T_2^h (ps) dephasing time of the heavy-hole exciton	0.53	0.53	0.47	0.47	0.53
T_2^l (ps) dephasing time of the light-hole exciton	0.47	0.47	0.53	0.53	0.47
T_2^{hh} (ps) dephasing time of the heavy-hole biexciton	0.53	0.53	0.47	0.47	0.53
T_2^{ll} (ps) dephasing time of the light-hole biexciton	0.47	0.47	0.53	0.53	0.47
$T_2^{(hl,lh)}$ (ps) dephasing time of the mixed (heavy- and light-hole) biexciton	0.25	0.25	0.25	0.25	0.25
$\hbar\Delta\omega$ (meV) heavy-light hole offset	41.5	39.2	22.5	30.3	42.93
$\lvert\frac{\mu_h}{\mu_l}\rvert^2$ relation of the heavy- and light-hole dipole-matrix element	3	3	0.03	0.03	3
U_0 (meV) Coulomb strength	8.2	8.2	8.54	8.54	8.2
Excitation parameter: pulse width δ and its central frequency ω					
Pulse 1: δ_1 (ps)	0.1	0.1	0.1	0.1	0.1
$\hbar\omega_1$ (meV)	33.4	33.4	33.4	33.4	33.4
Pulse 2: δ_2 (ps)	0.1	0.1	0.1	0.1	0.1
$\hbar\omega_2$ (meV)	33.4	33.4	33.4	33.4	33.4
Pulse 3: δ_3 (ps)	0.1	0.1	0.1	0.1	0.1
$\hbar\omega_3$ (meV)	33.4	33.4	33.4	33.4	33.4
delay time $T(ps)$	0.1	0.1	0.1	0.1	0.1

set	XI	XII	XIII	XIV	XV
N number of the sites	10	10	10	40	10
a (nm) site separation	5	5	5	5	5
a_0/a regularization parameter	5	5	5	5	5
J^e(meV) coupling strength of the electron band	6	22	6	6	6
J^h(meV) coupling strength of the heavy-hole band	2	2	2	2	2
J^l(meV) coupling strength of the light-hole band	8.5	8.5	2.35	2.35	2.35
J^{hl}(meV) coupling strength between heavy- and light-hole band	4	4	0	0	0
T_2^h (ps) dephasing time of the heavy-hole exciton	0.44	0.44	1.3	1.3	1
T_2^l (ps) dephasing time of the light-hole exciton	0.51	0.51	1.3	0.8	0.5
T_2^{hh} (ps) dephasing time of the heavy-hole biexciton	0.44	0.22	1.04	1.3	1
T_2^{ll} (ps) dephasing time of the light-hole biexciton	0.51	0.255	1.04	0.8	0.5
$T_2^{(hl,lh)}$ (ps) dephasing time of the mixed (heavy- and light-hole) biexciton	0.24	0.12	0.51	0.5	0.33
$\hbar\Delta\omega$ (meV) heavy-light hole offset	35	35	6	11.9	30
$\lvert\frac{\mu_h}{\mu_l}\rvert^2$ relation of the heavy- and light-hole dipole-matrix element	0.3	0.3	1	2.1	1000
U_0 (meV) Coulomb strength	8.54	8.54	8.54	8.54	8.54
Excitation parameter: pulse width δ and its central frequency ω					
Pulse 1: δ_1 (ps)	0.1	0.1	0.1	0.1	10
$\hbar\omega_1$ (meV)	29	29	18.7	1563	15.87
Pulse 2: δ_2 (ps)	0.1	0.1	0.1	0.1	0.005
$\hbar\omega_2$ (meV)	29	29	18.7	1563	26
Pulse 3: δ_3 (ps)	0.1	0.1	0.1	0.1	0.005
$\hbar\omega_3$ (meV)	29	29	18.7	1563	26
delay time $T(ps)$	0.1	0.1	0	0.1	0

Additionally we refer to material parameters. The reduced exciton mass is given by:

$$m_r^{h(l)} = \frac{m_e * m_{h(l)}}{m_e + m_{h(l)}}, \tag{B.1}$$

where

$$m_{h(l)} = \frac{\hbar^2}{2J^{h(l)}a^2}, \tag{B.2}$$

are effective masses of the heavy- and light-hole excitons, $J^{h(l)}$ are their coupling parameters and a is the lattice constant (see for the details Chapter 3.1).

Thus we can estimate the influence of the model parameters such as electron J^e and hole $J^{h(l)}$ couplings on the excitonic reduced mass.

$$\begin{aligned} m_r^h &\propto -\frac{1}{J^e - J^h}, \\ m_r^l &\propto -\frac{1}{J^e - J^l}. \end{aligned} \tag{B.3}$$

In this work we have considered semiconductor nanostructures, in particular different quantum wells. The material parameters such as an effective mass dependents on the design of a particular quantum well. Since in the quantum well the sub-bands are confined, the effective mass will depend not only on the material compound, but on the confinement potential as well. This is the reason for different effective masses of the bulk and the quantum well. Usually, for the rough estimation of the effective masses of the quantum well[1] the bulk parameter are used.

To give an idea of the model parameters used in our numerical simulations, we calculate the effective masses of the GaAs quantum well for the parameter set given in VII.

$$\begin{aligned} m_e &= 0.1523 * m_0, \\ m_h &= 0.76 * m_0, \\ m_l &= 0.0806 * m_0, \end{aligned} \tag{B.4}$$

where $m_0 = 9.109 * 10^{-31}$ kg. The effective masses for the bulk material taken from Ref. [53] are:

$$\begin{aligned} m_e &= 0.067 * m_0 \\ m_h &= 0.643 * m_0 \\ m_l &= 0.0806 * m_0 \end{aligned} \tag{B.5}$$

---

[1] In particular, for the wide quantum well the effective masses of the bulk and quantum well are nearly the same.

It has to be mentioned, that for the accurate estimation of the effective masses, the comparison of the measured and calculated band structure are needed. In fact, for the quantum well it has to be done for each particular quantum well.

Furthermore, we have used the phenomenological damping parameter T_2 for excitons and biexcitons, the so called dephasing time. This allows us to investigate different signatures in details, for a example the signatures of bound, unbound and mixed (heavy-light hole) biexcitons. The dephasing times of the heavy-hole T_2^{hh}, light-hole T_2^{hh} biexcitons and the mixed ones are given as:

$$\begin{aligned} T_2^{hh} &= \alpha_1 T_2^h, \\ T_2^{ll} &= \alpha_2 T_2^l, \\ T_2^{hl(lh)} &= \frac{\alpha_3}{1/T_2^h + 1/T_2^l}, \end{aligned} \tag{B.6}$$

where $\alpha_1, \alpha_2, \alpha_3$ are certain coefficients.

Bibliography

[1] R. R. Ernst, G. Bodenhausen, and A. Wokaun, *Principles of Nuclear Magnetic Resonance in One and Two Dimensions*, (Oxford Science Publications, New York, 1987).

[2] R. M. Hochstrasser, Proc. Natl. Acad. Sci. USA. **104**, 14190 (2007).

[3] T. Zhang, C. N. Borca, X. Li, and S. T. Cundiff, Opt. Express **13**, 7432 (2005).

[4] T. Meier, P. Thomas, and S. W. Koch, *Coherent Semiconductor Optics - From Basic Concepts to Nanostructure Applications*, (Springer, Berlin, 2007).

[5] S. Mukamel, *Principles of Nonlinear Optical Spectroscopy*, (Oxford, New York, 1995).

[6] M. Koch, J. Feldmann, G. von Plessen, E. O. Göbel, P. Thomas, and K. Köhler, Phys. Rev. Lett. **69**, 3631 (1992).

[7] X. Li, T. Zhang, C. N. Borca, and S. T. Cundiff, Phys. Rev. Lett. **96**, 057406 (2006).

[8] I. Kuznetsova, P. Thomas, T. Meier, T. Zhang, X. Li, R. P. Mirin, and S. T. Cundiff, Sol. State Comm. **142**, 154 (2007).

[9] L. Yang, I. V. Schweigert, S. T. Cundiff, and S. Mukamel, Phys. Rev. B **75**, 125302 (2007).

[10] T. Meier, C. Sieh, E. Finger, W. Stolz, W. W. Rühle, P. Thomas, and S. W. Koch, phys. stat. sol. (b) **238**, 537 (2003).

[11] M. Khalil, N. Demirdóven, and A. Tokmakoff, J. Phys. Chem. A, **107**, 5258 (2003).

[12] N. A. Kurnit, I. D. Abella, and S. R. Hartmann, Phys. Rev. Letters., **13**, 567 (1964).

[13] T. Meier, and P. Thomas, Physik. Journal, **3**, 53 (2003).

[14] S. Weiser, T. Meier, J. Möbius, A. Euteneuer, E. J. Mayer, W. Stolz, M. Hofmann, W. W. Rühle, P. Thomas, and S. W. Koch, Phys. Rev. B **61**, 13088 (2000).

[15] H. Haug and S. W. Koch, *Quantum Theory of the Optical and Electronic Properties of Semiconductors*, 4th ed. (World Scientific, Singapore, 2004).

[16] A. Stahl, Z. Phys. B **72**, 371 (1988).

[17] L. Bányai, C. Ell, and H. Haug, Phys. Rev. B **36**, 6099 (1987).

[18] W. Huhn and A. Stahl, phys. stat. sol. (b) **124**, 167 (1984).

[19] W. Schäfer, D. S. Kim, J. Shah, T. C. Damen, J. E. Cunningham, K. W. Goosen, L. N. Pfeiffer, and K. Köhler, Phys. Rev. B **53**, 16429 (1996).

[20] M. Wegener, D. S. Chemla, S. Schmitt-Rink, and W. Schäfer, Phys. Rev. A **42**, 5675 (1990).

[21] D. S. Chemla and J. Shah, Nature **411**, 549 (2001).

[22] C. Sieh, T. Meier, A. Knorr, F. Jahnke, P. Thomas, and S. W. Koch, Eur. Phys. J. B **11**, 407 (1999).

[23] E. Finger, S. P. Kraft, M. Hofmann, T. Meier, S. W. Koch, W. Stolz, and W. W. Rühle, phys. stat. sol. (b) **234**, 424 (2002).

[24] F. Jahnke, M. Koch, T. Meier, J. Feldmann, W. Schäfer, P. Thomas, S. W. Koch, E. O. Göbel, and H. Nickel, Phys. Rev. B **50**, 8114 (1994).

[25] Y. Z. Hu, R. Binder, S. W. Koch, S. T. Cundiff, H. Wang, and D. G. Steel, Phys. Rev. B **49**, 14382 (1994).

[26] A. Euteneuer, E. Finger, M. Hofmann, W. Stolz, T. Meier, P. Thomas, S. W. Koch, W. W. Rühle, R. Hey, and K. Ploog, Phys. Rev. Lett. **83**, 2073 (1999).

[27] S. T. Cundiff, M. Koch, W.H. Knox, J. Shah, and W. Stolz, Phys. Rev. Lett. **77**, 1107 (1996).

[28] I. Kuznetsova, Diploma Thesis, (Marburg, 2003), unpublished.

[29] I. Kuznetsova, P. Thomas, T. Meier, T. Zhang, and S. T. Cundiff, Conference Digest of CLEO/Europe-IQEC 2007.

[30] C. N. Borca, T. Zhang, X. Li, and S. T. Cundiff, Chem. Phys. Lett. **416**, 311 (2005).

[31] C. Sieh, T. Meier, F. Jahnke, A. Knorr, and S. W. Koch, P. Brick, M. Hübner, C. Ell, J. Prineas, G. Khitrova, and H. M. Gibbs, Phys. Rev. Lett. **82**, 3112 (1999).

[32] T. Meier, C. Sieh, S. Weiser, M. Reichelt, C. Schlichenmaier, S. Siggelkow, P. Thomas, and S. W. Koch, NIC Symposium, **9** 315 (2001).

[33] V. M. Axt, K. Victor, and T. Kuhn, phys. stat. sol. (b) **206**, 189 (1998).

[34] T. F. Albrecht, K. Bott, T. Meier, A. Schulze, M. Koch, S. T. Cundiff, J. Feldmann, W. Stolz, and P. Thomas, Phys. Rev. B **54**, 4436 (1996).

[35] E. J. Mayer, G. O. Smith, V. Heuckeroth, J. Kuhl, K. Bott, A. Schulze, T. Meier,D. Bennhardt, S. W. Koch, P. Thomas, R. Hey, and K. Ploog, Phys. Rev. B **50**, 14730 (1994).

[36] E. J. Mayer, G. O. Smith, V. Heuckeroth, J. Kuhl, K. Bott, A. Schulze, T. Meier, S. W. Koch, P. Thomas, R. Hey, and K. Ploog, Phys. Rev. B **51**, 10909 (1995).

[37] T. Zhang, I. Kuznetsova, T. Meier, X. Li, R. P. Mirin, P. Thomas, and S. T. Cundiff, Proc. Natl. Acad. Sci. USA, 10.1073/pnas.0701273104, **104**, 14227 (2007).

[38] S. Cundiff, *private communication.*

[39] K. Bott, J. Hader, S. W. Koch, and P. Thomas, Phys. Rev. B **56**, 12784 (1997).

[40] L. Allen and J. H. Eberly, *Optical Resonance and Two-Level Atoms*, (Wiley, New York, 1975).

[41] W. Schäfer and M. Wegener, *Semiconductor Optics and Transport Phenomena*, (Springer, Berlin, 2002).

[42] F. Rossi and T. Kuhn, Rev. Mod. Phys. **74**, 895 (2002).

[43] M. Lindberg, R. Binder, and S. W. Koch, Phys. Rev. A **45**, 1865 (1992).

[44] V. M. Axt, and A. Stahl, Z. Phys. B **93**, 195 (1994); **93**, 205 (1994).

[45] M. Lindberg, R. Binder, and Y. Z. Hu, and S. W. Koch, Phys. Rev. B **49**, 16942 (1994).

[46] W. Langbein, T. Meier, S. W. Koch, and J. M. Hvam J. Opt. Soc. Am. B **18**, 1318 (2001).

[47] T. Meier and S. W. Koch, in *Semiconductors and Semimetals*, Vol. 67, K.T. Tsen, ed., Academic Press, 231 (2001).

[48] I. Kuznetsova, T. Meier, S. T. Cundiff, and P. Thomas, Phys. Rev. B **76**, 153301 (2007).

[49] G. Noll, U. Siegner, S. G. Shevel, and E. O. Göbel, Phys. Rev. Lett. **64**, 792 (1990).

[50] V. G. Lyssenko, J. Erland, I. Balslev, K.-H. Pantke, B. S. Razbirin, and J. M. Hvam Phys. Rev. B **48**, 5720 (1993).

[51] S. G. Carter, Z. Chen, and S. T. Cundiff, Phys. Rev. B, has been accepted for publication (2007).

[52] P. Brick, C. Ell, S. Chatterjee, G. Khitrova, and H. M. Gibbs, T. Meier, C. Sieh, and S. W. Koch, Phys. Rev. B **64**, 075323 (2001).

[53] I. Vurgaftman, J. R. Meyer, and L. R. Ram-Mohan, J. Appl. Phys. **89**, 5815 (2001).

Publications and conference presentations in frame of the thesis

- Polarized Optical Two-dimensional Fourier Transform Spectroscopy of Semiconductors, T. Zhang, X. Li, S. T. Cundiff, R. Mirin, and I. Kuznetsova, Ultrafast Phenomena XV Proceedings of the 15th International Conference, Pacific Grove/CA, USA, July 30 - August 4, 2006

- Signatures of Many-Particle Correlations in Two-Dimensional Fourier-Transform Spectra of Semiconductor Nanostructures, I. Kuznetsova, P. Thomas, T. Meier, T. Zhang, X. Li, R. P. Mirin, and S. T. Cundiff, Sol. State Comm., **142**, 154 (2007)

- Investigation of Coulomb induced coupling in semiconductor nanostructures using 2D Fourier-Transform-Spectroscopy, I. Kuznetsova, P. Thomas, T. Meier, T. Zhang, S. T. Cundiff, DPG Tagung, March 2007

- Many-body Interactions in Semiconductors: Probed by Optical Two-dimensional Fourier Transform Spectroscopy, T. Zhang, X. Li, S. T. Cundiff, R. P. Mirin, I. Kuznetsova, APS March Meeting (2007)

- Investigation of Coulomb-induced coupling in semiconductor nanostructures using 2D Fourier-Transform-Spectroscopy, I. Kuznetsova, P. Thomas, T. Meier, T. Zhang, S. T. Cundiff, CLEO, June 2007

- Polarization-dependent optical 2D Fourier transform spectroscopy of semiconductors, T. Zhang, I. Kuznetsova, T. Meier, X. Li, R. P. Mirin, P. Thomas, and S. T. Cundiff, Proc. Natl. Acad. Sci. USA, 10.1073/pnas.0701273104, **104**, 14227 (2007)

- Polarization-dependent 2D Fourier transform spectroscopy of quantum wells, T. Zhang, X. Li, A. D. Bristow and S. T. Cundiff, I. Kuznetsova, T. Meier, and P. Thomas, R. P. Mirin, FOPS, July 2007

- Determination of Homogeneous and Inhomogeneous Broadening in Semiconductor Nanostructures by Optical Two-Dimensional Fourier-Transform Spectroscopy, I. Kuznetsova, T. Meier, S. T. Cundiff, and P. Thomas, Phys. Rev. B **76**, 153301 (2007).

During the work on my PhD thesis I have been working also on microscopic modeling of different processes in the semiconductor laser structures. The results have been presented in the following publications and conference contributions:

- Nonequilibrium gain in optically pumped GaInNAs laser structures, A. Thränhardt, T. Meier, M. Reichelt, C. Schlichenmaier, B. Pasenow, I. Kuznetsova, S. Becker, T. Stroucken, J. Hader, A. R. Zakharian, J. V. Moloney, W. W. Chow, S. W. Koch, Appl. Phys. Lett. **85**, 5526 (2004).

- Nitrogen incorporation effects on gain properties of GaInNAs lasers: experiment and theory, A. Thränhardt, I. Kuznetsova, C. Schlichenmaier, and S. W. Koch, L. Shterengas and G. Belenky, J.-Y. Yeh and L. J. Mawst, N. Tansu, J. Hader and J. V. Moloney, W. W. Chow, Appl. Phys. Lett. **86**, 201117 (2005).

- Linewidth enhancement factor in semiconductor quantum well $In_{1-y}Ga_yAs$ and $In_{1-y}Ga_yAs_{1-x}N_x$, I. Kuznetsova, A. Thränhardt, C. Schlichenmaier, S. W. Koch, J. Hader, J. V. Moloney and W. W. Chow, CLEO, June 2005

- Microscopic modeling of radiative losses in semiconductor laser structures, I. Kuznetsova, A. Thränhardt, C. Schlichenmaier, S. W. Koch, J. Hader, J. V. Moloney, NUSOD, September 2005

Acknowledgement

This work has been not created during only the last three months. The basis for this work has been layed out at the beginning of my studies in Germany. I started with the Großpraktikum under Prof. Dr. Peter Thomas and decided to do research in the group of Prof. Dr. Stephan Koch and Prof. Dr. Peter Thomas. I am thanking Prof. Dr. Stephan Koch for financial support. During this time I learned all about semiconductor physics and finished diploma under the supervision of Prof. Dr. Peter Thomas. Thank you Peter for your very clear explanations, the language corrections, the patience with me, for believing in me.

This work has been inspired by experiments made in the group of Prof. Dr. Steven Cundiff (JILA, University Colorado) and Peter Thomas drew my attention to it. I am very glad that I choose this topic for my dissertation and could enjoy the excellent collaboration with Peter, Torsten (Universität Paderborn), Steven and Tianhao (JILA, University Colorado). I will never forget the long-hours discussions about physics and philosophy with Peter. I also thank Prof. Dr. Torsten Meier for his valuable comments and programming codes. Since the problems treated in my dissertation have required numerical calculations, including parallel computing, I was glad to have the possibility to execute my codes in the Neumann Institute for Computing in Jülich. The collaboration with Steven and Tianhao was a pleasured due to rapid communications, important discussions and exchanging of the information and data. Thank you Steven for believing in me.

During my PhD I have been also working on the other topics, namely the simulations of semiconductor-laser properties. I learned about the gain properties of the different structures and the programming language C. For the support in this period I want to thank my colleagues Dr. Angela Thränhardt and Dr. Christoph Schlichenmaier. For valuable discussions and collaboration I thank Dr. Weng Chow from Sandia National Laboratories, and Dr. Jörg Hader from the University of

Arizona in Tucson.

I am thanking my colleagues: Péter Bozsoki, Mathias Reichelt, Oleg Rubel, Noémi Gőgh, Marco Werchner, Christina Bückers, Bernhard Pasenow, Eckhard Kühn, and Thomas Feldtmann, who created a good atmosphere in the office and were always ready to help. We spent a good time together not only at the desk, but also during hiking tours organized by Peter Thomas.

I have to direct a special thank to the European Graduate College "Electron-electron interactions in solids", which played an important role in my carrier as a physicist. During 4 years of participation in this EGC I was trained to give good presentations, to lead scientific discussions, to be independent and self-confident.

Besides my supervisors and colleges, my friends were of great help for me (kind of a family in the foreign country). I thank for the mental support Ira Sharunova, Anna Leibo, Agnes Dabrowski, Silke Karg, Tracy Sutphin, Elizabeth Kruse, Gregorio Da Rosa, Uwe Bulthaup, Vitaly Pankov, Richard Benninger, Peter Brand and my yoga-people.

This work is dedicated to my family, whose love has no begin and no end. I love you mama, papa and my brother Igor.

Wissenschaftlicher Werdegang

23 November 1977	geboren in st. Staroizobilnaja, Region Stawropol/Rußland.
1985–1995	Mittelschule (entspr. Gymnasium und Hochschulzugangsberechtigung) in der Region Semipalatinsk/Kazachstan, Finsterwalde/Deutschland, Morozowsk/Rußland.
1 September 1995	Einschreibung an der Fakultät für Physik an der Staatlichen Universität Rostow–am–Don.
29 Juni 1999	Bacheloreabschluß und weiterführendes Magisterstudium. Thema: “Numerische Modellierung des Übertragungsprozesses von Strahlung in einem statistisch-heterogenen Plasma (Reflexionsfall)”.
Oktober 2001	Fortsetzung des Physikstudiums an der Philipps-Universität Marburg.
2003–2004	Wissenschaftliche Hilfskraft in der Arbeitsgruppe Theoretische Halbleiterphysik. Großpraktikum, Beitrag für das Buch “Coherent Semiconductor Optics – From Basic Concepts to Nanostructure Applications”.
16 Januar 2004	Diplomabschluß. Thema: “Coulomb-induzierte Kopplungen optischer Anregungen in geordneten Halbleitern”.
Seit 1 April 2004	Wissenschaftliche Mitarbeiterin an der Philipps-Universität Marburg und Beginn des Promotionsstudiums.
24 Oktober 2007	Disputation.